High Strain Rate Behaviour of Hot Formed Boron Steel with Tailored Properties

by

Alexander Bardelcik

A thesis
presented to the University of Waterloo
in fulfilment of the
thesis requirement for the degree of
Doctor of Philosophy
in
Mechanical Engineering

Waterloo, Ontario, Canada, 2012

ABSTRACT

In an automotive crash event, hot stamped, die quenched martensitic structural components have been shown to provide excellent intrusion resistance. These alloys exhibit only limited ductility, however, which may limit the overall impact performance of the component. The introduction of lower strength and more ductile "tailored" properties within some regions of a hot stamped component has the potential to improve impact performance. One approach being applied to achieving such tailored properties is through locally controlling the cooling rate within the stamping die. The primary motivation for the current work is to understand the role of cooling rate on the as-quenched mechanical response of tailored hot stampings, which has required characterization of the high strain rate mechanical behaviour of tailored hot stamped boron steel.

The effect of cooling rate and resulting microstructure on the as-quenched mechanical behavior of USIBOR® 1500P boron steel at strain rates between 10^{-3} and 10^{3} s^{-1} was investigated. Specimens quenched at rates above the critical cooling rate (~27 °C/s) exhibited a fully martensitic microstructure with a UTS of ~1,450 MPa. Sub-critical cooling rates, in the range 14°C/s to 50 °C/s, resulted in as-quenched microstructures ranging between bainitic to martensitic, respectively. Tension tests revealed that predominantly bainitic material conditions (14 °C/s cooling rate) exhibited a lower UTS of 816 MPa compared to 1,447 MPa for the fully martensitic material condition (50 °C/s cooling rate) with a corresponding increase in elongation from 0.10 to 0.15 for the bainitic condition. The reduction in area was 70% for the bainitic material condition and 58% for the martensitic material conditions which implied that a tailored region consisting of bainite may be a desirable candidate for implementation within a hot stamped component. The strain rate sensitivity was shown to be moderate for all of the as-quenched material conditions and the measured flow stress curves were used to develop a strain rate sensitive constitutive model, the "Tailored Crash Model (TCM)". The TCM accurately reproduced the measured flow stress curves as a function of effective plastic strain, strain rate and Vickers hardness (or area fraction of martensite and bainite).

The effect of deformation during quenching and the associated shift in the CCT diagram on the subsequent constitutive response was also examined for this material. Specimens were simultaneously quenched and deformed at various cooling rates to achieve a range of as-quenched microstructures that included ferrite in addition to martensite and bainite. Tensile tests conducted on these specimens at strain rates ranging from 0.003 s^{-1} to ~80 s^{-1} revealed that the presence of ferrite resulted in an increase in uniform elongation and *n*-value which increased overall energy absorption for a given hardness level. The strain rate sensitivity was shown to be moderate for all of the as-quenched material conditions and the TCM constitutive model was extended to account for the presence of ferrite. This extended constitutive model, the "Tailored Crash Model II (TCM II)", has been shown to predict flow stress as a function of effective plastic strain, strain rate and area fraction of martensite, bainite and ferrite.

As a validation exercise, uniaxial tension test simulations of specimens extracted from the transition zone of a hot stamped lab-scale B-pillar with tailored properties [1] were performed. The measured hardness distribution along the gauge length of the tensile specimens was used as input for the TCM constitutive model to define the element constitutive response used in the finite element (FE) models. The measured stress versus strain response and strain distribution during loading (measured using digital image correlation) was in excellent agreement with the FE models and thus validated the TCM constitutive model developed in this work. Validation of the TCM II version of the model is left for future work.

ACKNOWLEDGEMENTS

I would like to thank my supervisor Prof. Michael Worswick for giving me the opportunity to pursue my life goal of becoming a scientist. Without his foresight and keen sense of the “next big thing”, I would not have had the opportunity to work on such an important and industrially relevant research project. I am grateful for his guidance and confidence in my ability. I would also like to thank my co-supervisor Prof. Mary Wells, who’s constant words of encouragement and expertise in the field of material science aided me immensely.

This research would not have been possible without the financial and intellectual support from our industry partners, especially the late Dylan Thomas and Duane Detwiler from Honda R&D Americas, who spearheaded and continued to support the project, respectively. ArcelorMittal Dofasco generously provided the USIBOR® 1500P material studied in this work and Ron Soldaat’s experience and willingness to help in any way possible was appreciated very much. The industrial experience and expertise brought to the table by Nick Adam and Darren Womack from Promatek Research Centre were invaluable in completing this project. Financial support from the Natural Sciences and Engineering Research Council of Canada, the Ontario Research Fund and the Canada Research Chair Secretariat is also gratefully acknowledged.

The experimental portion of this work required the assistance from the skilled and devoted MME technical staff. I owe many thanks to Tom Gawel for his help in the lab and friendship outside it. I am very grateful to Andy Barber who held my hand every time I had to activate a new hydraulic apparatus. Jason Benninger’s machining expertise was critical throughout the development of the tools and specimens required to complete this work. Dr. Sooky Winkler every so kindly taught me the tricks of her trade when it came to metallography. The Engineering Machine Shop had a critical role in this work, so I would like to thank John Boldt and his staff, especially Rick Forgett, Mark Kuntz, Karl Janzen and Charlie Boyle. I want to thank Laurie Wilfong for her dedication to keeping me and the Worswick group on track.

Last but not least, I want to thank my parents who sacrificed so much to give my sister and I a chance at a better life in Canada. Caroline, I couldn’t imagine anyone else by my side

to support me throughout my doctoral work and life in general. My ray of sunshine, Ivan, seeing your beautiful and happy face has helped me get through the good times and the bad.

For my dear Caroline and Ivan

TABLE OF CONTENTS

LIST OF FIGURES

LIST OF TABLES

1 INTRODUCTION

Hot stamping is a relatively new manufacturing process used to form structural vehicle components that have ultra high strength steel (UHSS) properties with ultimate tensile strengths in the order of 1,500 MPa due to a fully martensitic material condition. One of the main advantages of implementing hot stamped components is the potential to lightweight a vehicle structural assembly, while maintaining crashworthiness. A recent development at the University of Waterloo has shown that the in-die heating technique can be implemented within a conventional hot stamping process to produce lower strength and higher ductility regions of "tailored" properties consisting of varying volume fractions of martensite, bainite and ferrite [1]. A hot stamped part with tailored properties has the potential to improve the impact (crash) performance of vehicle structural members, but there is currently little published work on the mechanical response of hot stamped materials with such tailored properties. This is the main motivation for the work presented in this thesis, which focuses on experimentally simulating the hot stamping thermal-mechanical processing routes required to produce tailored microstructures and then subsequently testing the as-quenched tailored materials in uniaxial tension at various strain rates to characterize the mechanical behaviour. In addition to the measured mechanical response, another primary deliverable stemming from this work is the development of a strain rate sensitive constitutive model that is capable of predicting the flow stress behavior for the various multiphase tailored material conditions. The main beneficiaries of this model will be those who implement hot stamped components (with tailored properties) within a vehicle crash protective structure and simulate full vehicle crash scenarios. The accurate prediction of the low to high strain rate response of tailored hot stamped components is a necessary step to enable virtual optimization and commercialization of vehicle crash structures that are both lightweight and meet stringent crash test regulations.

This thesis has been written in a "manuscript-based" style which includes first this synopsis of the thesis work, followed by several parts documenting each aspect of the research. The synopsis comprises a review of the current state of the art in hot stamping, an outline of the objectives and a summary of the research results, followed by a discussion, conclusions and future work. The remainder of the thesis consists of four individual parts that detail the work done and results accomplished to fulfill the objectives. Each part is a published or submitted peer-review manuscript.

2 HOT STAMPING: THE CURRENT STATE OF THE ART

2.1 The Hot Stamping Process

The current demand to reduce vehicle weight for improved fuel efficiency, while maintaining crash performance, has led to the application of new and innovative materials and manufacturing processes in the automotive industry. One such process is hot stamping (or press hardening) of boron steel, which allows conventionally stamped parts to attain Ultra High Strength Steel (UHSS) properties with tensile strengths up to 1,500 MPa. The UHSS properties are a result of in-die quenching, which causes a hot blank to undergo a solid-state phase transformation from austenite to 100% martensite during the forming process. The elevated strength of hot formed parts allows for the use of thinner gauge sheet metal, which results in vehicle weight reduction while maintaining structural integrity. The adoption of hot stamped components within a vehicle structure is becoming more commonplace as indicated by a steady increase in global production rate [2,3]. The hot stamping process is currently used to manufacture structural components such as bumper beams, door intrusion beams, A- and B-pillars, roof and side rails [2,4-8]. Figure 1 shows some of the typical structural components which are currently being produced or are candidates to be manufactured using the hot stamping process. These are critical crash components of a vehicle.

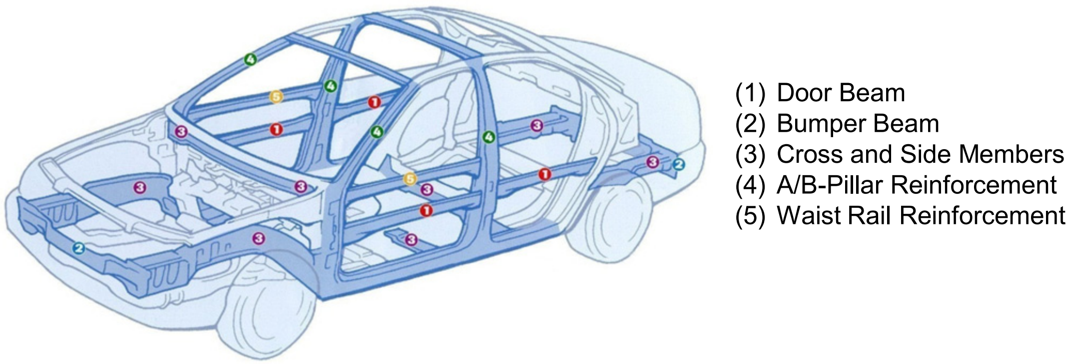

Figure 1: Structural components currently (or candidates to be) manufactured by hot stamping [6].

2.2 Tailored Properties for Improved Crash Performance

Although components with a fully martensitic microstructure are often desired due to their exceptional high strength and intrusion resistance, some structural components, such as a B-pillar, may benefit from regions of lower strength but greater ductility for improved energy absorption. Figure 2 is a schematic of a B-pillar with a region of tailored properties that has been adapted from the work of Maikranz-Valentin et al. [9]. Maikranz-Valentin et al. were among the first to suggest that the crashworthiness of a vehicle with a hot stamped B-pillar containing a tailored region would improve based on the frontal and side load transmission paths within a vehicle structural frame when subjected to crash loading. Munera et al. [10,11] created, tested and modeled multiple crash structures that were produced by tailor welding a conventional hot stamping boron steel sheet to a steel sheet that resisted the martensitic phase transformation during hot stamping and remained soft. They showed that the tailored components offered lower reduced component weight (compared to conventionally stamped steel) and improved the overall passenger safety in a crash event.

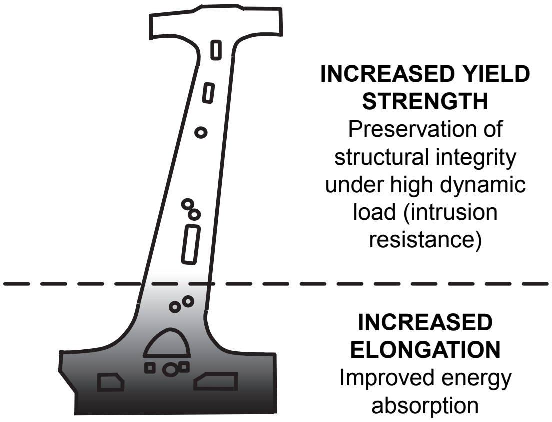

Figure 2 - A schematic of a B-pillar with tailored properties. Adapted from [9].

Munera et al. [10] also stressed the importance of capturing the strain rate sensitivity in their crash models to account for local deformation rates that reach strain rates of 1,000 s^{-1}. This revelation is not new as it has been well established that vehicle structural components undergo deformation at strain rates that range from quasi-static (0.001 s^{-1}) to high strain rates (1,000 s^{-1}) in local hinge point regions [12-18]. It is widely accepted among the crash modeling community that the successful and accurate prediction of vehicle crash behavior is dependent on the accuracy of the strain rate sensitive constitutive model implemented for the structural components within the finite element (FE) analysis [15-17,19-21]. The accuracy of the crash models is crucial during the design and development stage of new vehicle concepts to ensure that vehicles pass certification trials at the prototype stage.

2.3 Producing a Hot Stamped Part with Tailored Properties

Multiple variations of the hot stamping process exist that are capable of producing a tailored hot stamping as reviewed in [8,9,22]. The various processes are outlined below.

2.3.1 Tailor Welded Blanks

ArcelorMittal has austenized and hot formed tailor welded blanks made of boron sheet metal (USIBOR® 1500P) and DUCTIBOR® 500P. The boron steel achieves an ultimate tensile strength (UTS) of 1,500 MPa while the DUCTIBOR® 500P material exhibits a UTS of 500 MPa and about 20% uniform elongation after hot stamping [10,11,22]. The disadvantage of this process is the additional blanking and welding required which increases the complexity of the process and the cost involved.

2.3.2 Partial heating in a furnace

For this process, a portion of the blank is austenized in an open-ended furnace and subsequently hot formed [4,23]. Only the part of the blank that was austenized achieves full martensitic properties when stamped, while the reminder of the part possesses the as-received properties of USIBOR® 1500P, which are a UTS of 600 MPa and 20% uniform elongation [4]. In this case, the tailored zone is restricted to the as-received material properties of the boron steel, which does not allow for tailoring.

2.3.3 Post Tempering

In this case, a fully martensitic part is hot stamped and then a region is partially subjected to a tempering treatment which reduces the strength and improves ductility by introducing tempered martensite [22,24-26]. The main downfall of post tempering is the addition of another process step in the production chain and some limitations related to isolating the tailored region. Also, the time required to post temper can be as long as several minutes.

2.3.4 Die Materials with Variable Heat Extraction Rates

A hot stamping die can be made with regions of different materials that have varying thermal conductivity characteristics. Where fully martensitic properties (1,500 MPa UTS) are desired, die materials with a thermal conductivity of 50-70 W/mK are used, while in the regions where parts are to have tailored properties (~800 MPa UTS), the thermal conductivity is 5-10 W/mK [27,28]. There is a lack of flexibility in this method because the tailored region cannot be altered once the die has been manufactured.

2.3.5 Partial In-Die Heating

Hot stamped parts with tailored properties can be formed within a die that has heated sections. The heated sections of the die reduce the cooling rate of the boron steel to less than the critical cooling rate at which the martensitic transformation occurs. Figure 3a shows the continuous cooling transformation (CCT) diagram for USIBOR® 1500P [29], which is the material of focus for the current doctoral work. By reducing the cooling rate (CR) to below the critical cooling rate, some volume fraction of bainite can be transformed into the microstructure as shown by CR_2 in Figure 3a. The decomposition of austenite into ferrite requires a cooling rate of 8 °C/s, which is relatively slow and requires a controlled heated environment (i.e. a furnace) as shown by CR_3 in Figure 3a. However, the occurrence of plastic deformation during hot stamping results in a shift of the CCT diagram to the left [30], which allows some volume fraction of ferrite to form, as will be discussed in Section 2.4. Figure 3b is a schematic of the expected true stress versus effective plastic strain response due to the tailored properties as defined by the cooling rate in Figure 3a. The reduced strength and increased ductility are properties that would benefit a hot stamped part such as the one shown in Figure 2.

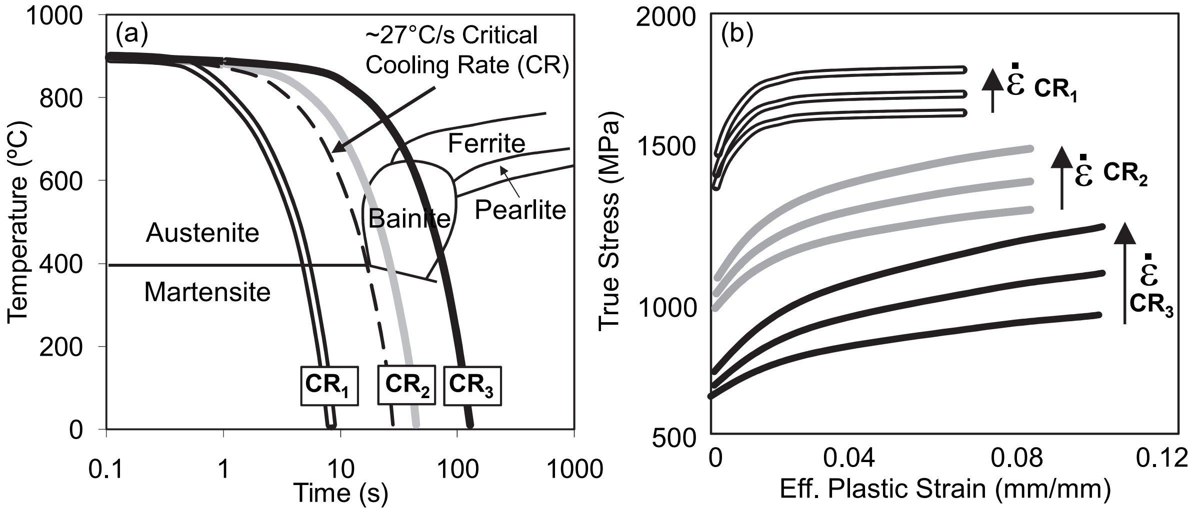

Figure 3 - (a) The continuous cooling transformation (CCT) diagram for USIBOR® 1500P [29]. (b) A schematic of the expected true stress versus effective plastic strain response due to the cooling rates shown in (a).

A number of research groups have examined the in-die heating technique to produce hot stamped parts with tailored properties [31-37]. In some of the existing work, quench times were not published, while for the work where the quench time was published, it was greater than 20 s. Quench time refers to the holding period within the die at the bottom of the forming stroke and a 20 s quench time is not attractive from a production cycle time perspective. To overcome this deficit in the current state of the art, a hot stamping program was undertaken at the University of Waterloo and the development of a hot stamping process with in-die heating and short quench times was one of the primary objectives. As a part of this program, George et al. [1] developed a hot stamping tool with heated sections as shown in Figure 4a. This tool was used to successfully hot stamp a lab-scale B-pillar which contained tailored properties within the soft zone as shown in Figure 4b. It was shown that a heated die section (400 °C) with a quench time of 4 s resulted in a tailored region with a Vickers hardness that was 52% less than the fully martensitic region. Uniaxial tension tests were conducted on a specimen cut from the tailored region which revealed that the ultimate tensile strength decreased by 49% and the uniform elongation increased by 84% when compared to the fully martensitic material condition. Metallographic observations conducted on the hot stamped components revealed that the as-quenched volume fraction of martensite, bainite and ferrite varied based on the heated die temperature and location that the specimen was extracted from. It was shown that the presence of ferrite was found to be more pronounced in regions of the B-pillar where deformation (thinning) was observed.

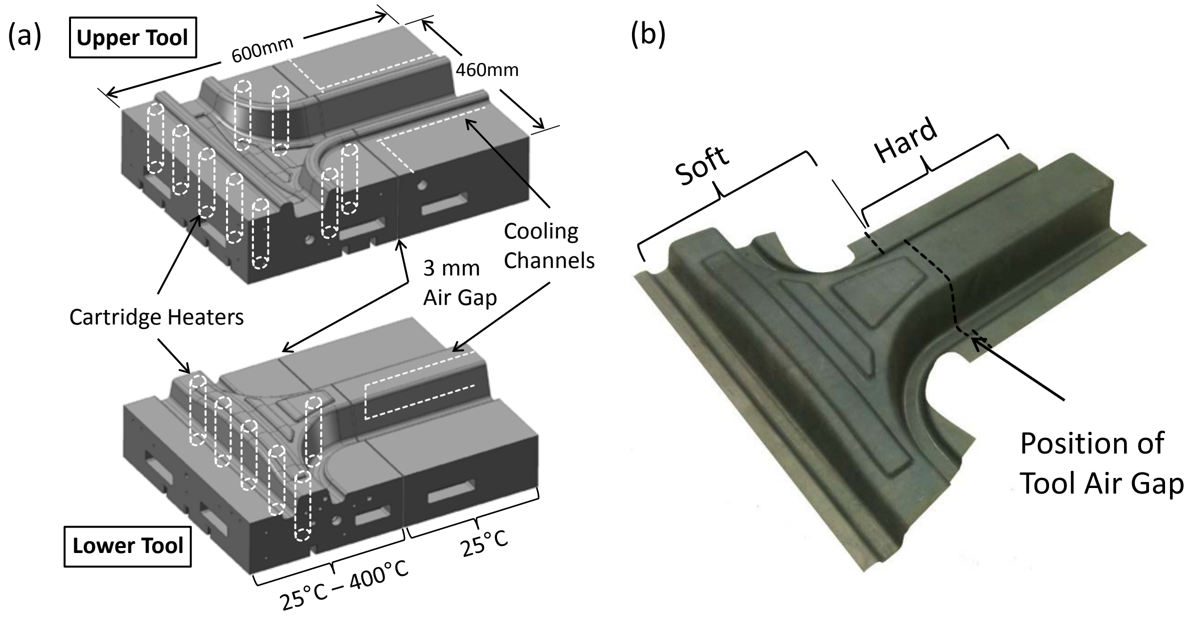

Figure 4 – (a) A CAD model showing the design of the split tool with heated zones (b) A photograph of a hot stamped part.

2.4 Effect of Plastic Deformation during Hot Stamping on the Tailored Properties

The effect of plastic deformation during quenching of a hot stamped boron steel was examined by Barcellona and Palmeri [30]. They used a Gleeble thermal-mechanical simulator to quench and isothermally deform a 22MnB5 boron steel at various temperatures and quench rates that were either above or below the critical cooling rate. The results of their study revealed that plastic deformation caused the continuous cooling transformation (CCT) diagram to shift towards the left, or lower quench times as shown in Figure 5. The CCT also moved downward and this combined shift in the CCT resulted in the decomposition of austenite into bainite and ferrite at quench rates that would normally supress these phase transformations. It should be noted that the as-quenched bainitic structure due to plastic deformation was that of granular bainite. Min et al. [38] conducted experiments similar to those presented in [30] and concluded that the increase in stored energy due to the plastic deformation of austenite contributes to increasing the driving force and shortening the incubation time for the ferrite phase transformation. These effects were amplified as the temperature at which the deformation was imposed was reduced. Unlike the granular bainite morphology reported by Barcellona and Palmeri [30], Min et al. [38] reported that bainite transformed at the austenite grain boundaries was *conventional bainite* (CB) and appeared as packets of parallel ferrite laths separated by a martensite-austenite constituent, while the bainite transformed at intergranular sites was *acicular ferrite* (AF) which grows as randomly oriented ferrite laths or groups of laths which contain discrete martensite-austenite particles. Naderi et al. [39] conducted experiments in which a cylindrical 22MnB5 boron steel specimen was quenched at 50 °C/s and simultaneously deformed (in compression) at various temperatures. The imposed deformation in their experiments resulted in the phase transformation of austenite to martensite and bainite and also indicated that the CCT diagram shifted towards the left and down.

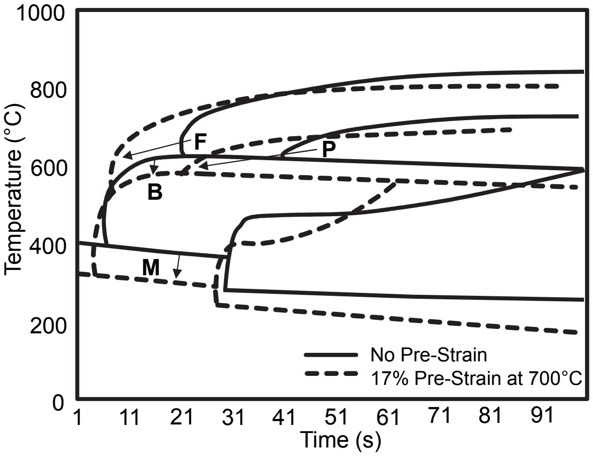

Figure 5 - Effect of deformation on the CCT diagram for 22MnB5 hot stamping steel. Adapted from [30].

Nikravesh et al. [40] and Abassi et al. [41] conducted similar experiments using the same experimental apparatus as Naderi et al. [39] and showed that the presence of ferrite in the as-quenched microstructure varied due to the cooling rate, deformation temperature and strain rate at which deformation occurred. Fan et al. [42] conducted a small scale tensile quenching/deformation study in which a small volume fraction of ferrite was detected in otherwise fully martensitic microstructures at quench rates of 25 °C/s and 30 °C/s for a boron steel. Shi et al. [43] conducted similar work to [40] and concluded that the diffusional phase transformations of polygonal ferrite and bainitic ferrite were facilitated by non-isothermal deformation during quenching.

2.5 Current Deficit in the Literature

Although there has been a substantial research effort put towards understanding the complex phase transformations that result in the as-quenched multiphase (martensite, bainite, ferrite) microstructure of boron steels with tailored properties, there has yet to be a comprehensive assessment of the mechanical response of the as-quenched multiphase material conditions and the implication of applying these materials to vehicle crash structures. In particular, the effect of varying volume fractions of martensite, bainite and ferrite on the strain rate sensitivity, strain hardening response and overall energy absorption behaviour (as illustrated in Figure 3b) need to be explored. This is the main motivation behind the current work, in which a variety of as-quenched material conditions were produced and tested in uniaxial tension at various strain rates. These mechanical characteristics need to be identified and captured within a constitutive model that can be used to define the strain rate sensitive constitutive response of tailored properties within a finite element simulation of a full-scale vehicle crash event.

3 OBJECTIVE

The objective of the current research is to characterize the mechanical response of hot stamped materials or components containing "tailored" properties which consist of multiphase microstructures with varying volume fractions of martensite, bainite and ferrite. In addition, a constitutive model capable of predicting the low to high strain rate constitutive behavior of tailored components is to be developed for implementation within vehicle crash models. In order to achieve this objective, a number of research tasks were undertaken as outlined in the following. The interrelationship between these tasks is captured in the flow chart showing the research strategy in Figure 6.

1. Develop experimental techniques and methods to simulate quenching of boron steel at:
   (i) Quench rates *greater* than the critical cooling rate (~27 °C/s) to produce martensitic as-quenched material conditions.
   (ii) Quench rates *less* than the critical cooling rate (~27 °C/s) to produce martensitic, martensitic/bainitic and bainitic as-quenched material conditions.
   (iii) Quench rates at and less than the critical cooling rate, with simultaneous plastic deformation to produce as-quenched material conditions with varying volume fractions of martensite, bainite and ferrite.

2. Develop and apply metallographic analysis methods to characterize and quantify the microstructures of the various as-quenched phases present within the tailored material conditions.

3. Conduct low to high strain rate uniaxial tension testing on the various as-quenched material conditions. Analyze the stress versus strain response of the material conditions to characterize the influence of martensite, bainite and ferrite on the mechanical properties.

4. Capture the effect of strain rate sensitivity and volume fraction of the as-quenched phases (martensite, bainite and ferrite) in a constitutive model that can be used to define the as-quenched constitutive properties (stress versus strain curves) suitable for simulation of impact (crash) loading of a hot stamped component.

5. Validate the model by comparing the predicted constitutive response against specimens that have been extracted from an actual hot stamping with tailored properties due to in-die quenching.

Work done within these research tasks are summarized in the following sections of this synopsis. More detailed treatment of the research results follow in Parts 1-4 of this thesis, each part consisting of a peer-reviewed research article.

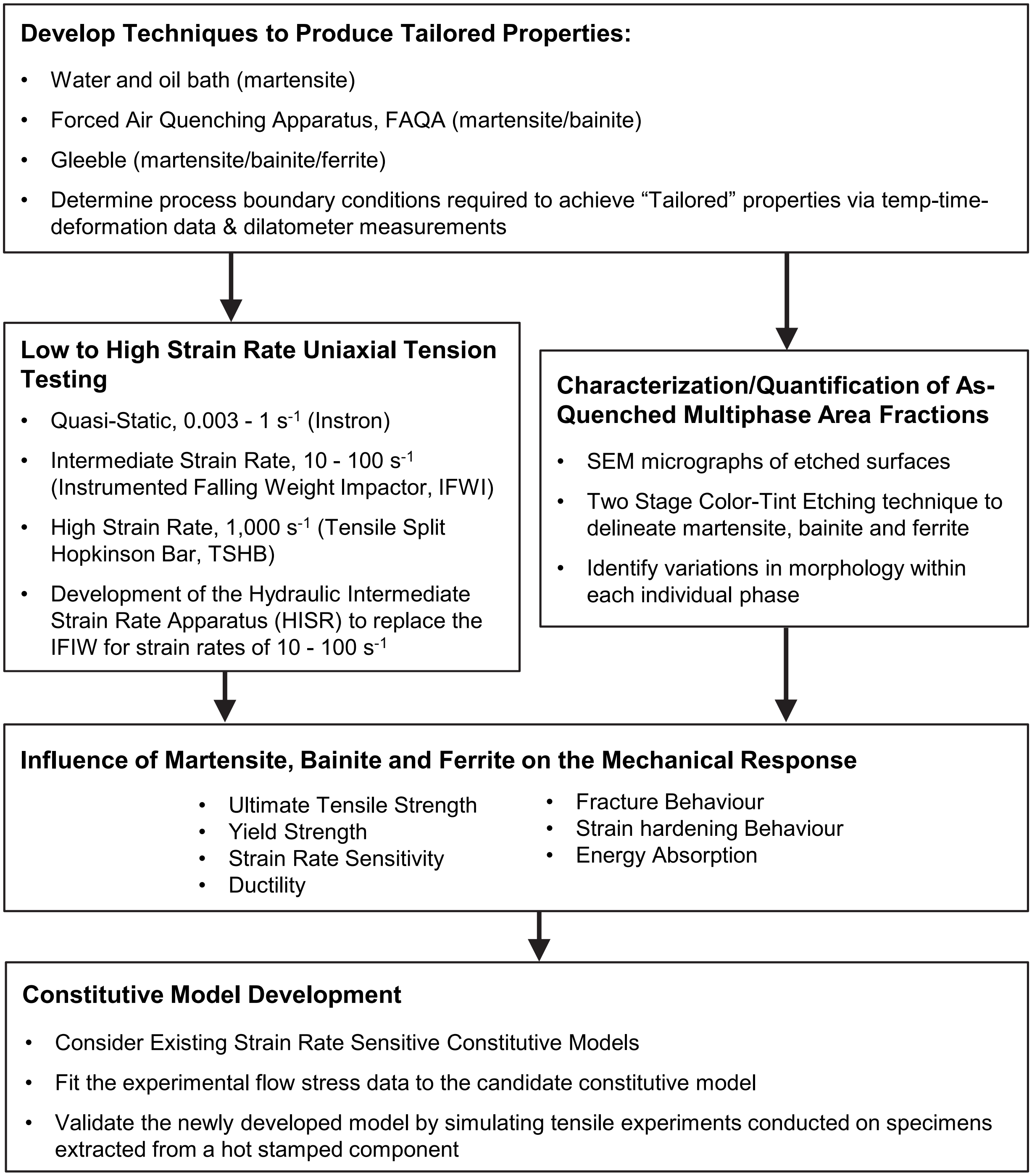

Develop Techniques to Produce Tailored Properties:

- Water and oil bath (martensite)
- Forced Air Quenching Apparatus, FAQA (martensite/bainite)
- Gleeble (martensite/bainite/ferrite)
- Determine process boundary conditions required to achieve “Tailored” properties via temp-time-deformation data & dilatometer measurements

Low to High Strain Rate Uniaxial Tension Testing

- Quasi-Static, 0.003 - 1 s^{-1} (Instron)
- Intermediate Strain Rate, 10 - 100 s^{-1} (Instrumented Falling Weight Impactor, IFWI)
- High Strain Rate, 1,000 s^{-1} (Tensile Split Hopkinson Bar, TSHB)
- Development of the Hydraulic Intermediate Strain Rate Apparatus (HISR) to replace the IFIW for strain rates of 10 - 100 s^{-1}

Characterization/Quantification of As-Quenched Multiphase Area Fractions

- SEM micrographs of etched surfaces
- Two Stage Color-Tint Etching technique to delineate martensite, bainite and ferrite
- Identify variations in morphology within each individual phase

Influence of Martensite, Bainite and Ferrite on the Mechanical Response

- Ultimate Tensile Strength
- Yield Strength
- Strain Rate Sensitivity
- Ductility
- Fracture Behaviour
- Strain hardening Behaviour
- Energy Absorption

Constitutive Model Development

- Consider Existing Strain Rate Sensitive Constitutive Models
- Fit the experimental flow stress data to the candidate constitutive model
- Validate the newly developed model by simulating tensile experiments conducted on specimens extracted from a hot stamped component

Figure 6 - Research strategy.

4 SUMMARY OF THE RESEARCH RESULTS

The research carried out to complete the objective of this research program is presented in four parts. Each part is based on a separate article as shown below:

Part 1	**Bardelcik A**, Salisbury CP, Winkler S, Wells MA, Worswick MJ. Effect of Cooling Rate on the High Strain Rate Properties of Boron Steel. *International Journal of Impact Engineering*, **37** (6), 694-702, 2010.
Part 2	**Bardelcik A**, Worswick MJ, Winkler S, Wells MA. A Strain Rate Sensitive Constitutive Model for Quenched Boron Steel with Tailored Properties. *International Journal of Impact Engineering*, **50**, 49-62, 2012.
Part 3	**Bardelcik A**, Worswick MJ, Wells MA. The Influence of Martensite, Bainite and Ferrite on the As-Quenched Constitutive Response of Simultaneously Quenched and Deformed Boron Steel – Experiments and Model. *Submitted for possible publication*. 2012.
Part 4	**Bardelcik A**, George R, Worswick MJ. Transition Zone Tensile Properties within a Tailored Hot Stamping. *SAE World Congress 2012*, Paper# 2012-01-0531, 2012.

In addition to these four parts, the following four published and peer-reviewed articles were written and based on the current research. These articles have a lesser impact on the overall objective of this thesis and will only be referenced as supportive work:

- George R, **Bardelcik A**, Worswick MJ. Hot Forming of Boron Steel using Heated and Cooled Tooling for Tailored Properties. *Journal of Materials Processing Technology*, **212** (11), 2386-2399, 2012.

- **Bardelcik A**, Ghavam K, George R, Worswick MJ. An Impact Model of a Hot Stamped Lab-Scale B-Pillar with Tailored Properties. *3rd International Conference on Hot Sheet Metal Forming of High-Performance Steel*, 221-228, 2011.

- **Bardelcik A**, Salisbury CP, Worswick MJ, Wells MA. The effect of cooling rate on the mechanical properties and energy absorption potential of hardened boron steel. *2nd International Conference on Hot Sheet Metal Forming of High-Performance Steel*, 105-113, 2009.

- **Bardelcik A**, Salisbury CP, Worswick MJ, Wells MA. High Strain Rate Properties of Hot Formed Die Quenched Boron Steel. *1st International Conference on Hot Sheet Metal Forming of High-Performance Steel*, 45-54, 2008.

4.1 Part 1: Effect of Cooling Rate on the High Strain Rate Properties of Boron Steel

The initial characterization of the effect of cooling rate on the high strain rate behavior of as-quenched boron steel was investigated in this part of the research. The cooling rates that were focused on in this work were near to and greater than the critical cooing rate of ~27 ºC/s. USIBOR® 1500P steel blanks were quenched at three cooling rates (45, 250 and 2,200 °C/s), all of which resulted in fully martensitic as-quenched material conditions. In addition, a single cooling rate was considered, 25 °C/s, that was less than the critical cooling rate. The quenched blanks were machined into miniature dog-bone style tensile specimens that were tested in tension at a quasi-static rate (0.003 s^{-1}) and a high strain rate (960 s^{-1}) using an Instron and a tensile split Hopkinson bar apparatus, respectively. Micro-hardness measurements were made on the quenched specimens and optical micrographs of the as-quenched microstructures were generated.

The path of the measured temperature-time history during quenching (not shown, but found in Figure 2 in Part 1) with respect to the continuous cooling transformation (CCT) diagram indicates that the specimens quenched at 25 °C/s consisted of a “tailored” or mixed phase microstructure. This was confirmed by the measured Vickers hardness and optical micrographs (Figure 7), which revealed that the specimens quenched at 25 °C/s consisted of approximately 5% bainite and 95% martensite by volume. The specimens quenched at the 45, 250 and 2,200 °C/s cooling rates all contained a fully martensitic as-quenched microstructure.

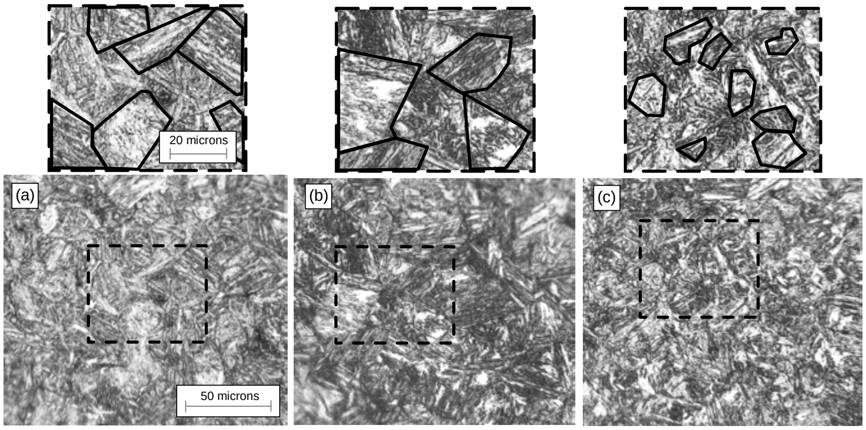

Figure 7 - Optical micrographs of quenched specimens (a) 25 °C/s (b) 45 °C/s and (c) 2,200 °C/s. Etchant: 2% Nital. The microstructure of the 250ºC/s specimens are very similar to the 45 °C/s specimens.

Figure 8a shows the engineering stress versus strain curves (three repeats per cooling rate) measured under quasi-static (0.003 s^{-1}) loading conditions. The quasi-static stress versus strain results revealed that the small volume fraction of bainite within the tailored microstructure (25 °C/s quench condition) reduced the average ultimate tensile strength (UTS) and average yield strength by 190 MPa and 75 MPa, respectively, when compared to the fully martensitic (45 °C/s) material condition. The measured hardness also reduced from 472 HV to 420 HV as the quench rate was decreased from 45 °C/s to 25 °C/s. Although the strength decreased, the overall ductility (i.e. total elongation) did not show any improvement which is not beneficial from an energy absorption perspective. The fracture mechanism was shown (see Figure 9) to be dependent on the microstructure constituents as it transitioned from a ductile-shear mechanism at 25 °C/s which is favourable from a crash perspective, to a more shear dependent mechanism as the cooling rate increased.

The similarity in the stress versus strain response and measured hardness of the 45 °C/s and 250 °C/s quench conditions shown in Figure 8a indicates a robust and large process window for the conventional (fully hardened) hot stamping process. The specimens quenched at 2,200 °C/s, which is outside the realistic capability of the hot stamping process, resulted in an increase in UTS from ~1,450 MPa (average of 45 °C/s and 250 °C/s quench conditions) to 1,640 MPa as shown in Figure 8a, along with an increase in hardness from ~476 HV (average of 45 °C/s and 250 °C/s quench conditions) to 516 HV. This relatively large increase in material strength and hardness was most likely due to the refined microstructure of the specimens quenched at 2,200 °C/s as shown in Figure 7c.

A comparison of the quasi-static and high strain rate average engineering stress versus strain curves in Figure 8b shows moderate strain rate sensitivity for the 45 °C/s quench condition which was similar to the 250 °C/s data that was omitted in the figure for clarity. The 25 °C/s quench condition stress-strain curves shown in Figure 8b show slightly more strain rate sensitivity than the fully martensitic material condition quenched at 45 °C/s. The highest strength martensitic condition, achieved at a cooling rate of 2,200 °C/s, revealed almost no strain rate sensitivity.

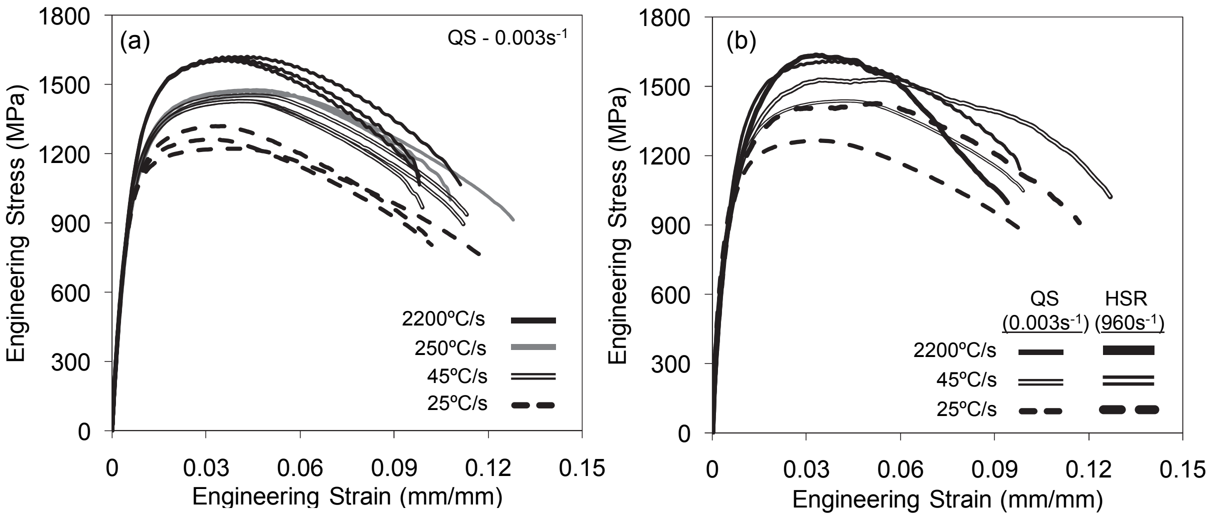

Figure 8 – (a) Quasi-static strain rate (0.003 s^{-1}) engineering stress versus strain results (b) The Average quasi-static (QS) and high strain rate (HSR) engineering stress-strain results. The 250 °C/s results were omitted for clarity.

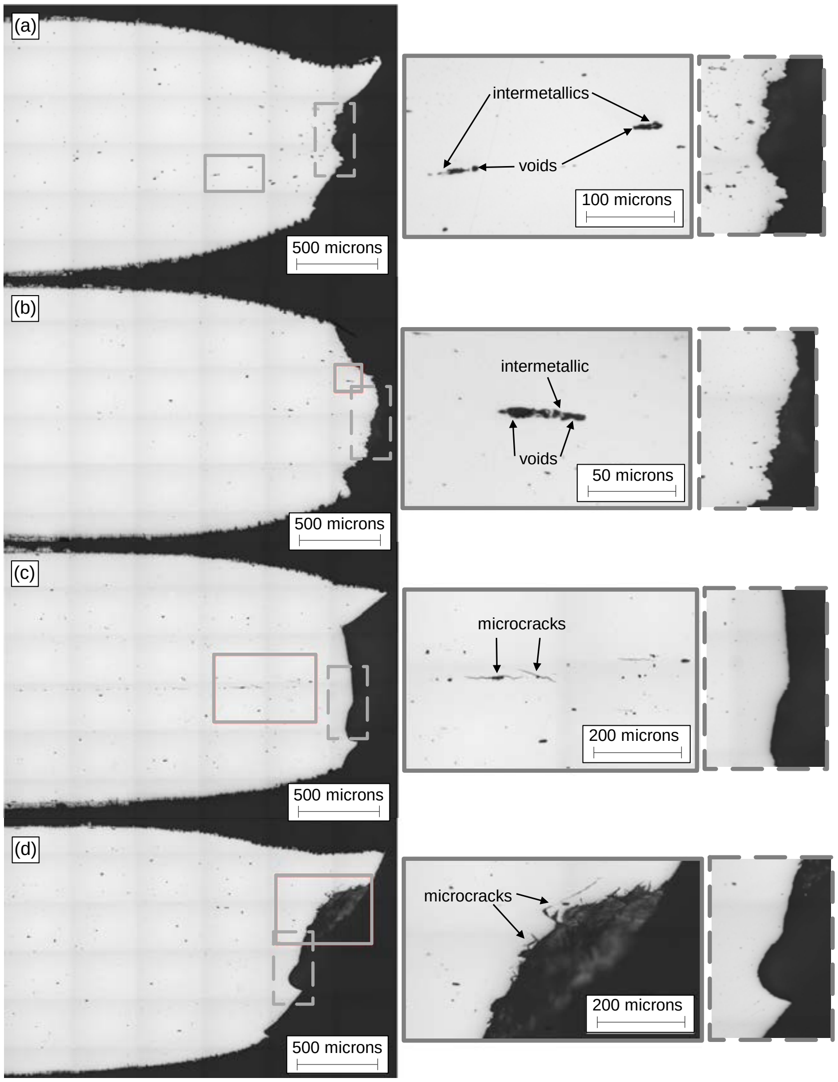

Figure 9 - Optical micrographs showing the cross-section and fracture profiles of specimens tensile tested at 0.003 s^{-1} for samples quenched at (a) 25 °C/s (b) 45 °C/s (c) 250 °C/s and (d) 2,200 °C/s. The images on the right are higher-resolution images of regions highlighted on the left. As-polished and viewed along the long-transverse plane.

4.2 Part 2: A Strain Rate Sensitive Constitutive Model for Quenched Boron Steel with Tailored Properties

The work presented in Part 1 considered a broad range of cooling rates (25 °C/s to 2,200 °C/s) that were close to and greater than the critical cooling rate of (~27 °C/s) for a fully martensitic phase transformation. Part 2 focusses on imposing a range of sub-critical cooling rates (<30 °C/s) to USIBOR® 1500P blanks, in an order to produce as-quenched microstructures that range from martensitic to bainitic. To achieve these sub-critical cooling rates, a forced air quenching apparatus (FAQA) was developed to quench the boron steel blanks. The *apparent* cooling rates that were achieved with the FAQA were 14, 17, 24, 28 and 50 °C/s as shown by the measured temperature-time plots during quenching in Figure 10. The average measured Vickers hardness for these specimens (see Table 1) varied from 268 HV to 466 HV for the 14 °C/s and 50 °C/s quench conditions, respectively. Due to some variability that resulted from the manual nature of the FAQA apparatus, a Gleeble thermo-mechanical apparatus was used to impose the average temperature-time histories shown in Figure 10 to boron steel blanks. The Gleeble processed blanks were then polished and the microstructures shown in Figure 11 were observed using scanning electron microscopy. The microstructure varied from approximately bainitic to martensitic as shown in the Figure 11 micrographs that were used to quantify the area fractions of martensite and bainite for each quench condition as shown in Table 1. Micro-hardness measurements of the as-quenched microstructures revealed a linear relationship between the area fraction martensite (remainder being bainite) and hardness.

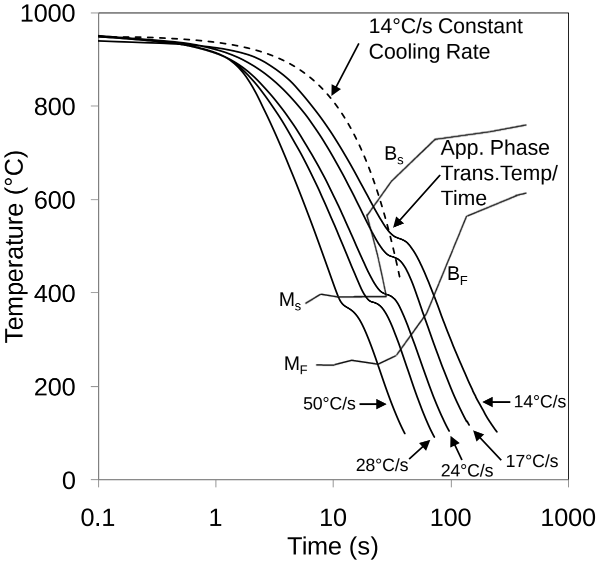

Figure 10 - Average measured temperature versus time curves for the five quench conditions tested in the FAQA. The overlaid CCT diagram is for USIBOR® 1500P that was austenized with similar composition and temperature versus time conditions used in the FAQA tests [29].

Table 1 – The average measured Vickers hardness and average measured area fraction of martensite and bainite for the various apparent cooling rate conditions.

Apparent Cooling Rate (°C/s)	Avg. Measured Vickers Hardness	Avg. Measured % Area Fraction Martensite/Bainite
14	268	3% / 97%
17	318	12% / 88%
24	399	57% / 43%
28	442	86% / 14%
50	466	97% / 3%

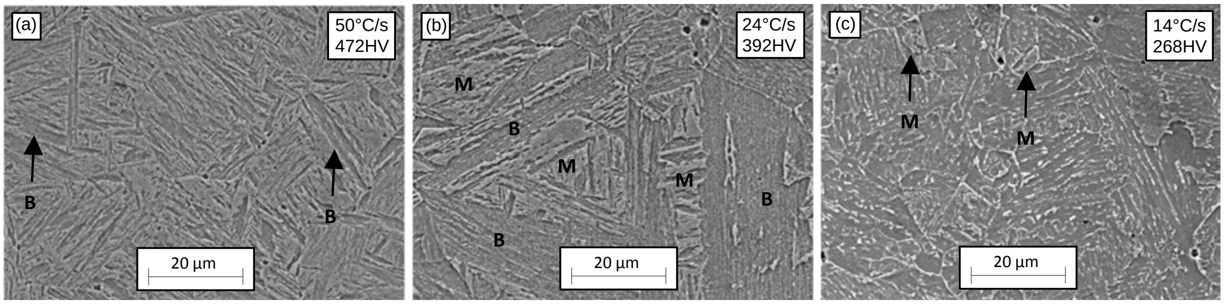

Figure 11 - SEM micrographs of the Gleeble specimens showing (a) an almost fully martensitic microstructure for the 50°C/s specimen (b) a mixed bainitic/martensitic microstructure for the 24°C/s specimen and (c) a predominantly bainitic microstructure for a 14°C/ specimen. (B=bainite, M=martensite).

Miniature dog-bone style specimens were cut from the as-quenched FAQA processed blanks and tested at quasi-static strain rates of 0.003 s^{-1} and 1.0 s^{-1} using an Instron, ~85 s^{-1} using an instrumented falling weight impactor (IFWI) and ~1,075 s^{-1} using a tensile split Hopkinson bar (TSHB) apparatus. The engineering stress versus strain response of the various material conditions pulled at the quasi-static rate is shown in Figure 12a and indicates that the average UTS increased from 816 MPa to 1,447 MPa as the microstructure transitioned from bainitic to martensitic. Figure 12b shows that the elongation to failure exhibited a corresponding increase from 0.10 to 0.15 strain. It was also shown that the elongation to failure improved only when the area fraction of martensite was less than 50%. This finding indicates improved ductility for the more bainitic material conditions which is a key aspect of tailoring the properties of a hot stamping for improved crash performance. There was also an advantageous increase in the fracture surface reduction in area from 58% to 70% as the material varied from martensitic to bainitic as shown in Figure 13. The fracture behaviour varied from a ductile mode to a pure shear mode (see Figure 12c) as the material varied from bainitic to martensitic, respectively.

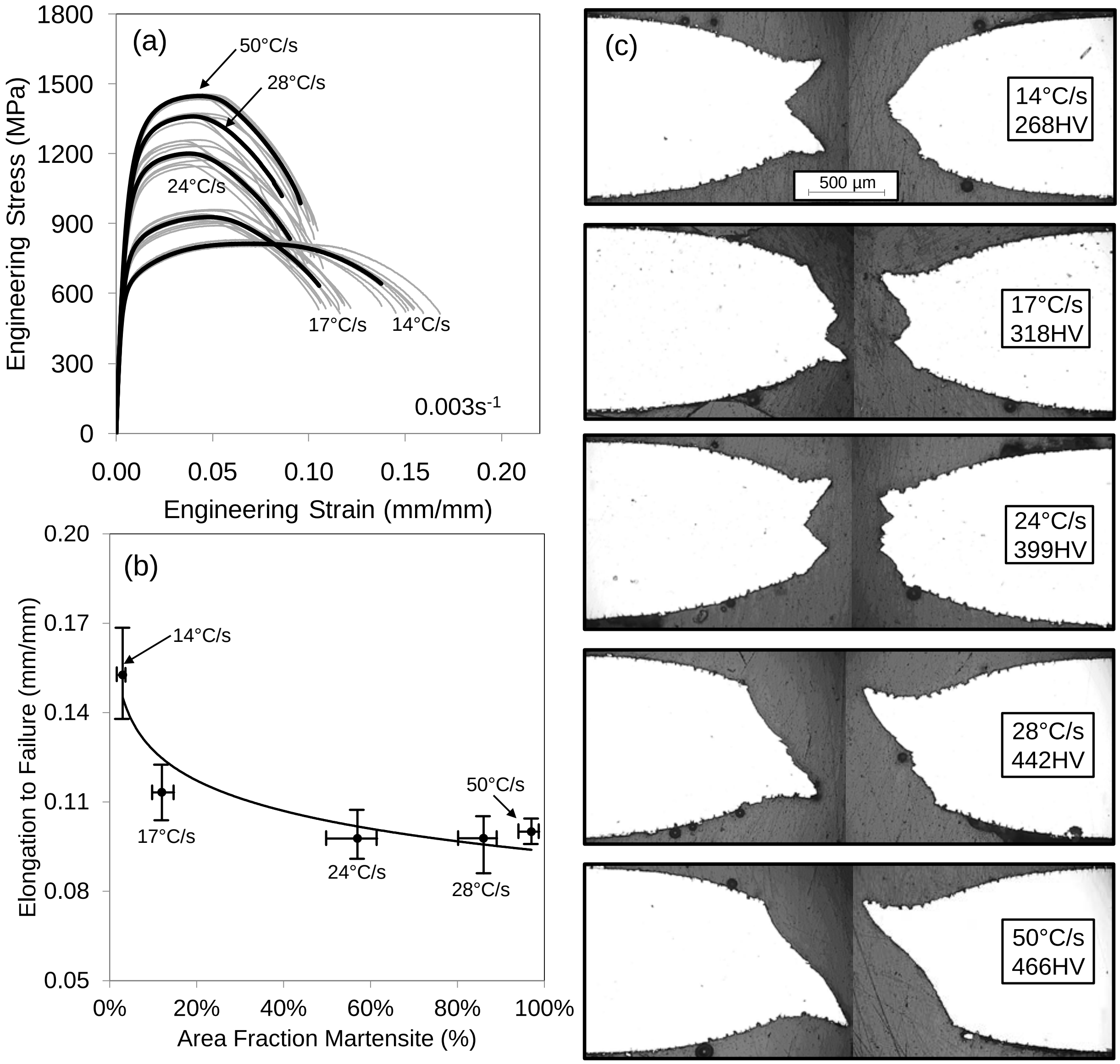

Figure 12 - (a) The engineering stress-strain curves conducted at 0.003 s^{-1} (b) The measured elongation to failure versus % area fraction martensite from the quasi-static (0.003 s^{-1}) tension tests. Note that 0% and 100% area fraction martensite refers to 100% and 0% area fraction bainite, respectively. The vertical and horizontal error bars indicate the maximum and minimum measured values from the repeat measurements (c) Optical microscope images of the fracture surface (cross-sectional views) for specimens quenched at 14-50 °C/s and pulled at 0.003s^{-1}. The specimens quenched at the apparent cooling rates correspond to the following measured area fraction martensite/bainite: 14 °C/s (3%M/97%B), 17 °C/s (12%M/88%B), 24 °C/s (57%M/43%B) 28 °C/s (86%M/14%B), 50 °C/s (97%M/3%B).

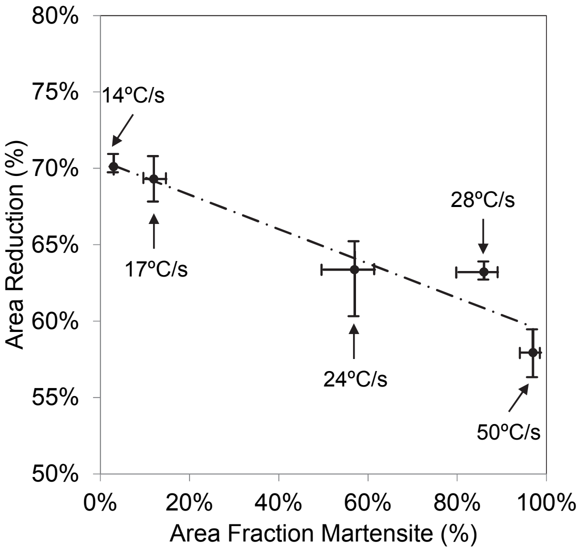

Figure 13 - Percent area reduction versus % area fraction martensite as measured from the quasi-static (0.003 s^{-1}) tension tests. Note that 0% and 100% area fraction martensite refers to 100% and 0% area fraction bainite, respectively. The vertical and horizontal error bars indicate the maximum and minimum measured values from the repeat measurements.

The true stress versus effective plastic strain (or flow stress) curves generated at the various strain rates and various area fractions of martensite/bainite were used to develop a strain rate sensitive constitutive model. Initially, the Johnson-Cook (JC) [44,45] constitutive model was fit to the data, but it was shown that the strain hardening behavior and stress saturation of the martensitic material conditions could not be captured by the continuously hardening function that defines the JC model. The Zerilli-Armstrong model was also fit to the data, but the strain rate sensitivity for all of the material conditions predicted unrealistic model parameters. It was shown that the Voce [46] hardening law (equation 1) with an exponential-type strain rate sensitivity term accurately captured the hardening behavior and strain rate sensitive response for all of the material conditions examined in this work.

$$\sigma = f(\varepsilon, \dot{\varepsilon}) = \left[A + \left[[B - A]e^{\left(-\frac{\varepsilon}{C}\right)}\right]\right][1 + \dot{\varepsilon}]^{D} \tag{1}$$

Using the Voce parameters (A, B, C, D) fit to each individual material condition, mathematical functions relating the parameters with respect to Vickers hardness (HV) were found and a phenomenological constitutive model, referred to as the "Tailored Crash Model (TCM)" was developed. The purpose of this model is to predict the flow stress behavior of the tailored material conditions as a function of effective plastic strain (ε), true strain rate $(\dot{\varepsilon})$ and Vickers hardness (HV) as shown in equation 2. The excellent agreement between the predicted (TCM) and measured flow stress curves can be seen in Figure 14.

$$\sigma = f(\varepsilon, \dot{\varepsilon}, HV) = \left[A(HV) + \left[[B(HV) - A(HV)]e^{\left(-\frac{\varepsilon}{C(HV)}\right)}\right]\right][1 + \dot{\varepsilon}]^{D(HV)} \qquad (2)$$

This model can alternatively be expressed as a function of the area fraction martensite, due to the linear relationship between Vickers hardness (HV) and area fraction martensite $(\%M)$ as measured from the experiments and shown in equation (3). For a given a $(\%M)$ the balance of the area fraction is bainite.

$$HV = 217.85 \cdot (\%M) + 236.15 \qquad (3)$$

With the current TCM, a hot stamping finite element (FE) simulation can be conducted and the as-quenched volume fraction of martensite and bainite for each element can be used to define the crash properties for a subsequent impact FE model by implementing the numerical procedure outlined by Bardelcik et al. [47].

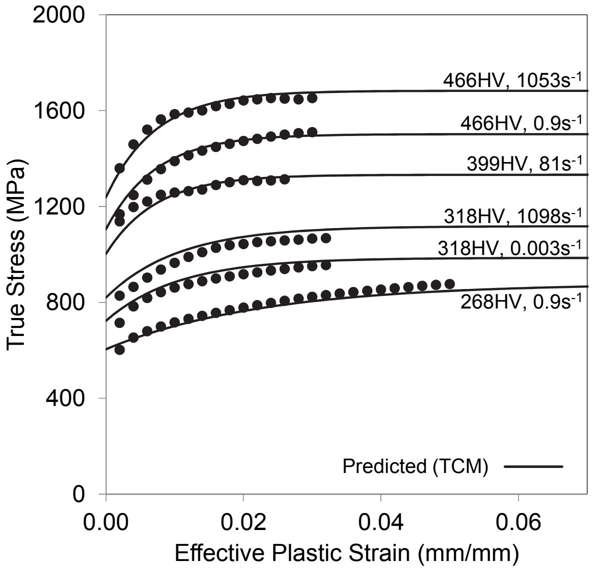

Figure 14 - The measured (symbols) and TCM predicted (curves) flow stress curves for a variety of as-quenched Vickers hardness and strain rate values. The following hardness values correspond to the following measured area fraction martensite/bainite: 268 HV (3%M/97%B), 318 HV (12%M/88%B), 399 HV (57%M/43%B) 442 HV (86%M/14%B), 466 HV (97%M/3%B).

4.3 Part 3: The Influence of Martensite, Bainite and Ferrite on the As-Quenched Constitutive Response of Simultaneously Quenched and Deformed Boron Steel – Experiments and Model

The formation of ferrite within the as-quenched microstructure of a tailored hot stamping has been shown to occur due to the application of plastic deformation during quenching as reviewed in section 2.4. This phenomenon was observed by George et al. [1] for a hot stamped, lab-scale B-pillar component that was produced at the University of Waterloo using in-die heating to produce regions of tailored properties. Understanding the influence of ferrite within a mixed multiphase material containing martensite, bainite and ferrite was the motivation for this part of the work, which focused on: (i) simultaneously quenching and deforming USIBOR® 1500P boron steel, (ii) characterizing the as-quenched microstructure (iii), evaluating the mechanical properties, and (iv) developing a new constitutive model.

A Gleeble 3500 thermal-mechanical apparatus was used to simultaneously quench and deform boron steel blanks at three different cooling rates (10, 15 and 30 °C/s) and two different deformation temperatures (T_{DEF}=800 °C and 600 °C) as shown in temperature versus time schematics in Figure 15. The imposed deformation during the quenching process was ε_{DEF} = ~0.2 strain in each case. A no deformation (ND) condition experiment was also carried out for each of the three different cooling rates.

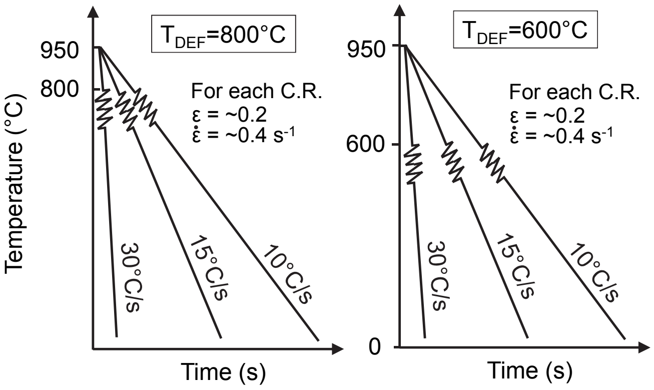

Figure 15 - Temperature versus time schematic for the two hot deformation temperature conditions.

The hardness of the as-quenched materials reduced as the quench rate reduced, which is expected from the work presented in Parts 1 and 2 of this thesis. The effect of deformation during quenching also reduces the as-quenched hardness, with the greatest reduction occurring for deformation occurring at the lower temperature (T_{DEF}) of 600 °C, as shown in Figure 16. Scanning electron microscope and colour tint etched optical micrographs were generated for the various quenched/deformed conditions (Figure 16) and revealed that for most of the deformation conditions, ferrite was present within the microstructure as presented in Table 2. It was also observed that the morphology of the bainite phase changed from an upper bainite-type (UB) structure when no deformation was imposed, to a granular bainite (GB) structure when deformation was imposed as shown in Figure 16.

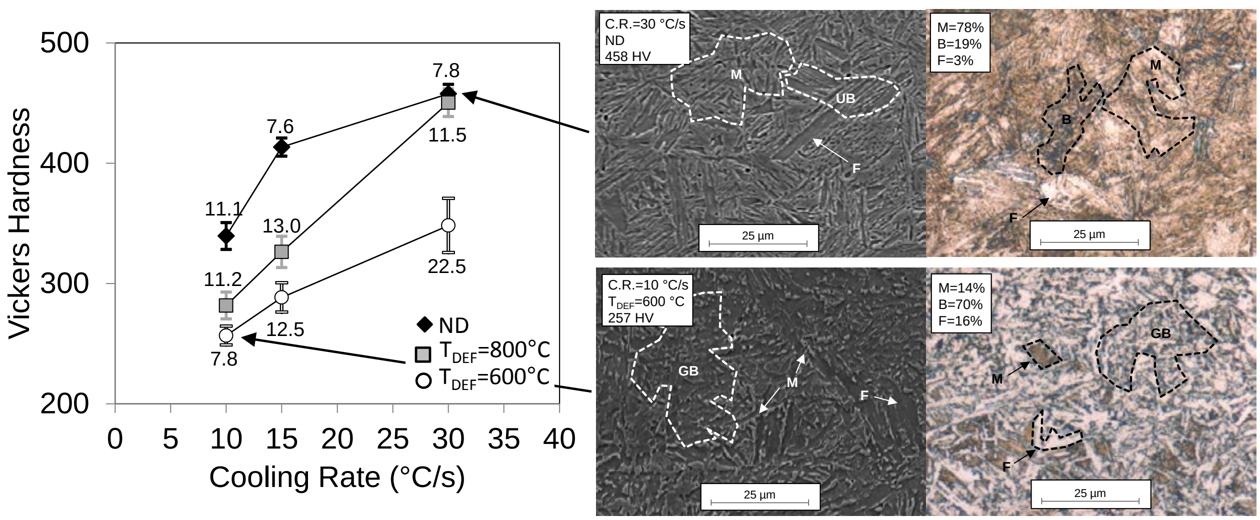

Figure 16 - Vickers hardness versus cooling rate. The error bars indicate +/- the standard deviation as measured from the population of repeat measurements and the values adjacent to the data points indicate the calculated standard deviation. (ND = no deformation). SEM micrographs and color tint-etched optical micrographs for two different quench/deformation conditions. F=ferrite, UB=upper bainite-type, GB=granular bainite.

Table 2 - Summary of the area fraction measurements.

Cooling Rate (°C/s)	T_{DEF} (°C)	Avg. Vickers Hardness	Avg. Area Fraction Martensite, M (%)	Avg. Area Fraction Bainite, B (%)	Avg. Area Fraction Ferrite, F (%)
10	ND	339	22	72	6
	800	282	17	71	12
	600	257	14	70	16
15	ND	413	57	37	6
	800	326	53	29	18
	600	288	12	76	12
30	ND	458	78	19	3
	800	450	71	27	2
	600	348	37	49	14

Miniature dog-bone style tensile specimens were cut from the quenched and deformed blanks and subsequently tested in uniaxial tension at a quasi-static strain rate of 0.003 s^{-1} using an Instron. The tensile specimens were also tested at intermediate strain rates (10 s^{-1} and 80 s^{-1}) using the Hydraulic Intermediate Strain Rate (HISR) apparatus that was developed as a part of this work and is described in detail in Part 3. The stress versus strain curves generated from the quenched and deformed specimens revealed that the presence of ferrite within the tailored microstructure resulted in almost no change in yield strength (σ_Y) and a slight increase in ultimate tensile strength (σ_{UTS}) when compared, at an equivalent hardness, to the tailored microstructure of the FAQA specimens (Part 2) that were devoid of ferrite. A plot of σ_Y and σ_{UTS} versus hardness for the quenched and deformed and FAQA specimens is shown in Figure 17a. Although there was little change in material strength due to the presence of ferrite, the uniform elongation increased noticeably for a given hardness level less than ~350 HV, as plotted in Figure 17b.

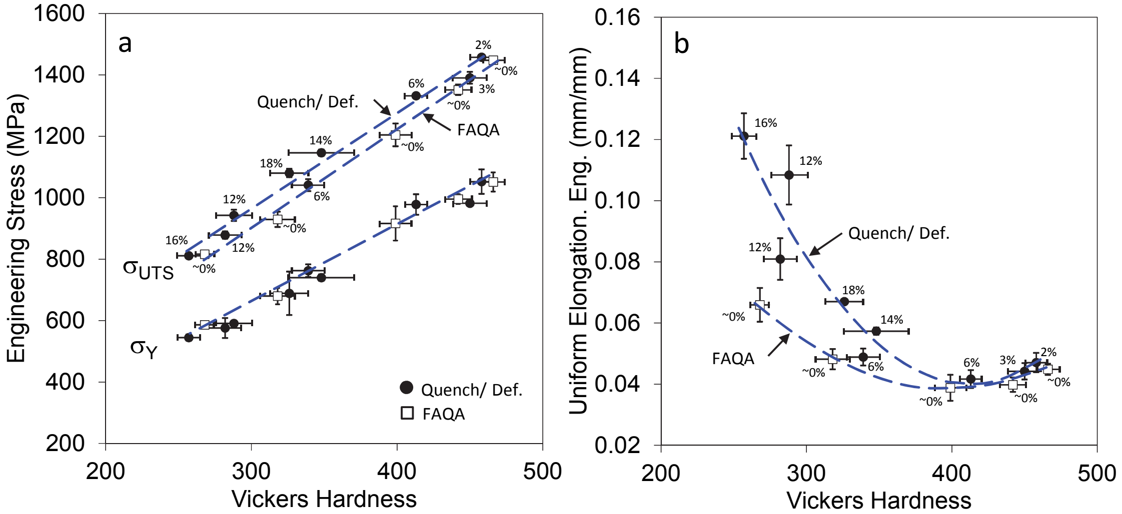

Figure 17 - (a) The measured ultimate tensile strength (σ_{UTS}) and 0.2% yield strength (σ_Y) versus average Vickers hardness from the quasi-static tension tests conducted at a strain rate of 0.003 s^{-1} (b) The average uniform elongation versus the average measured Vickers hardness. The percent values indicate the average measured area fraction of ferrite within the microstructure. The error bars indicate +/- the standard deviation as measured from the population of repeat test results. The FAQA results are those measured from Part 2.

The increase in uniform elongation can be seen in Figure 18 which serves to compare the average stress versus strain curves at material conditions with similar hardness levels. For the two pairs of curves with a hardness of ~260 HV and ~330 HV, the material exhibits similar strength levels and a larger uniform elongation strain when the amount of ferrite present within the microstructure increases.

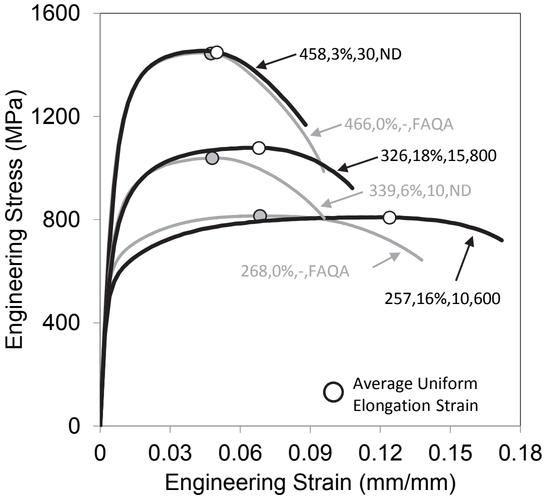

Figure 18 - The effect of area fraction of ferrite on the uniform elongation strain. Shown for a variety of as-quenched material conditions. Average engineering stress versus strain curves for a variety of as-quenched material conditions tested in this work and from the FAQA experiments (Part 2). The tensile tests were conducted at a strain rate of 0.003 s-1 and the label corresponding to each curve indicates: [avg. Vickers hardness, avg. measured area fraction of ferrite, cooling rate, deformation condition].

By fitting the true stress versus true strain data with the power law function due to Holloman [48] and quantifying the strain hardening exponent (*n*-value), it was shown that the increased uniform elongation strain also corresponds to an increase in the *n*-value, which indicates greater strain hardening due to the presence of ferrite within the as-quenched microstructure as shown in Figure 19a. The elevated uniform elongation strain and greater *n*-value result in greater energy absorption capacity of the quenched and deformed material containing ferrite. Energy absorption was quantified as the toughness, which is plotted in Figure 19b. At hardness levels less than ~350 HV, the quenched and deformed material containing ferrite indicate improved energy absorption capacity when compared to the material devoid of ferrite. It was shown that a material with a bainitic microstructure containing 16% ferrite (with 257 HV) resulted in a 28% increase in energy absorption when compared to a material that was fully bainitic with a hardness of 268 HV as shown in Figure 19b. The toughness distribution shown in Figure 19b also shows that as-quenched materials with hardness values ranging from approximately 300 HV to 425 HV exhibited a lower reduced energy absorbing capacity, which must be considered during the design/development of a hot stamped component with tailored properties.

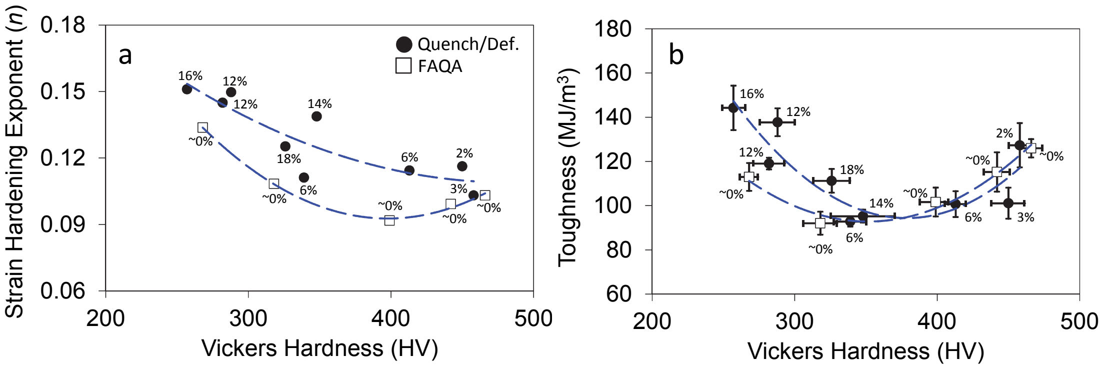

Figure 19 – (a) The strain hardening exponent (*n*) versus the Vickers hardness for the quenched and deformed specimens (b) The average toughness (or energy absorption) versus the Vickers hardness for the quenched and deformed specimens. Also included is the data for the specimens quenched in the FAQA, from Part 2. The percent values indicate the average measured area fraction of ferrite within the microstructure.

The effect on increasing the loading rate revealed only moderate strain rate sensitivity as shown by the increase in σ_Y and σ_{UTS} (Figure 20), due to an increase in strain rate from 0.003 s^{-1} to 80 s^{-1}.

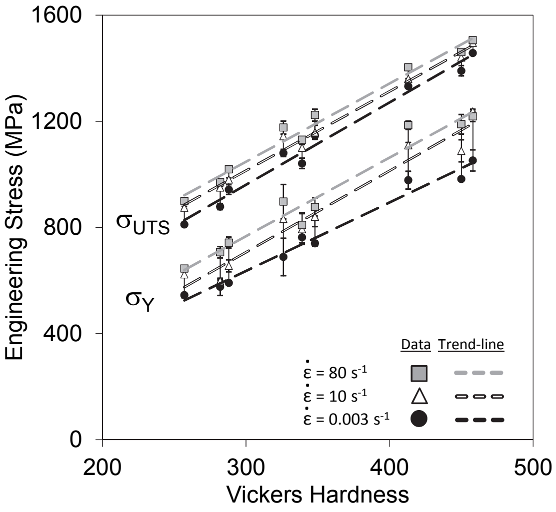

Figure 20 - The ultimate tensile strength (σ_{UTS}) for and 0.2% yield strength (σ_Y) versus Vickers hardness for all of the quenched and deformed specimens tested at nominal strain rates of 0.003 s^{-1}, 10 s^{-1} and 80 s^{-1}.

True stress versus effective plastic strain (or flow stress) curves were generated for all of the various material conditions and strain rates tested in this work. This flow stress data, along with the FAQA flow stress data from Part 2, was used to develop the “Tailored Crash Model II (TCM II)”, which is a constitutive model that is an extension of the TCM (Part 2) and is now a function of effective plastic strain (ε), true strain rate $(\dot{\varepsilon})$, the martensite – bainite area fraction relationship $[M/(M+B)]$ and the area fraction ferrite (F) as shown in equation 4 below,

$$\sigma = f\left(\varepsilon, \dot{\varepsilon}, [\tfrac{M}{M+B}], F\right) = \left[A\left([\tfrac{M}{M+B}], F\right) + \left[\left[B\left([\tfrac{M}{M+B}], F\right) - A([\tfrac{M}{M+B}], F)\right] e^{\left(-\varepsilon/C([\frac{M}{M+B}],F)\right)}\right]\right][1+\dot{\varepsilon}]^{D} \qquad (4)$$

The TCM II is based on the same Voce hardening law with exponential-type strain rate sensitivity term as shown in equation 1. Rather than fitting the model parameters (A, B, C, D) with respect to Vickers hardness, three dimensional surface functions were found to fit each of the Voce model parameters with respect to the martensite – bainite area fraction relationship $[M/(M+B)]$ and the area fraction ferrite (F). The TCM II accurately captures the constitutive behavior of the tailored material conditions tested in this work for all of the strain rates as shown in Figure 21. The model was also shown to be able to predict the FAQA specimen flow stress data (at various strain rates) measured in Part 2.

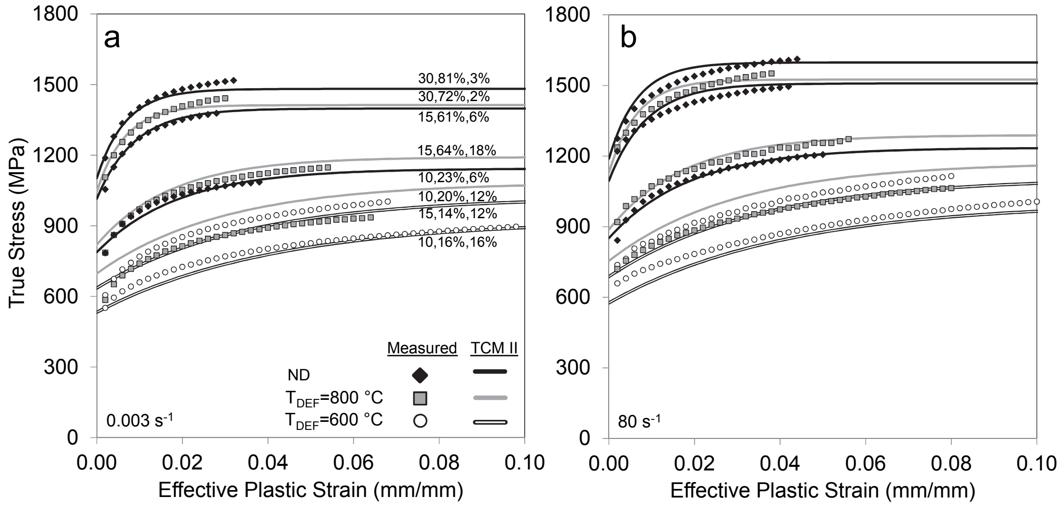

Figure 21 - The measured and predicted (TCM II) flow stress curves for the quenched and deformed specimens pulled at a strain rate of (a) 0.003 s^{-1} and (b) 80 s^{-1}. The T$_{DEF}$=600 °C and 30 °C/s results were omitted for clarity. The numbers adjacent to the predicted curves indicate (cooling rate °C/s, [$M/(M+B)$], F).

4.4 Part 4: Transition Zone Tensile Properties within a Tailored Hot Stamping

Validation of constitutive models against independently generated experimental data is crucial for building confidence in the model and is generally considered good practice amongst the modeling community. Although the Tailored Crash Model (TCM) from Part 2 was successfully validated against the data used to fit the model, it was important to validate the model against experiments conducted on actual hot stamped materials. This was the motivation for Part 4, in which tensile tests were conducted on specimens that were cut from the transition zone of the hot stamped part developed by George et al. [1] which incorporates tailored properties. A finite element (FE) model of the tensile tests was developed and the true stress versus effective plastic strain (or flow stress) curves used within the model were defined by the TCM. It should be noted that an earlier implementation of the TCM, which incorporated a logarithmic strain rate sensitivity term, rather than the exponential term was used as shown in equation 5. Although the strain rate term was different, the strain rate sensitive constitutive behaviour was predicted with nearly the same accuracy. Also, the tests that were modeled in Part 4 were conducted at quasi-static strain rates.

$$\sigma = f(\varepsilon, \dot{\varepsilon}, HV) = \left[A(HV) + \left[[B(HV) - A(HV)]e^{\left(-\frac{\varepsilon}{C(HV)}\right)}\right]\right][1 + D(HV) \cdot ln(\dot{\varepsilon})] \qquad (5)$$

For the experimental part of this work, tensile dog-bone specimens were extracted from the transition zone of the lab-scale B-pillar created due to the work of George et al. [1]. Figure 22a shows a CAD image of the heated and cooled tooling that was used to create the tailored B-pillar part using the in-die heating technique. The hard and soft zone of the hot stamped part are indicated in Figure 22b, along with the transition zone that is due to the air gap present in the hot stamping tool. Sub-sized ASTM-E8 tensile specimens were extracted from various locations at the transition zone shown in Figure 22b. The material properties varied across the gauge length of the tensile specimen for which the hardness indicated a transition from fully martensitic (450 HV) to fully bainitic (265 HV) microstructure. The tensile specimens were pulled in tension and the stress-strain response was measured. Also, digital image correlation (DIC) techniques were used to measure the strain distribution during tensile loading, which provided additional validation for the FE models.

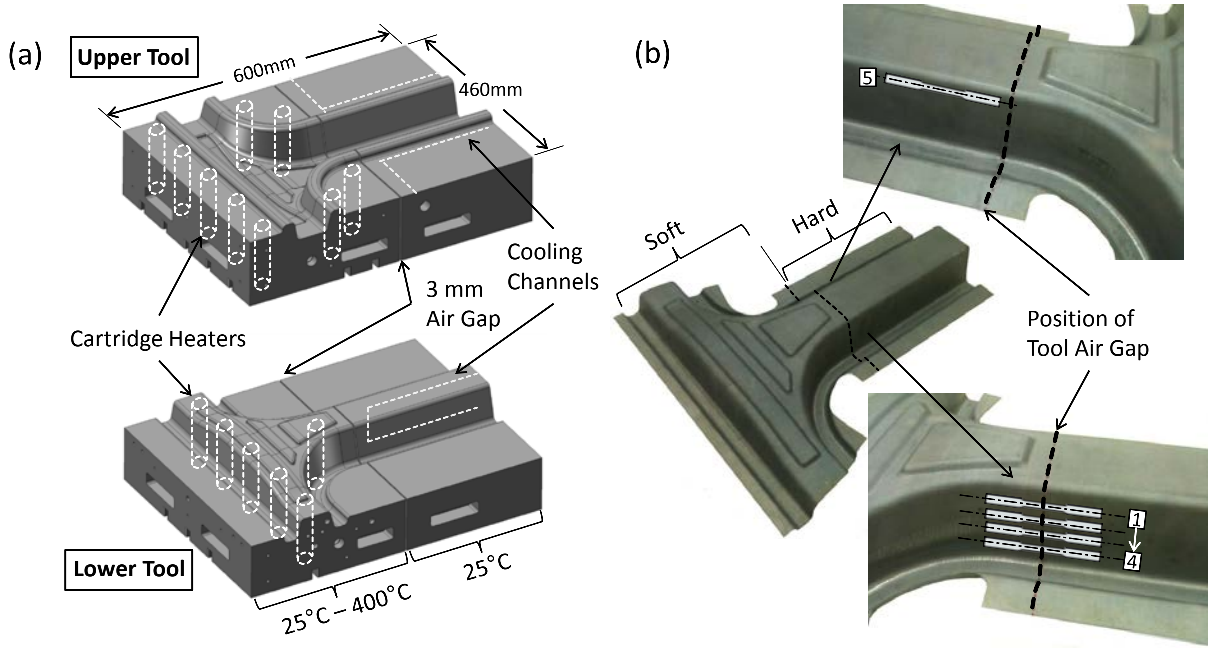

Figure 22 - a) A CAD image of the heated/cooled hot stamping die set (b) A photograph of a hot stamped part with the transition zone specimen locations highlighted. The dashed line indicates the location of the 3 mm air gap in the tool which represents the middle of the transition zone. Copyright © SAE International. Reprinted with permission from SAE paper 2012-01-0531.

A finite element (FE) model (Figure 23a) of the transition zone tensile specimens was created and loaded using boundary conditions corresponding to those in the experiments. The material flow stress curves defined for the FE model were generated using the TCM (equation 5) based on the measured Vickers hardness distribution along the length of the tensile specimens. A sample of the variation in flow stress (as predicted by equation 5) due to hardness and strain rate is shown in Figure 23b.

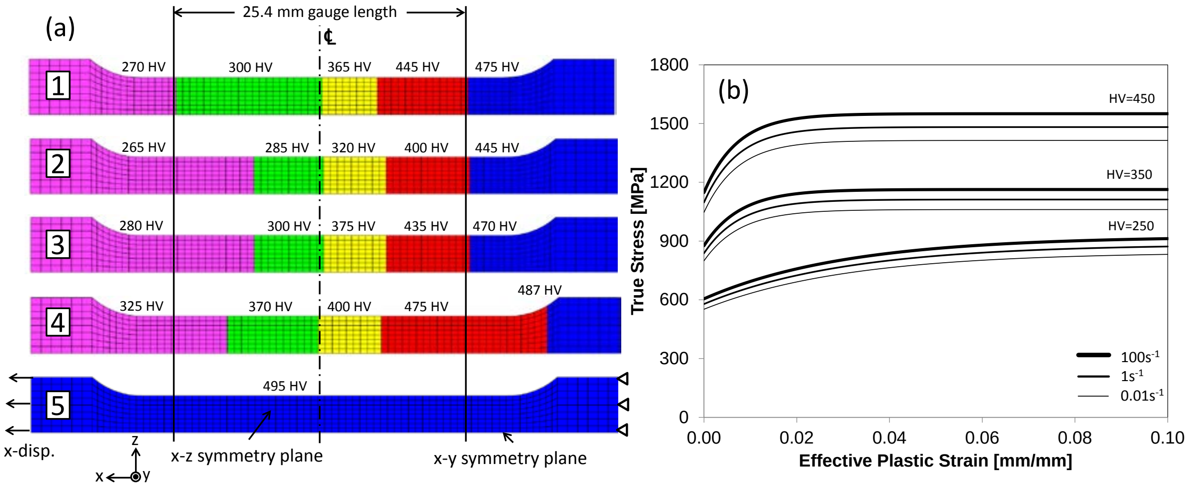

Figure 23 - a) Finite element mesh of the tensile specimens cut from location 1 to 5. (b) A sample of flow stress curves generated using the TCM from Article 2 with a logarithmic strain rate sensitivity term. Copyright © SAE International. Reprinted with permission from SAE paper 2012-01-0531.

Material properties corresponding to the measured hardness distribution within each specimen were mapped onto the finite element mesh and the material stress versus strain data was assigned using a point-wise stress-strain-strain rate material model according to the procedure described by Bardelcik et al. [47]. The FE simulation of the tension tests accurately reproduced the experimentally measured engineering stress versus strain curves, as seen in Figure 24a. The DIC analysis of the strains within tensile samples also revealed that the FE model predicted the measured strain distribution well, as shown in Figure 24b.

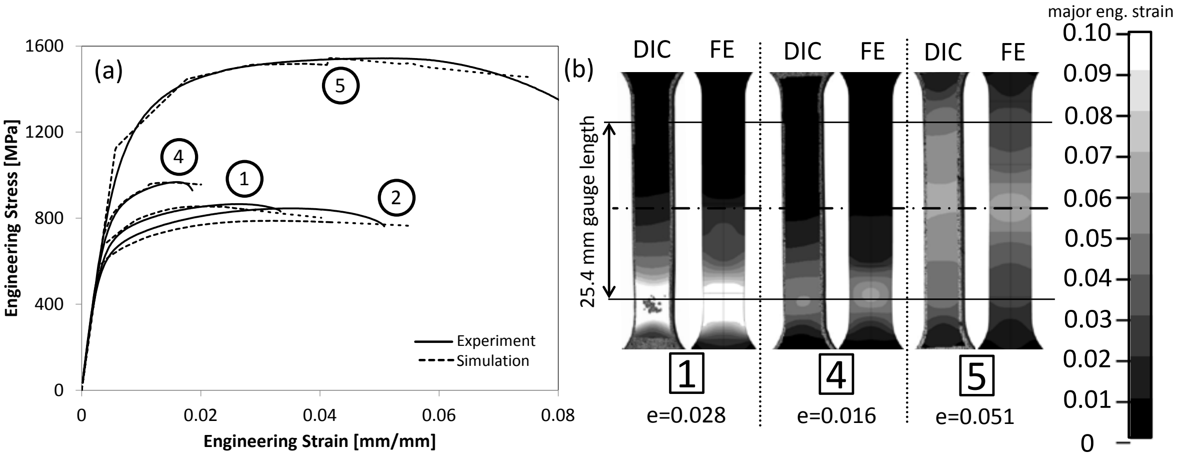

Figure 24 – (a) The measured and predicted engineering stress vs. engineering strain curves for the location 1,2,4 and 5 specimens. The location 3 results were omitted for clarity. (b) The measured (DIC) and predicted (FE) major engineering strain distributions at the strain state indicated. The framed numbers indicate the specimen location within the hot stamped part (Figure 22). Copyright © SAE International. Reprinted with permission from SAE paper 2012-01-0531.

5 DISCUSSION

The research presented in this thesis has successfully characterized the high strain rate mechanical response of USIBOR$^{®}$ 1500P boron steel with tailored properties imparted through a thermal-mechanical route which simulates a hot stamping process with in-die heating. In general, the low hardness regions within tailored hot stampings were shown to exhibit reduced strength, improved ductility and good energy absorption properties. These characteristics indicate that a hot stamped component with tailored properties may offer improved crash performance. The strain-rate sensitive constitutive models developed in this work can be directly applied to finite element (FE) simulations of component-level or full-vehicle impact models that utilize hot stamped components with tailored properties. These models are needed to support the design and development of vehicle crash structures incorporating tailored hot stamped parts.

From a material response perspective, it was shown that a tailored material condition consisting of bainite has improved ductility compared to a fully martensitic material condition, with comparable energy absorption. These mechanical properties suggest that a hot stamping with a tailored region consisting of bainite may be desirable because such a region can locally absorb impact energy during crash and resist fracture in regions that are inherently susceptible to cracking due to geometric constraints. The increased reduction in area for an increasingly more bainitic material condition corresponds to improved ductility, which is also attractive from an energy absorption perspective.

Plastic deformation during quenching results in the transformation of austenite into ferrite at cooling rates near or below the critical cooling rate. The current mechanical characterization efforts have demonstrated that the presence of ferrite within a tailored microstructure not only increases the UTS of the material (for an equivalent hardness), but also increases the uniform elongation and strain hardening behavior (*n*-value) for hardness levels less than ~350 HV. The presence of ferrite with the low strength and high ductility within the tailored microstructure resulted in a more ductile behavior, which ultimately improved the energy absorption capacity. With this desirable increase in energy absorption or toughness, it may be possible to design future processing strategies to intentionally introduce elevated levels of strain to improve overall crash performance. Regardless of whether such a strategy can be implemented in practice, the current work provides a constitutive model that accounts for the presence of ferrite resulting from deformation during quenching.

It was also observed that the morphology of the bainite present in the as-quenched microstructure changed from an upper bainite-type lath structure, when no deformation was imposed during quenching, to a granular bainite structure (with ferrite regions) when simultaneous deformation was operative during quenching. The effect of bainite morphology on the mechanical response of tailored components has to be further investigated to reveal what degree of influence it has on the energy absorption capacity of the material.

For all of the tailored microstructures examined in this work, it was revealed that intermediate as-quenched hardness, values ranging from approximately 300 HV to 425 HV, resulted in reduced energy absorption capacity, which must be considered during the design/development of a hot stamped component with tailored properties. Interestingly, the current work on tensile testing of transition zones (Part 4) has not revealed any embrittling effect of this lower toughness material within the transition between high and low hardness phases.

In terms of industrial viability, the lab-scale hot stamping process with in-die heating reported by George et al. [1] has successfully produced a hot stamped part with a tailored region consisting primarily of bainite that meets industrial targets for as-formed properties and manufacturability. Other researchers [31-37] have also examined the hot stamping process with in-die heating, but those studies have not provided in-depth characterization of the as-quenched stress-strain response and mechanical properties that result for the as-quenched and multiphase microstructures. Other tailoring techniques, such as hot stamping of non-boron alloyed steel [49] and varying austenization temperatures with subsequent quenching [50] have also been studied, but the as-quenched microstructures resulting from these tailoring techniques differ from those that are achieved due to in-die heating. The most novel contribution stemming from this thesis are the strain rate sensitive constitutive models that can be used to define finite element (FE) constitutive properties needed to model the in-service crash response of such tailored components. These models accurately capture both the strain hardening response and the strengthening effect due to elevated loading rates for the range of phases present in hot stampings produced using in-die heating tailoring techniques. Such models represent an important tool for future vehicle structure design, optimization and validation, which precedes the development of an actual part. These models should serve to improve the accuracy of crash simulation; in addition, they can be used to optimize the hot stamping process itself, by identifying the critical regions that will benefit from introduction of tailored properties.

6 CONCLUSIONS

The following conclusions are drawn from this research:

- The as-quenched microstructure due to cooling rates of 45 °C/s and 250 °C/s resulted in the formation of 100% martensite, for which the quasi-static ultimate tensile strength (UTS) and hardness were approximately 1,450 MPa and 476 HV, respectively. Optical micrographs of specimens quenched at 2,200 °C/s revealed that the martensitic microstructure was refined (compared to 45 °C/s and 250 °C/s) which most likely contributed to the elevated UTS of 1,620 MPa and hardness of 516 HV for this condition. The strain rate sensitivity was shown to be moderate for the specimens quenched at 45 °C/s and 250 °C/s, and minimal for the specimens quenched at of 2,200 °C/s.

- Specimens quenched at and below the critical cooling rate (< ~27 °C/s) resulted in as-quenched tailored microstructures that varied from bainitic to martensitic, for which the measured Vickers hardness varied linearly with respect to the area fraction of martensite and bainite. The UTS and strain at failure of the martensitic material condition was 1,447 MPa and 0.10, respectively, while the UTS and strain at failure of the bainitic material condition was 816 MPa and 0.15 strain, respectively. The fracture surface reduction in area also increased from 58% to 70% as the microstructure varied from martensitic to bainitic. The overall mechanical properties measured for the bainitic material condition indicate that a tailored microstructure consisting of bainite may be a desirable candidate material condition for implementation within a hot stamped structural component for improved crash performance.

- For as-quenched tailored microstructures consisting of martensite, bainite and ferrite, the presence of ferrite was shown to slightly improve the UTS without affecting the yield strength for material conditions with similar Vickers hardness values. The presence of ferrite in the tailored microstructure also noticeably increased the uniform elongation and hardening behavior (*n*-value) which resulted in improved material toughness (or energy absorption capacity) for hardness values less than ~350 HV. The improvement in energy absorption due to the presence of 16% ferrite within a 257 HV predominantly bainitic microstructure was 28% when compared to a bainitic material condition that was void of ferrite, but of similar hardness.

- All of the as-quenched material conditions tested in this work (except for the 2,200 °C/s case) displayed moderate strain rate sensitivity as measured from uniaxial tensile data generated at a various strain rates (0.003 s^{-1} to ~1,075 s^{-1}). The tensile data was used to develop the "Tailored Crash Model (TCM)" which was shown to accurately reproduce the measured flow stress data as a function of effective plastic strain, true strain rate and Vickers hardness (or area fraction martensite) for materials ranging in microstructure from martensite to bainite. The "Tailored Crash Model II (TCM II)", which introduced the effect of ferrite on the constitutive response, also accurately reproduced the measured flow stress data as a function of effective plastic strain, true strain rate and area fractions of martensite, bainite and ferrite.

- The TCM constitutive model was validated against uniaxial tension tests conducted on specimens that were extracted from the transition zone of a tailored hot stamping and varied in hardness from 459 HV to 265 HV along the gauge length. The measured hardness distributions were used to define the finite element (FE) constitutive response for models of the experiments. The measured stress versus strain response was in excellent agreement with FE models, as was the strain distribution during loading that was measured using digital image correlation.

7 FUTURE WORK

The following future work is proposed as next steps to support the commercial implementation of tailored hot stampings:

- The constitutive models developed in this work have been validated primarily for uniaxial loading and it was assumed that the materials behave in an isotropic manner. Future work will consider multi-axial loading and variations in strain paths to fully validate the model and assumptions made in this work.

- Develop a fracture criterion that is based on the variation of martensite, bainite and ferrite within the as-quenched microstructure. Such a fracture criterion will improve the accuracy of finite element crash simulations.

- Validate the TCM II constitutive model and fracture criterion against impact experiments on hot stamped components with tailored properties.

- Identify whether it is feasible to develop a hot stamping process in which deformation can be imposed throughout the blank during quenching to form ferrite within tailored regions for enhanced energy absorption.

- Conduct a rigorous metallographic examination of the as-quenched multiphase material conditions to understand the dislocation dynamics at play and how they contribute to the measured constitutive response. This would require advanced metallographic experimental techniques such as TEM and XRD.

REFERENCES

[1] George R, Bardelcik A, Worswick MJ. Hot forming of boron steels using heated and cooled tooling for tailored properties. *Journal of Materials Processing Technology,* **212** (11), 2386-99, 2012.

[2] Altan T. Hot-stamping boron-alloyed steels for automotive parts, Part I: Process methods and used. *Stamping Journal Magazine* , 40-1, 2006.

[3] Aspacher J. Forming hardening concepts. *1st International Conference on Hot Sheet Metal Forming of High-Performance Steel*, Kassel, Germany, 77-81, 2008.

[4] Hein P. A global approach of the finite element simulation of hot stamping. *Advanced Materials Research,* **6-8**, 763-70, 2005.

[5] Jonsson M. Press hardening, from innovation to global technology. *1st International Conference on Hot Sheet Metal Forming of High-Performance Steel*, Kassel, Germany, 253-265, 2008.

[6] Akerstrom P. Modelling and simulation of hot stamping, PhD, University of Lulea, 2006.

[7] Babbit M. Some highlights on new steel products for automotive use. *Steel Research International,* **77** (9-10), 620-6, 2006.

[8] Karbasian H, Tekkaya AE. A review on hot stamping. *Journal of Materials Processing Technology,* **210** (15), 2103-18, 2010.

[9] Maikranz-Valentin M, Weidig U, Schoof U, Becker HH, Steinhoff K. Components with optimised properties due to advanced thermo-mechanical process strategies in hot sheet metal forming. *Steel Research International,* **79** (2), 92-7, 2008.

[10] Munera DD, Pinard F, Lacassin L. Very and ultra high strength steels based tailored welded blanks: A step further towards crashworthiness improvement. *SAE Transactions: Journal of Materials & Manufacturing,* **115** (2006 Transactions), 796-804, 2007.

[11] Munera DD, Pic A, Abou-Khalil D, Shmit F, Pinard F. Innovative press hardened steel based laser welded blanks solutions for weight savings and crash safety improvements. *SAE International Journal of Materials & Manufacturing,* **1** (1), 472-9, 2009.

[12] Rusinek A, Cheriguene R, Baeumer A, Klepaczko IR, Larour P. Dynamic behaviour of high-strength sheet steel in dynamic tension: Experimental and numerical analyses. *Journal of Strain Analysis for Engineering Design,* **43** (1), 37-53, 2008.

[13] Salisbury CP, Worswick MJ, Mayer R. High rate constitutive modeling of aluminium alloy tube. *Journal de Physique (France) IV,* **134** (Eurodymat 2006; Suppl.), 43-8, 2006.

[14] Huh H, Lim J, Park S. High speed tensile test of steel sheets for the stress-strain curve at the intermediate strain rate. *International Journal of Automotive Technology,* **10** (2), 195-204, 2009.

[15] Uenishi A, Yoshida H, Kuriyama Y, Takahashi M. Material characterization at high strain rates for optimizing car body structures for crash events. , 22-6, 2003.

[16] Mahadevan K and Liang P. Effect of strain rate in full vehicle frontal crash analysis. *2005 SAE World Congress*, Detroit, Michigan, USA, 2000.

[17] Mahadevan K, McCoy R, Faruque O, Schell B. Strain-rate characterization of automotive steel and the effect of strain-rate in component crush analysis. *1998 SAE World Congress*, Detroit, USA, 1998.

[18] Simunovic S, Nukala PKVV, Fekete J, Meuleman D, Milititsky M. Modeling of strain rate effects in automotive impact. *SAE Transactions: Journal of Materials & Manufacturing,* **112**, 733-43, 2004.

[19] Chen XM, Shi MF, Chen G, Kamura M, Watanabe M, Omyia Y. Crash performances of advanced high-strength steels of DP780, TRIP780 and DP980. *2005 SAE World Congress*, Detroit, Michigan, USA, 2005.

[20] Wood PKC, Schley CA, Buckley M, Walker B, Dutton T. Validating dynamic tensile mechanical properties of sheet steels for automotive crash applications. *6th European LS-DYNA Users' Conference*, 2007.

[21] Abedrabbo N, Mayer R, Thompson A, Salisbury C, Worswick M, van Riemsdijk I. Crash response of advanced high-strength steel tubes: Experiment and model. *International Journal of Impact Engineering,* **36** (8), 1044-57, 2009.

[22] Hein P, Wilsius J. Status and innovation trends in hot stamping of USIBOR 1500 P. *Steel Research International,* **79** (2), 85-91, 2008.

[23] Erhardt R and Boke J. Industrial application of hot forming process simulation. *1st International Conference on Hot Sheet Metal Forming of High-Performance Steel*, Kassel, Germany, 83-88, 2008.

[24] Krauss G. Deformation and fracture in martensitic carbon steels tempered at low temperatures. *Metallurgical and Materials Transactions A-Physical Metallurgy and Materials Science,* **32** (4), 861-77, 2001.

[25] Laumann T, Pfestorf M, Beil A, Geiger M, Merklein M. Crash behaviour of various modern steels exposed to high deformation rates. *Key Engineering Materials,* **344**, 151-8, 2007.

[26] Labudde T and Bleck W. Formability characteristics of press hardened steels. *2nd International Conference on Hot Sheet Metal Forming of High-Performance Steel*, Lulea, Sweden, 127-135, 2009.

[27] Casas B, Latre D, Rodriguez N, Valls I. Tailor made tool materials for the present and upcoming tool solutions in hot sheet metal forming. *1st International Conference on Hot Sheet Metal Forming of High-Performance Steel*, Kassel, Germany, 23-35, 2008.

[28] Picas I, Hernandex R, Casellas D, Valls I. Cold cutting of microstructurally tailored hot formed components. *2nd International Conference on Hot Sheet Metal Forming of High-Performance Steel*, Lulea, Sweden, 115-125, 2009.

[29] ArcelorMittal – USIBOR® 1500P CCT Diagram. *ArcelorMittal* , 2009.

[30] Barcellona A, Palmeri D. Effect of plastic hot deformation on the hardness and continuous cooling transformations of 22MnB5 microalloyed boron steel. *Metallurgical and Materials Transactions A,* **40** (5), 1160-74, 2009.

[31] Svec T and Merklein M. Tailored tempering - heat transfer and resulting properties in dependecny of tool temperatures. *3rd International Conference on Hot Sheet Metal Forming of High-Performance Steel*, Kassel, Germany, 21-29, 2011.

[32] Graff S, Gerber T, Lenze F, Sikora S. About the simulation of microstructure evolution in the hot sheet stamping process and the correlation of resulting mechanical properties and crash-performance. *3rd International Conference on Hot Sheet Metal Forming of High-Performance Steel*, Kassel, Germany, 323-330, 2011.

[33] Erturk S, Sester M, Selig M, Feuser P, Roll K. A thermo-mechanical-metallurgical FE approach for simulation of tailored tempering. *3rd International Conference on Hot Sheet Metal Forming of High-Performance Steel*, Kassel, Germany, 447-454, 2011.

[34] Feuser P, Schweiker T, Merklein M. Partially hot-formed parts from 22MnB5 - process window, material characteristics and component test results. *10th International Conference on Technology of Plasticity*, Achen, Germany, 408-413, 2011.

[35] Banik J, Lenze FJ, Sikora S, Laurenz R. Tailored properties - a pivotal question for hot forming. *3rd International Conference on Hot Sheet Metal Forming of High-Performance Steel*, Kassel, Germany, 13-20, 2011.

[36] Oldenburg M and Lindkvist G. Tool thermal cycle design for manufacturing of components with tailored material properties. *3rd International Conference on Hot Sheet Metal Forming of High-Performance Steel*, Kassel, Germany, 203-210, 2011.

[37] Merklein M and Svec T. Transformation kinetics of the hot stamping steel 22MnB5 in dependency of the applied deformation on the austenitic microstructure. *IDDRG 2010*, Graz, Austria, 71-81, 2010.

[38] Min J, Lin J, Min Y, Li F. On the ferrite and bainite transformation in isothermally deformed 22MnB5 steels. *Materials Science & Engineering A,* **550**, 375-87, 2012.

[39] Naderi M, Saeed-Akbari A, Bleck W. The effects of non-isothermal deformation on martensitic transformation in 22MnB5 steel. *Materials Science and Engineering A,* **487** (1-2), 445-55, 2008.

[40] Nikravesh M, Naderi M, Akbari GH. Influence of hot plastic deformation and cooling rate on martensite and bainite start temperatures in 22MnB5 steel. *Materials Science & Engineering A,* **540**, 24-9, 2012.

[41] Abbasi M, Saeed-Akbari A, Naderi M. The effect of strain rate and deformation temperature on the characteristics of isothermally hot compressed boron-alloyed steel. *Materials Science & Engineering A,* **538**, 356-63, 2012.

[42] Fan DW, Kim HS, De Cooman BC. *Steel Research International,* **80** (3), 241-348, 2009.

[43] Shi Z, Liu K, Wang M, Shi J, Dong H, Pu J, Chi B, Zhang Y, Jian L. Effect of non-isothermal deformation of austenite on phase transformation and microstructure of 22SiMn2TiB steel. *Materials Science & Engineering A,* **535**, 290-6, 2012.

[44] Johnson GR, Cook WH. Fracture characteristics of three metals subjected to various strains, strain rates, temperatures and pressures. *Engineering Fracture Mechanics,* **21** (1), 31-48, 1985.

[45] Johnson GR and Cook WH. A constitutive model and data for metals subjected to large strains, high strain rates, and high temperatures. *7th International Symposium on Ballistics*, 541-547, 1983.

[46] Voce E. The relationship between stress and strain for homogeneous deformation. *Journal of the Institute of Metals,* **74** (11), 537-62, 1948.

[47] Bardelcik A, Ghavam K, George R, Worswick MJ. An impact model of a hot stamped lab-scale b-pillar with tailored properties. *3rd International Conference on Hot Sheet Metal Forming of High-Performance Steel*, 221-228, 2011.

[48] Hollomon JH. Tensile deformation. *Transactions of the American Institute of Mining and Metallurgical Engineers,* **162**, 268-90, 1945.

[49] Naderi M, Ketabchi M, Abbasi M, Bleck W. Analysis of microstructure and mechanical properties of different high strength carbon steels after hot stamping. *Journal of Materials Processing Tech.,* **211** (6), 1117-25, 2011.

[50] Li N, Li X, Dry D, Dean TA, Lin J, Balint D. Investigation on the mechanical properties of as-formed boron steels for optimizing process strategies in hot stamping. *Steel Research International,* (Metal Forming 2012), 1259-62, 2012.

APPENDIX A: PART 1

Bardelcik A, Salisbury CP, Winkler S, Wells MA, Worswick MJ. Effect of Cooling Rate on the High Strain Rate Properties of Boron Steel. *International Journal of Impact Engineering*, **37** (6), 694-702, 2010.

International Journal of Impact Engineering 37 (2010) 694–702

Contents lists available at ScienceDirect

International Journal of Impact Engineering

journal homepage: www.elsevier.com/locate/ijimpeng

Effect of cooling rate on the high strain rate properties of boron steel

Alexander Bardelcik*, Christopher P. Salisbury, Sooky Winkler, Mary A. Wells, Michael J. Worswick

University of Waterloo, Department of Mechanical and Mechatronics Engineering, 200 University Avenue West, Waterloo, Ontario, Canada N2L 3G1

ARTICLE INFO

Article history:
Received 1 December 2008
Received in revised form 26 May 2009
Accepted 31 May 2009
Available online 6 June 2009

Keywords:
Hot forming die quenching
Ultra high strength steel
High strain rate
Split Hopkinson tensile bar
Martensite

ABSTRACT

In this work, the effect of cooling rate on the high strain rate behavior of hardened boron steel was investigated. A furnace was used to austenize boron sheet metal blanks which were then quenched in various media. The four measured cooling rates during the solid state transformation were: 25 (compressed air quench), 45 (compressed air quench), 250 (oil quench) and 2200 °C/s (water quench). Micro-hardness measurements and optical microscopy verified the expected as-quenched microstructure for the various cooling rates. Miniature dog-bone specimens were machined from the quenched blanks and tested in tension at a quasi-static rate, 0.003 s^{-1} (Instron) and a high rate, 960 s^{-1} (split Hopkinson tensile bar). The resulting stress vs. strain curves showed that the UTS increased from 1270 MPa to 1430 MPa as strain rate increased for the specimens cooled at 25 °C/s, while the UTS increased from 1615 MPa to 1635 MPa for the specimens cooled at 2200 °C/s. The high rate tests showed increased ductility for the 25, 45 and 250 °C/s specimens, while the specimens cooled at 2200 °C/s showed a slight decrease. The Hollomon hardening curve was fit to the true stress *vs.* true strain curves and showed that the mechanical response of the high rate tests exhibited a greater rate of hardening prior to fracture than the quasi-static tests. The hardening rate also increased for the specimens quenched at higher cooling rates. Optical micrographs of the fractured specimens showed that the failure mechanism transformed from a ductile-shear mode at the lower cooling rates to a shear mode at the high cooling rates.

1. Introduction

The current demand to reduce vehicle weight for improved fuel efficiency, while maintaining crash performance, has led to the application of new and innovative materials and manufacturing processes in the automotive industry. One such process is hot forming die quenching (HFDQ) of boron steel where sheet metal is austenized and subsequently stamped in a cooled die as shown in Fig. 1a. The process was developed and patented in 1974 by NJA which later merged to SSAB Hardtech and is today known as Gestamp Hardtech [1]. Although this process has been around for some 30 years, the estimated increase in European consumption of flat boron steel (60,000–80,000 t/year in 2004 is expected to increase up to 300,000 t/year in 2008–2009) indicates that automobile manufacturers are implementing more hot formed components into their vehicle design [2]. The HFDQ process is currently used to manufacture structural components such as bumper beams, door intrusion beams, A and B-pillars, roof and side rails [1–3]. These components are critical to the crash performance of a vehicle.

The HFDQ process allows for conventional stamping equipment to be used for the production of ultra high strength steel (UHSS) parts that have a final ultimate tensile strength of approximately 1500 MPa. This is achieved by heating the boron sheet metal to a temperature greater than 900 °C to achieve a homogeneous austenitic microstructure. After annealing, the sheet is transferred to a stamping press and formed with a cold tool. The initial high temperature of the sheet facilitates forming as the boron material exhibits reduced flow stress and greater ductility at high temperature. During the forming process however, the cold tool forces the cooling rate of the sheet to be greater than 30 °C/s, which results in a fully martensitic phase transformation of the sheet after it has been cooled as shown by the boron steel continuous cooling transformation (CCT) diagram in Fig. 1b [3–6].

Although components with a fully martensitic microstructure are desired because of the UHSS material properties, some structural components, such as a B-pillar, may benefit from regions that have a lower strength and greater ductility for improved crash performance as shown in Fig. 1c. These varying mechanical properties can be achieved by modifying the cooling rate within the stamping die during the HFDQ process. A cooling rate lower than 30 °C/s will result in a microstructure which contains other more ductile phases, such as bainite, ferrite or pearlite [6,7].

---

* Corresponding author. Tel.: +1 519 888 4567x36936; fax: +1 519 885 8562.
E-mail address: abardelc@uwaterloo.ca (A. Bardelcik).

0734-743X/$ – see front matter © 2009 Elsevier Ltd. All rights reserved.
doi:10.1016/j.ijimpeng.2009.05.009

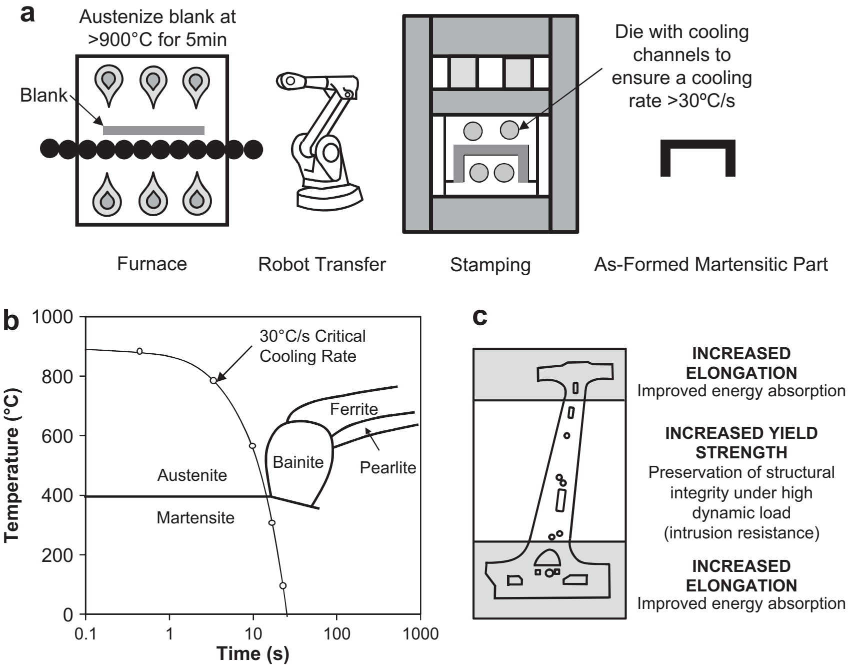

Fig. 1. (a) Schematic of the hot forming die quenching process (b) Boron steel (USIBOR® 1500P) CCT diagram showing the 30 °C/s critical cooling rate for a fully martensitic transformation (c) B-pillar with optimized microstructures for improved crash performance [6].

The HFDQ process is well understood, and thermo-mechanical finite element numerical models of the forming process have been successfully developed [3,5,8–10], but there is little published work on the as-formed, high strain rate properties of HFDQ boron steel. In a crash situation, the local strain rates in deformation zones may reach levels up to 1000 s^{-1} [11]; therefore, the high strain rate performance of the as-formed boron steel must be taken into account when modeling full-scale vehicle crash, which is the main motivation of this work.

In this study, USIBOR® 1500P boron sheet metal was austenized according to the HFDQ parameters and quenched in various media to achieve cooling rates below and above the critical rate of 30 °C/s. Miniature dog-bone specimens were then made and tested in tension at a quasi-static strain rate of 0.003 s^{-1} with an Instron and at a high strain rate of 960 s^{-1} using a split Hopkinson tensile bar apparatus. Stress vs. strain curves were then analyzed to assess the effect of cooling rate on the high strain rate performance of the boron steel. The Hollomon hardening law was fit to the data and used to compare the hardening behaviour of the different test conditions. To gain further insight into the as-quenched microstructure of the boron steel, micro-hardness measurements were made and a metallographic analysis was undertaken.

2. Experimental work

In this section the heating and quenching tests that were used to simulate the HFDQ process are discussed along with the results of the micro-hardness testing and the metallographic analysis. The low and high strain rate test experimental procedures are outlined as well.

2.1. Heating and quenching experiments

To simulate the HFDQ process, 1.63 mm USIBOR® 1500P (aluminum–silicon coated 22MnB5 steel, 0.22% carbon) boron sheet metal blanks were austenized in an electric furnace and quenched in various media to achieve different cooling rates. The as-received yield and ultimate tensile strength of the boron sheet metal were 385 MPa and 575 MPa respectively. High temperature Inconel overbraided thermocouples were resistance welded to the surface of the boron steel blanks. An Omega data acquisition system (OMB-DAQ-55) was used to monitor and record the blank temperature at 28 Hz which gives adequate temporal resolution at even the highest cooling rate. The blanks were placed into a 950 °C oven and held for 5 min after the temperature rose above 900 °C. After the 5-min hold time, the blanks were removed from the oven and quenched in three different media; a water bath (22 °C), a heated oil bath (85 °C) and compressed air at low and high flow rates. Due to the time required to transfer the specimen, the temperature dropped to approximately 870 °C prior to quenching. For the water and oil bath, the blanks were fully submerged in the media, while the compressed air apparatus was used to blow air onto both sides of the blank. The manual nature of the compressed air apparatus resulted in a less repeatable cooling rate for the blanks, which further became apparent during the low and high strain rate mechanical testing. The cooling rate was quantified using an ideal (and linear) cooling rate curve that was constructed from the measured start temperature to the beginning of the apparent phase transformation temperature (approximately 400 °C for all rates) which appears as a decrease in cooling rate due to the heat released during the transformation. Although this change in cooling rate is a good approximation of a phase transformation, dilation tests provide a more accurate measure of the phase transformation temperature/time. Using this method of determining the cooling rate, the following rates were measured for the 4 different quench media; 25, 45, 250 and 2200 °C/s.

Fig. 2 shows the USIBOR® 1500P continuous cooling transformation (CCT) diagram with the measured cooling curves. As indicated by the CCT diagram, the blanks quenched at 45, 250 and 2200 °C/s should have a fully martensitic microstructure (indicated by an "M"), while the blank quenched at 25 °C/s is expected to have bainite within its microstructure since the cooling curve intersected the nose of the CCT where bainite forms (indicated by a “B” in the figure).

2.2. Micro-hardness testing

Micro-hardness testing of the quenched specimens was conducted to quantify the effect of cooling rate/microstructure on the Vickers hardness. The micro-hardness was measured using a LECO MHT Series 2000 testing system. The hardness measurements were taken in the gauge length region of the miniature dog-bone specimens that were made from the quenched blank as shown in Fig. 3 inset. The hardness values are similar through the thickness of the quenched specimens as shown in Fig. 3. The average through the thickness Vickers and Rockwell C [HRC] hardness values of the quenched specimens are shown in Table 1.

Hodge and Orehoski [12] conducted Jominy bar end-quench tests on a variety of carbon steels and showed (using microstructural examination) that for a 0.22% carbon steel, the microstructure consisted of 99% martensite when the measured hardness was greater than 45.4 HRC (independently shown for high purity iron–carbon alloys by Litwinchuk et al. [13]). As they examined the microstructure further away from the quenched end of the Jominy bar (where cooling rates were lower and more bainite was present), they showed that the percent martensite formed and hardness decreased. Table 1 shows the predicted percent martensite formed (using Ref. [12]) based on the average micro-hardness measurements made for this work. Because the 25 °C/s cooling curve intersected the bainite formation region of the boron steel CCT diagram (Fig. 2), the predicted percent martensite formed is 95% while, while the remainder is expected to be bainite. The hardness of the other three cooling rate specimens predict a fully martensitic (99%) as-quenched microstructure which is expected because of the position of the cooling curves on the CCT diagram. Although the microstructure of the specimens quenched at 45, 250, 2200 °C/s is fully martensitic, the hardness increases for higher cooling rates and may be due to a change in the martensitic structure as will be shown in the next section.

2.3. Metallography

After quenching and mechanical testing, the specimens were studied using metallographic techniques. The specimens were mounted in epoxy resin, ground and polished to a mirror finish using 500, 1200 and 4000 grit SiC paper; followed by 3, 1 and 0.25 μm diamond paste. A 2% Nital etching solution was used to reveal the microstructure. Microstructural and failure characterization was carried out using an Olympus BH60 optical microscope equipped with an ImagePro Plus 5.1 image analysis software.

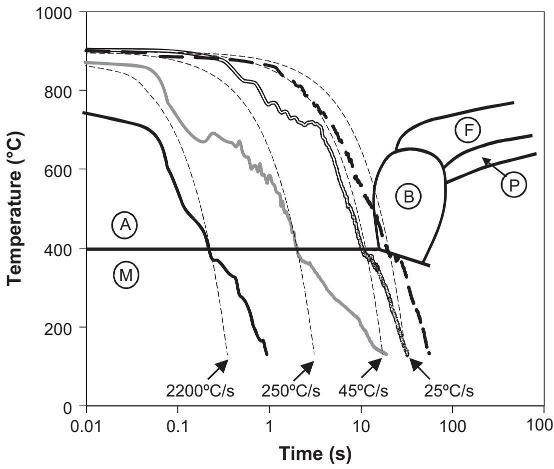

Fig. 2. Cooling curve profiles for the various cooling rates plotted with the USIBOR® 1500P CCT diagram.

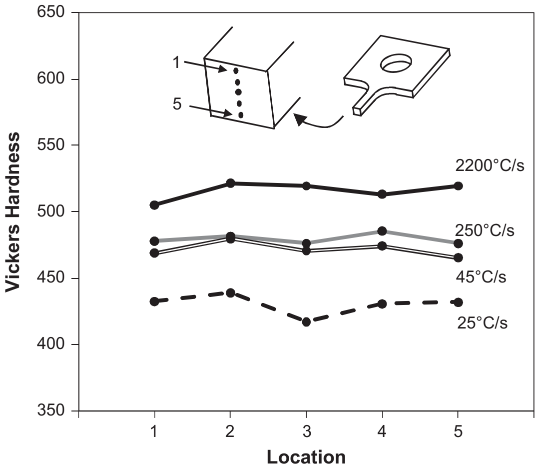

Fig. 3. Micro-hardness measurements of the quenched specimens.

As indicated by the CCT diagram in Fig. 2 and predicted by Ref. [12] (Table 1), the blanks quenched at 45, 250 and 2200 °C/s should have a fully martensitic microstructure; while the blanks quenched at 25 °C/s are expected to have a predominantly martensitic microstructure with small amounts of bainite since the cooling curve intersected the nose of the CCT where bainite forms. Because the weight percent carbon of the boron steel is less than 0.60%, the as-quenched martensite consists of a lath structure [14,15]. Initial metallographic examination of the as-quench blanks confirms the martensitic microstructure for the 25, 45 and 250 °C/s specimens as shown in Fig. 4a and b. The magnified sections of the micrographs highlight the previous austenite grain boundaries and the packets of parallel lath crystals that are characteristics of the martensite [14–17]. The microstructure of the specimen cooled at 2200 °C/s appears to contain a finer and more randomly oriented structure. The previous austenite grain boundaries are difficult to distinguish and the observed packet size is more fine and randomly dispersed throughout the microstructure, which would lead one to expect that the martensite will have an elevated strength (hardness has already been shown to be elevated) do to an increase in dislocation impedances [15,16,18].

2.4. Low to high strain rate mechanical testing

The quenched blanks were CNC machined into the miniature dog-bone style specimens shown in Fig. 5a. The specimen gauge

Table 1
Measured cooling rates, Vickers hardness and percent martensite of the quench blanks.

Quench media	Measured cooling, rate (°C/s)	Average Vickers hardness [HRC]	Percent martensite of a 0.22% carbon steel[a]
Low flow compressed air	25	420 [43.6]	95%
High flow compressed air	45	472 [47.1]	99%
Oil bath	250	480 [47.7]	99%
Water bath	2200	516 [50.2]	99%

[a] Predicted as a function of hardness [12].

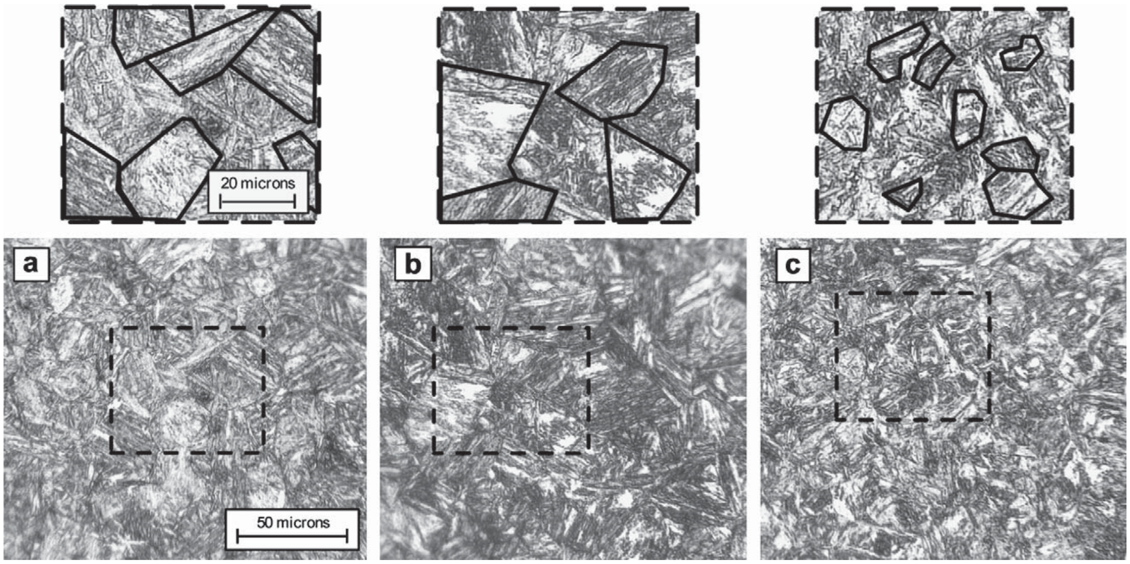

Fig. 4. Optical micrographs of quenched specimens (a) 25 °C/s (b) 45 °C/s and (c) 2200 °C/s. Etchant: 2% Nital. The microstructure of the 250 °C/s specimens are very similar to the 45 °C/s specimens.

length was 12.5 mm and the same specimen was used for both the low and high strain rate tests. Work conducted at the University of Waterloo has shown that the miniature dog-bone style geometry used for this work correlated well with standard ASTM (E 8M-04) dog-bone specimen results up to the ultimate tensile strength for both aluminium [19,20] and advanced high strength steels [21–23]. Fig. 5 shows the Instron apparatus that was used for the quasi-static strain rate tests and the split Hopkinson tensile bar apparatus that was used for the high rate tests. For each of the four cooling rates, three repeatable test results were used for the analysis at the two strain rates.

Quasi-static strain rate. The quasi-static experiments were conducted using a servo hydraulic Instron testing apparatus (Fig. 5b). Custom grips were made for the miniature dog-bone specimens and an extensometer was used to measure the elongation of the specimen gauge length. A cross-head displacement of 2.25 mm/min was used, which resulted in a strain rate of 0.003 s^{-1}.

High strain rate. High strain rate testing was conducted using the split Hopkinson tensile bar (SHTB) apparatus at the University of Waterloo (Fig. 5c). The apparatus is described briefly here, while a more detailed description can be found in Refs. [19,21].

The SHTB uses a gas gun to propel a concentric hollow striker towards an end cap located at the free end of the incident pressure bar. Upon impact, a tensile incident loading pulse is generated which travels towards the specimen. As the incident wave reaches the specimen a portion is transmitted into the sample with the remainder being reflected. The specimen is overwhelmed by the applied impulse which causes the specimen to deform at high rates. Strain gauges placed on the incident and transmitted bars measure the incident, reflected and transmitted waves. The waves are then analyzed using the Hopkinson bar equations to determine the stress vs. strain relationship of the sample. The strain rates for these tests were relatively constant during plastic deformation and the average measured values for all of the specimens tested were 960 s^{-1}.

3. Results and discussion

The results of the two strain rate tests performed at 0.003 s^{-1} and 960 s^{-1} for each cooling rate are presented. The Holloman hardening law is fit to the experimental data and the flow stress curves are presented to show the plastic behavior of the quenched specimens up to the UTS.

3.1. Constitutive behaviour

Fig. 6a and b shows the complete set of engineering stress vs. strain results for the quasi-static and high strain rate tests respectively. As can be seen in the figures, the results of the 45, 250 and 2200 °C/s tests were very repeatable at both strain rates, while the tests performed on the 25 °C/s specimens exhibited more scatter.

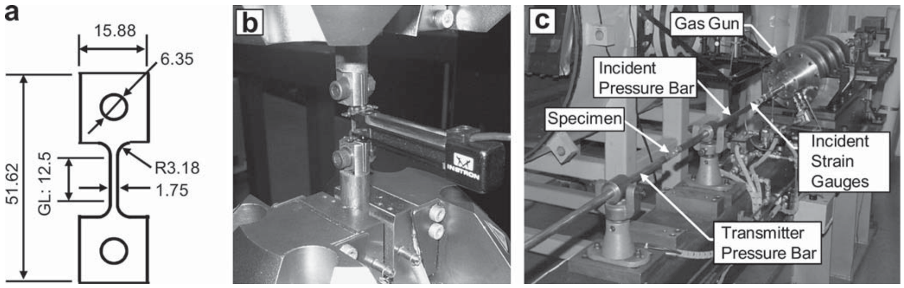

Fig. 5. (a) Miniature dog-bone specimen geometry (dimensions are in mm) (b) Quasi-Static testing apparatus and (c) Split Hopkinson tensile bar apparatus.

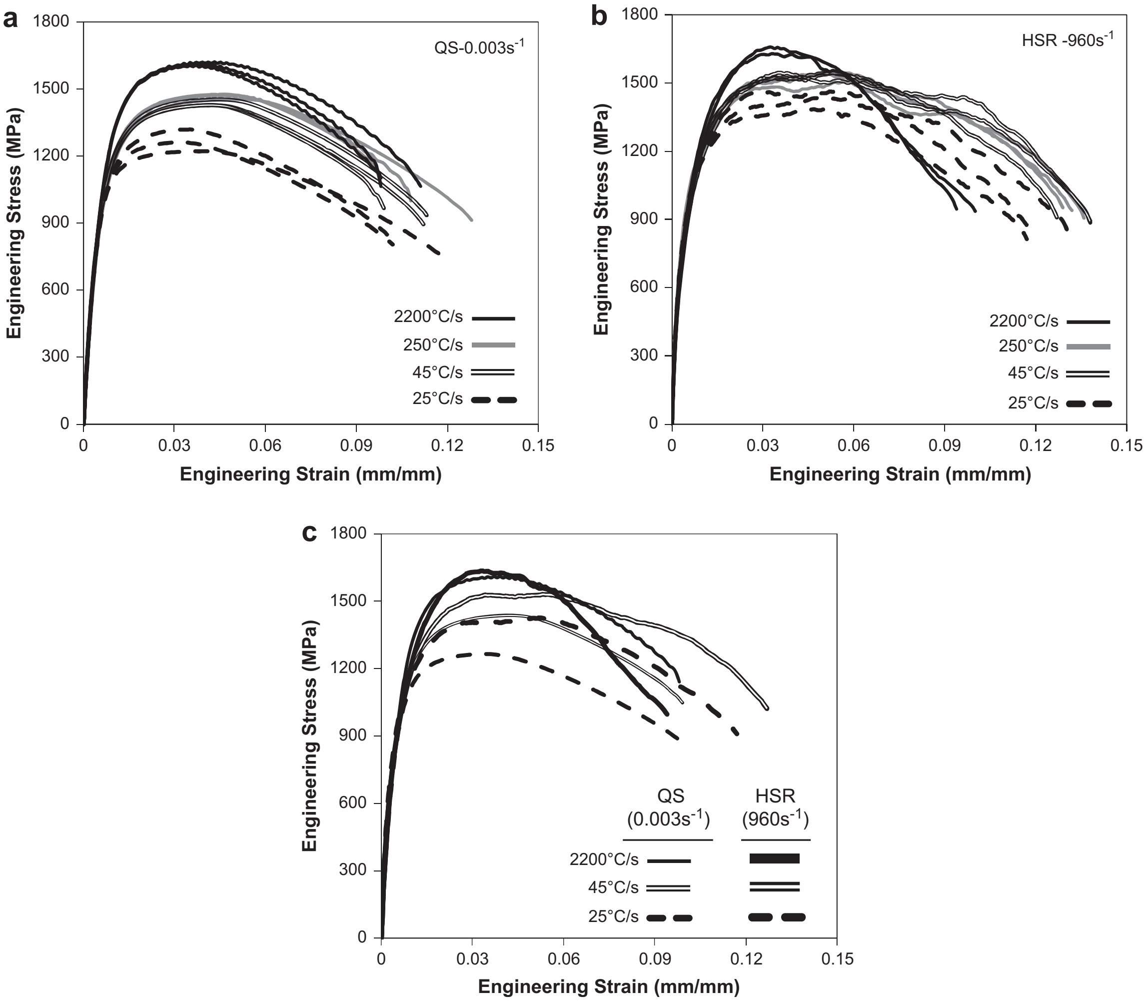

Fig. 6. (a) Quasi-static strain rate (0.003 s^{-1}) engineering results (b) High strain rate (960 s^{-1}) engineering results and (c) Average quasi-static and high strain rate engineering results. The 250 °C/s results were omitted from (c) for clarity.

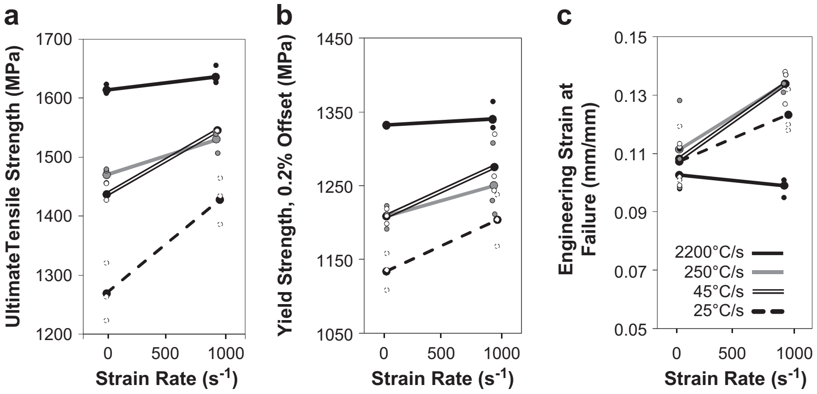

Fig. 7. Effect of strain rate on (a) ultimate tensile strength, (b) yield strength (0.2% offset method) and (c) engineering strain at failure. The small data points represent the individual repeat test results.

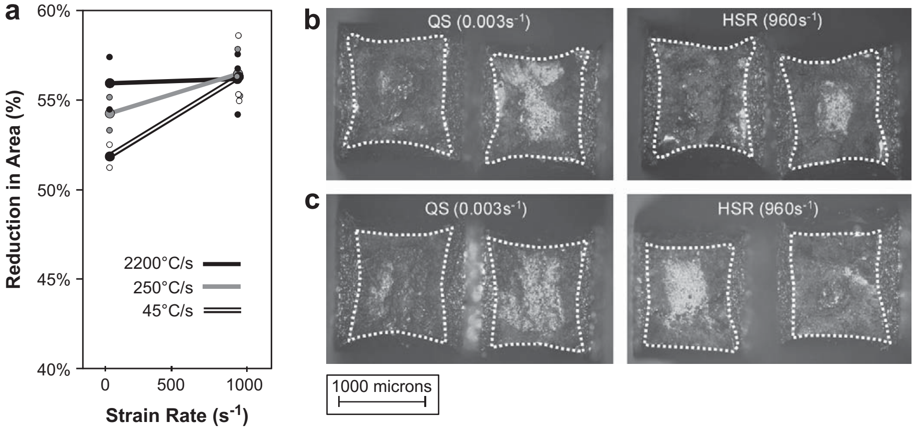

Fig. 8. (a) Effect of strain rate on the reduction of cross-sectional area at failure. Typical fracture surface of (b) 45 °C/s and (c) 2200 °C/s quenched specimens.

Due to the manual nature of the compressed air quenching apparatus, the measured cooling rate varied between 23 and 26 °C/s along the blank from which the specimens were cut. Due to this slight variation in cooling rate, the percent volume of bainite/martensite formed would have also varied, resulting in less repeatability of the mechanical properties due to a variation in the microstructure. This also indicates the sensitivity of the material's mechanical response to small fluctuations in cooling rate. For each test condition, the data of the three repeated tests were averaged and a representative curve was constructed for each condition as shown in Fig. 6c. The results of the 250 and 45 °C/s cooling rates were very similar, therefore the 250 °C/s data was omitted in Fig. 6c for clarity. The engineering parameters used to compare the effect of cooling rate and strain rate on the mechanical response are; the ultimate tensile strength (UTS), the yield strength (YS) and the strain at failure. These three results (average and individual test results) are summarized in Fig. 7.

For all of the conditions tested, the UTS occurred between 0.03 and 0.06 strain. Fig. 7a shows that the UTS of the cooling rates within the hot forming die quenching (HFDQ) process window (45 and 250 °C/s) are on average 1450 MPa at the quasi-static (QS) strain rate and increases by 6% to approximately 1540 MPa at the high strain rate (HSR). At the highest cooling rate, which is beyond the HFDQ process window, the UTS marginally increased from 1620 MPa at QS to 1640 MPa at HSR. The 25 °C/s cooling rate specimens resulted in a UTS of 1270 MPa at QS and 1430 MPa for the HSR test. This cooling rate showed the greatest increase in UTS (13%) as a function of strain rate.

The yield strength (YS) of the test specimens was calculated using the 0.2% offset method. For each test, an apparent elastic modulus was fit to the initial linear rise portion up to 900 MPa and then used in the 0.2% offset method. Fig. 7b shows the results of the measured YS as a function of strain rate. As expected, the YS trends are similar to the UTS trends (Fig. 7a) for the different cooling rates. The 2200 °C/s cooling rate specimens showed almost no increase in YS (~ 1340 MPa) for the two rates tested, while the 25 °C/s cooling rate specimens showed the greatest increase in YS from 1130 MPa at QS up to 1200 MPa at the HSR.

There is a large amount of scatter in the engineering strain at failure (Fig. 7c) at the QS rate for all of the cooling rates. On average, the QS strain at failure was approximately 0.11 for the 25, 45 and 250 °C/s cooling rates, while for the HSR tests, there was less scatter and an average increase in strain at failure to approximately 0.13. Similar increases in strain at failure have been shown for advanced

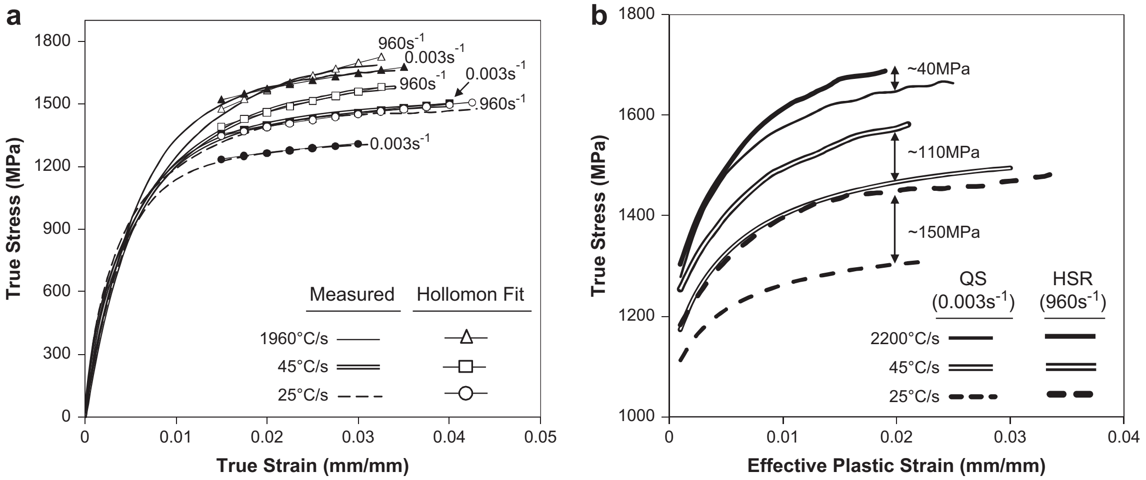

Fig. 9. (a) The average true stress vs. strain and (b) flow stress results. The 250 °C/s results were omitted for clarity.

Table 2
Results of the Hollomon hardening function curve fit.

Cooling rate (°C/s)	Strain rate (s^{-1})	Strength coefficient, K (MPa)	Strain-hardening coefficient, n	R^2
25	0.003	1758	0.084	0.982
	960	2119	0.108	0.940
45	0.003	2118	0.106	0.969
	960	2755	0.162	0.963
250	0.003	2183	0.110	0.965
	960	2538	0.143	0.924
2200	0.003	2473	0.116	0.959
	960	3441	0.202	0.974

high strength steels [23,24] and aluminum [20,25]. For the 2200 °C/s cooling rate specimens, the strain at failure decreased slightly when the strain rate was increased from QS to HSR.

In addition to the strain at failure, the reduction in cross-sectional area at failure, which is a measure of ductility, was measured and is presented vs. strain rate in Fig. 8a. An Olympus BH60 optical microscope equipped with ImagePro Plus 5.1 image analysis software was used to measure the cross-section of the failed specimens. After image enhancement, the cross-sectional area was measured by tracing a polygon around the edge of the fracture surface as shown in Fig. 8b and c. Due to the large shear lips formed at the fracture surface of the specimens quenched at 25 °C/s, it was difficult to accurately measure the cross-section and therefore the

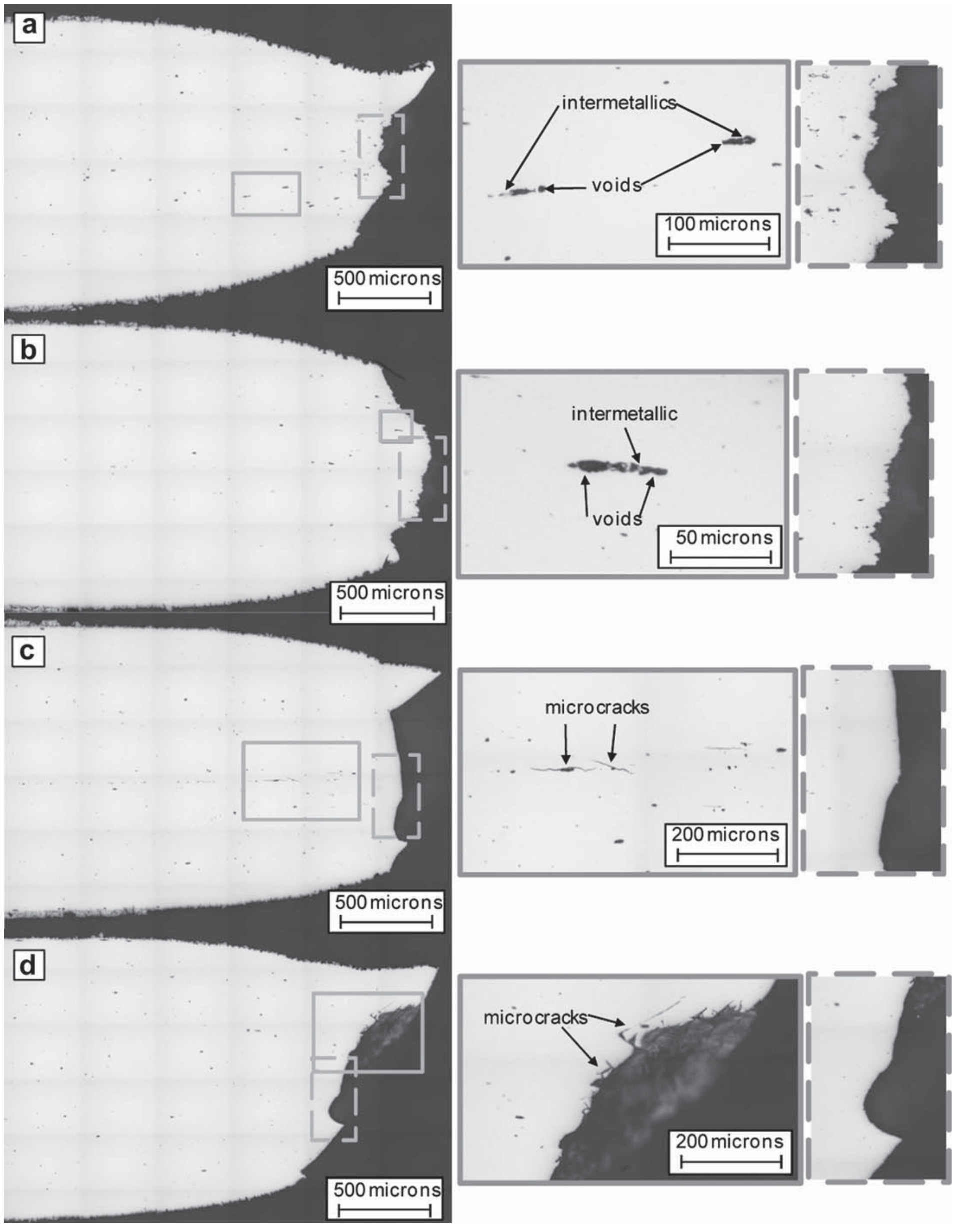

Fig. 10. Optical micrographs showing the cross-section and fracture profiles of specimens tested at 0.003 s^{-1} for (a) 25 °C/s (b) 45 °C/s (c) 250 °C/s and (d) 2200 °C/s. The images on the right are higher-resolution images of regions highlighted on the left. As-polished and viewed along the long-transverse plane.

results were omitted. The Fig. 8a trends suggest that by increasing the strain rate, the specimens quenched at 45 and 250 °C/s show improved ductility while the 2200 °C/s specimens were unaffected at the higher strain rate. These results agree with the strain at failure trends shown in Fig. 7c.

The engineering stress vs. strain data was converted into true stress vs. strain and used to rank the relative formability of the quenched specimens (Fig. 9a). For clarity, the 250 °C/s results were omitted. In order to quantify the effect of cooling and deformation rate on the hardening behaviour, the Hollomon [26] equation was fit to the true stress vs. strain data,

$$\sigma = K\epsilon^n \tag{1}$$

where K is the strength coefficient (MPa) and n is the strain-hardening exponent. Each individual test result was fit with (1) from 0.015 strain up to the UTS. This portion of the curves was selected because it has been shown that notable changes occur in the n-value at low strains for most metals and in particular for martensitic steels [27,28]. The K and n parameters were then averaged for each condition and are shown in Table 2. As an indication to the goodness of the fitted parameters, the R-squared value is identified in the table. The results of the curve fitting exercise are plotted as the curves with data points in Fig. 9a. For most metals, the n-value provides an empirical parameter for appraising the relative stretch formability of similar metallic systems and is useful for estimating the strain at the onset of necking in a uniaxial tension test [29,30].

The strain-hardening coefficient results in Table 2 indicate that the onset of necking ranges from 0.08 to 0.20 strain for all of the conditions tested. This does not agree with the measured results (see Fig. 6) which show that the onset of necking occurs between 0.03 and 0.06 strain. Although the predicted n-values are high, they serve to rank the relative formability of the specimens tested in this work. For all of the individual cooling rates, the HSR n-values are greater than the QS n-values, indicating that a higher rate of deformation causes the rate of hardening to increase. This agrees with the increased strain at failure (except for 2200 °C/s) at HSR as shown in Fig. 7c. The K-values of the HSR tests are also greater than the QS tests for each cooling rate, which show the increased strength of the material at higher rates of loading.

All of the repeat tests conducted for this work were converted from engineering to true stress vs. effective plastic strain (or flow stress curves) up to the point of necking. The apparent modulus that was found for each test was used to calculate an elastic strain which was subtracted from the total strain resulting in effective plastic strain. For each condition, an average curve of the repeated tests was found and is shown in Fig. 9b (the 250 °C/s results were omitted for clarity). In general, the flow stress increases at the higher strain rate for all of the cooling rates tested. Also, the difference in flow stress between the QS and HSR tests decreases as the cooling rate is increased. This is shown in Fig. 9b by the flow difference for the three cooling rates, where the difference is approximately 40 MPa for the 2200 °C/s specimens while the difference is approximately 150 MPa for the specimens cooled at 25 °C/s (at 0.02 strain). This trend may be related to the increased hardness (and change in microstructure) that the specimens exhibited for higher cooling rates.

3.2. Deformation behaviour

The optical micrographs in Fig. 10 show the typical cross-section and fracture profile of the as-quenched blanks that failed at a strain rate of 0.003 s^{-1}. As the cooling rate of the specimens increases from 25 to 2200 °C/s, the fracture surface changes from that of a rough fibrous ductile appearance (Fig. 10a and b) to a smoother planar shear appearance (Fig. 10c and d). This suggests that the failure mechanism transitions from a ductile-shear mode to a shear mode with increasing cooling rates. Less localized necking is also observed in specimens quenched at the higher rates. This trend is expected considering the increased hardness of the specimens quenched at the higher rates (Fig. 3). Damage in the specimens studied is also found to be sensitive to the cooling rate. In specimens quenched at 25 and 45 °C/s, damage is observed to occur via a void nucleation and growth mechanism at the grey hard non-deformable intermetallics seen in Fig. 10a and b, prior to final failure via shear overload. For specimens quenched at 250 and 2200 °C/s, the presence of micro-cracks are seen along the centre-line of the specimen (Fig. 10c) or adjacent to the fracture surface at approximately 45 degrees angle to the applied load.

4. Conclusions and recommendations

Utilizing a furnace and various quenching media, four different cooling rates were successfully imposed on initially austenized boron steel blanks. The boron steel CCT diagram showed that the 45, 250 and 2200 °C/s quenched blanks resulted in a fully martensitic phase transformation, while the 25 °C/s cooling rate specimens allowed approximately 95% martensite to form with the remainder being bainite. This was confirmed by the measured cooling rates and the micro-hardness tests.

The repeatability of the quasi-static 0.003 s^{-1} (QS) and high strain rate 960 s^{-1} (HSR) tests was good for the 45, 250 and 2200 °C/s specimens. The 25 °C/s specimens showed more scatter because the cooling rate varied slightly along the blank. It is likely that the variation in cooling rate resulted in a variation of bainite formed. Future work will examine lower cooling rates that produce other phases such as pearlite and ferrite.

The 45 and 250 °C/s cooling rates are representative of the thermal route that boron sheet undergoes during the hot forming die quenching (HFDQ) process. Even though the cooling rates vary considerable, the mechanical properties of the quenched specimens are almost identical, which is an attribute of this robust process. By increasing the strain rate from QS to HSR, the average ultimate tensile strength and average yield stress increase by 6% and 4% respectively. The increased strain rate also showed an average increase in strain at failure from 0.11 to 0.13.

A structural vehicle member, such as a B-pillar, would benefit from regions that have increased elongation properties for improved crash performance. One such method is to lower the cooling rate during forming, which introduces other phases such as bainite, pearlite and ferrite. By introducing some bainite into the mostly martensitic microstructure, the ultimate tensile strength (UTS) of the 25 °C/s quenched specimen was reduced (compared to the 45 and 250 °C/s) by an average of 190 MPa at QS and 110 MPa at HSR. Similarly, the YS also reduced by 75 MPa and 60 MPa for QS and HSR respectively. The strain at failure was similar to the 45 and 250 °C/s quenched specimens and did not offer an increase in elongation that would have been beneficial for improved energy absorption.

The highest cooling rate (2200 °C/s) is outside the realistic capability of the HFDQ process, and illustrates a bounding extreme of the boron steel properties. An increase in strain rate from QS to HSR resulted in a marginal increase in UTS from 1620 MPa to 1640 MPa and almost no increase in YS. In comparison to all of the cooling rates tested, the 2200 °C/s specimens showed a slight decrease in strain at failure and the lowest increase in flow stress when tested at the high rate.

It has been shown that the strain-hardening exponent (n), which was derived from the Hollomon equation, does not predict the strain at the onset of necking as it does for other metals. It does however show that loading the specimens at 960 s^{-1} results in a higher rate of strain-hardening prior to fracture than the specimens loaded at the 0.003 s^{-1} rate, as indicated by the higher *n*-values.

Optical micrographs showed that the highest cooling rate produces a more refined martensitic grain structure. Also, as the cooling rate was increased, the observed failure mechanism transformed from a ductile-shear mode to a shear mode.

Acknowledgements

The authors would like to thank the Natural Sciences and Engineering Research Council of Canada (NSERC) and the Ontario Research Fund Research Excellence (ORF-RE) program for their support of this work.

References

[1] Jonsson M. Press hardening, from innovation to global technology. In: Proceedings of the first international conference on hot sheet metal forming of high-performance steel; Kassel, Germany: Steel grips. October 2008. p. 253–65.
[2] Altan T. Hot-stamping boron-alloyed steels for automotive parts, Part I: Process methods and used. Stamping Journal 2006;(December)::40–1.
[3] Hein P. A global approach of the finite element simulation of hot stamping. Advanced Materials Research 2005;6–8:763–70.
[4] Akerstrom P, Wikman B, Oldenburg M. Material parameter estimation for boron steel from simultaneous cooling and compression experiments. Modelling and Simulation in Materials Science and Engineering 2005;13(8):1291–308.
[5] Merklein M, Lechler J. Investigation of the thermo-mechanical properties of hot stamping steels. Journal of Materials Processing Technology 2006;177(1–3):452–5.
[6] Maikranz-Valentin M, Weidig U, Schoof U, Becker HH, Steinhoff K. Components with optimised properties due to advanced thermo-mechanical process strategies in hot sheet metal forming. Steel Research International 2008;79(2):92–7.
[7] Hein P, Wilsius J. Status and innovation trends in hot stamping of USIBOR 1500P. Steel Research International 2008;79(2):85–91.
[8] Akerstrom P, Oldenburg M. Austenite decomposition during press hardening of a boron steel – computer simulation and test. Journal of Materials Processing Technology 2006;174(1–3):399–406.
[9] Bergman G, Oldenburg M. A finite element model for thermomechanical analysis of sheet metal forming. International Journal for Numerical Methods in Engineering 2004;59(9):1167–86.
[10] Naderi M, Durrenberger L, Molinari A, Bleck W. Constitutive relationships for 22MnB5 boron steel deformed isothermally at high temperatures. Materials Science and Engineering A, Structural Materials: Properties, Microstructure and Processing 2008;478(1–2):130–9.
[11] Salisbury CP, Worswick MJ, Mayer R. High rate constitutive modeling of aluminium alloy tube. Journal de Physique IV 2006;134(Eurodymat 2006; Suppl.):43–8.
[12] Hodge JM, Orehoski MA. Relationship between hardenability and percentage of martensite in some low-alloy steels. Transactions of the American Institute of Mining and Metallurgical Engineers 1946;167:627–42.
[13] Litwinchuk A, Kayser FX, Baker HH, Henkin A. Rockwell-C hardness of quenched high-purity iron–carbon alloys containing 0.09 to 1.91 percent carbon. Journal of Materials Science 1976;11(7):1200–6.
[14] Marder AR, Krauss G. Morphology of martensite in iron–carbon alloys. Asm Transactions Quarterly 1967;60(4):651–60.
[15] Krauss G. Principles of heat treatment of steel. Metals Park, Ohio: American Society for Metals; 1980. p.43-83.
[16] Naylor JP. Influence of the lath morphology on the yield stress and transition-temperature of martensitic–bainitic steels. Metallurgical Transactions A, Physical Metallurgy and Materials Science 1979;10(7):861–73.
[17] Schulz-Beenken A. Martensite in steels: its significance, recent developments and trends. Journal de Physique IV 1997;07. C5-359–C5-366.
[18] Wang C, Wang M, Shi J, Hui W, Dong H. Effect of microstructure refinement on the strength and toughness of low alloy martensitic steel. Journal of Materials Science and Technology 2007;23(5):659–64.
[19] R. Smerd. Constitutive behavior of aluminum alloy sheet at high strain rates. Master of Applied Science Thesis, University of Waterloo; 2005.
[20] Smerd R, Winkler S, Salisbury C, Worswick M, Lloyd D, Finn M. High strain rate tensile testing of automotive aluminum alloy sheet. International Journal of Impact Engineering 2005;32(1–4):541–60.
[21] A.C. Thompson. High strain rate characterization of advanced high strength steels. Master of Applied Science Thesis, University of Waterloo; 2006.
[22] Thompson AC, Salisbury CP, Worswick MJ, Mayer R. Constitutive modelling of dual phase steel sheet and tube. Journal de Physique IV 2006;134(Eurodymat 2006; Suppl.):281–6.
[23] Winkler S, Thompson A, Salisbury C, Worswick M, Van Riemsdijk I, Mayer R. Strain rate and temperature effects on the formability and damage of advanced high-strength steels. Metallurgical and Materials Transactions A – Physical Metallurgy and Materials Science 2008;39A(6):1350–8.
[24] Huh H, Lim J, Park S. High speed tensile test of steel sheets for the stress–strain curve at the intermediate strain rate. International Journal of Automotive Technology 2009;10(2):195–204.
[25] Higashi K, Mukai T, Kaizu K, Tsuchida S, Tanimura S. Strain rate dependence on mechanical-properties in some commercial aluminum-alloys. Journal de Physique III 1991;1(C3):341–6.
[26] Hollomon JH. Tensile deformation. Transactions of the American Institute of Mining and Metallurgical Engineers 1945;162:268–90.
[27] Samuel KG. Limitations of Hollomon and Ludwigson stress–strain relations in assessing the strain hardening parameters. Journal of Physics D Applied Physics 2006;39(1):203–12.
[28] Umemoto M, Liu ZG, Sugimoto S, Tsuchiya K. Tensile stress–strain analysis of single-structure steels. Metallurgical and Materials Transactions A – Physical Metallurgy and Materials Science 2000;31(7):1785–94.
[29] E646: standard test method for tensile strain-hardening exponents (*n*-values) of metallic sheet materials. West Conshohocken, PA: ASTM; 2000. p. 607–13.
[30] Kleemola HJ, Nieminen MA. Strain-hardening parameters of metals. Metallurgical Transactions 1974;5(8):1863–6.

Alexander Bardelcik, MASc: PhD Student, Department of Mechanical and Mechatronics Engineering, University of Waterloo

Christopher P. Salisbury, MASc, P.Eng: Senior Research Engineer, Department of Mechanical and Mechatronics Engineering, University of Waterloo

Sooky Winkler, PhD: Research Assistant Professor, Department of Mechanical and Mechatronics Engineering, University of Waterloo

Mary A. Wells, PhD, P.Eng: Associate Proffesor and Associate Dean, Outreach, Department of Mechanical and Mechatronics Engineering, University of Waterloo

Michael J. Worswick, MASc, PhD, P.Eng: Professor and Tier 1 Canada Research Chair, Department of Mechanical and Mechatronics Engineering, University of Waterloo.

APPENDIX B: PART 2

Bardelcik A, Worswick MJ, Winkler S, Wells MA. A Strain Rate Sensitive Constitutive Model for Quenched Boron Steel with Tailored Properties. *International Journal of Impact Engineering*, **50**, 49-62, 2012.

International Journal of Impact Engineering 50 (2012) 49–62

Contents lists available at SciVerse ScienceDirect

International Journal of Impact Engineering

journal homepage: www.elsevier.com/locate/ijimpeng

A strain rate sensitive constitutive model for quenched boron steel with tailored properties

A. Bardelcik*, M.J. Worswick, S. Winkler [1], M.A. Wells

University of Waterloo, Department of Mechanical and Mechatronics Engineering, 200 University Avenue West, N2L 3G1 Waterloo, Ontario, Canada

ARTICLE INFO

Article history:
Received 9 December 2011
Received in revised form
8 June 2012
Accepted 25 June 2012
Available online 7 July 2012

Keywords:
Hot stamping
Martensite
Bainite
Constitutive model
Split Hopkinson tensile bar

ABSTRACT

In this work, boron steel sheet metal blanks were austenized and quenched at five different cooling rates ranging from 14 °C/s to 50 °C/s, which resulted in as-quenched microstructures that ranged from bainitic to martensitic respectively. Micro-hardness tests revealed a linear relationship between the Vickers hardness and percent area fraction of martensite and bainite present in the quenched specimens. Miniature tensile specimens were machined from the quenched blanks and tested in tension at four strain rates from 0.003 s^{-1} to 1075 s^{-1}. For the 0.003 s^{-1} tests, the ultimate tensile strength (UTS) increased from 816 MPa to 1447 MPa for the 14 °C/s and 50 °C/s quench condition respectively. By elevating the strain rate from 0.003 s^{-1} to 1075 s^{-1}, the UTS of the 14 °C/s specimens increased by 134 MPa, while the increase in UTS of the 50 °C/s specimens was measured to be 170 MPa for an equivalent change in loading rate. The percent area reduction of the fracture surface was 70% for the 14 °C/s specimens and decreased to 58% for the 50 °C/s specimens. The true stress versus effective plastic strain (flow stress) curves were used to develop the "Tailored Crash Model" (TCM) which is a constitutive model that is a function of strain, strain rate, and as-quenched Vickers hardness (or area fraction martensite/bainite). Scanning electron microscope and optical microscope images of the fracture surfaces revealed a transition from ductile to shear fracture behaviour as the quench condition increased from 14 °C/s to 50 °C/s.

1. Introduction

The demand for lighter vehicles that possess excellent crashworthiness properties has driven the automotive industry to develop new and innovative materials and manufacturing processes. The hot stamping process, which is also known as press hardening, is one such recent innovation that is gaining popularity for the manufacture of vehicle structural components as indicated by a steady increase in global [1,2] production rates. Hot stamping allows conventionally stamped parts to attain Ultra High Strength Steel (UHSS) properties with tensile strengths up to 1500 MPa. The UHSS properties are a result of in-die quenching, which causes a hot blank to undergo a solid-state phase transformation from austenite to 100% martensite during the forming process. The elevated strength of hot stamped parts allows for the use of thinner gauge sheet metal, which has the potential to reduce part weight while maintaining crash and structural integrity. The hot stamping process is currently used to manufacture structural components such as bumper beams, door intrusion beams, A- and B-pillars, roof and side rails [1,3–7]. Karbasian and Tekkaya [7] provide a detailed review of the hot stamping process.

Although components with a fully martensitic microstructure are often desired due to their exceptional high strength and intrusion resistance, some structural components, such as a B-pillar, may benefit from regions of reduced strength and greater ductility for improved energy absorption and fracture resistance as shown in Fig. 1 [8–12]. This class of hot stamped parts are said to have "tailored properties" and various hot stamping processes exist which are capable of creating such a part [7,13]. George et al. [14,15] used the "in-die heating" hot stamping process to produce regions of tailored properties within a lab-scale B-pillar. This process utilized a segmented hot stamping die with one segment that remained at room temperature while the other segment was heated to 400 °C. The as-quenched Vickers hardness of the B-pillar region hot stamped within the heated die segment varied from 244 HV to 260 HV, while the average as-quenched Vickers hardness of the section hot stamped within the room temperature die segment was 475 HV. The lower hardness of the tailored region was

---

* Corresponding author. Tel.: +1 519 888 4567x36936; fax: +1 519 885 8562.
E-mail address: abardelc@uwaterloo.ca (A. Bardelcik).

[1] Present address – Dana Power Technologies, 656 Kerr Street, L6K 3E4 Oakville, Ontario, Canada.

0734-743X/$ – see front matter © 2012 Elsevier Ltd. All rights reserved.
http://dx.doi.org/10.1016/j.ijimpeng.2012.06.007

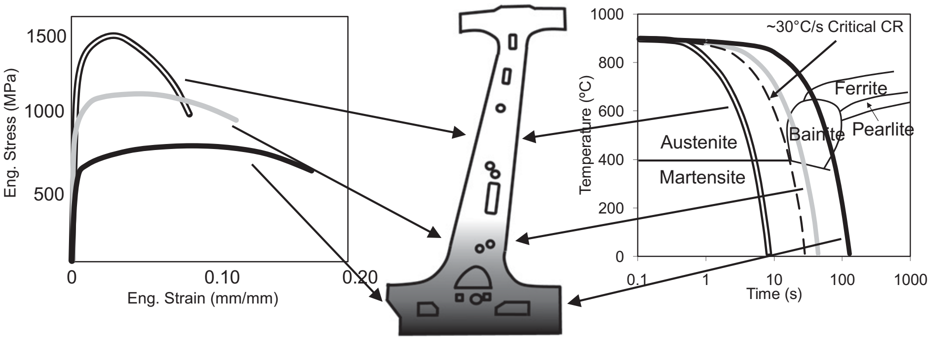

Fig. 1. Schematic of a B-pillar with tailored properties shown with a USIBOR® 1500P CCT diagram.

due to sub-critical cooling rates (less than ~30 °C/s) imposed on the blank during hot stamping, which allowed some volume fraction of bainite (and/or ferrite) to form as shown in the continuous cooling transformation (CCT) diagram in Fig. 1. Various other researchers have conducted similar hot stamping experiments with heated tools and have shown that the hardness decreases with increasing tool temperature [16–18].

One requirement to support introduction of tailored parts in cars is the development of predictive models of in-service crash response. This mandates development of strain rate sensitive constitutive models which account for the broad range of strain rates that are encountered during crash (up to 1000 s^{-1}) [19–22], as well as the effect of quench rate on the material properties within the part [16–18,23,24]. Typically, strain rate sensitive constitutive models are developed for a single material, but in the case of a part with tailored properties, the constitutive model must also be a function of the as-formed phases that develop within the as-quenched microstructure. This is the main focus of the current work, which strives to; (i) characterize the low to high strain rate behaviour and mechanical properties of an as-quenched boron steel with tailored properties; (ii) develop a strain rate sensitive constitutive model (for tailored parts) to be used in crash simulations and (iii) characterize the fracture behaviour of hot stamped steels with tailored properties.

2. Experimental methods

In this section, the heating and cooling procedure used to quench boron steel blanks are discussed, the experiments and procedure used to quantify the as-quenched volume fraction of phases found in the quenched blanks is outlined and the details of the micro-hardness and tension tests are presented.

2.1. USIBOR® 1500P boron steel

For this work, 1.2 mm USIBOR® 1500P sheet metal was used. The sheet metal has an Al–Si coating and an as-received microstructure of ferrite/pearlite with a yield strength, ultimate tensile strength and uniform elongation of 485 MPa, 612 MPa and 0.22, respectively. The chemical composition of the steel is given in Table 1.

2.2. Forced air quenching apparatus (FAQA)

A forced-air quenching apparatus (FAQA) was used to quench the USIBOR® 1500P blanks over a range of apparent cooling rates. A brief description of these experiments is given here while a more detailed review can be found in [24]. The quenched blanks were subsequently machined into miniature dogbone style specimens and tested in uniaxial tension as discussed in a forthcoming section of this article.

The boron steel blanks were instrumented with thermocouples and a measured temperature versus time history plot is shown for a single test (heat and quench) in Fig. 2a. The blanks were heated up to 900 °C, at which point the austenization process began and the temperature increased to a maximum of approximately 973 °C in 4 min and 20 s. Upon completion of the austenization process, the blanks were manually transferred to the FAQA which resulted in a temperature drop to approximately 950 °C prior to quenching.

Fig. 2b shows the average (of 6 repeat tests) temperature versus time curves for five quench conditions imposed by the FAQA. The cooling rates in these experiments, as in actual hot stamping conditions, are not constant and for this work an "apparent cooling rate" was defined to characterize the quench conditions. To define the apparent rate of cooling, the temperature versus time curves were examined and the start of the austenite-bainite or austenite-martensite transformation was identified. This corresponds to the inflection point as shown in Fig. 2b for an austenite–bainite case. The apparent cooling rate is simply defined as the temperature drop divided by quenching time at the onset of transformation. This is equivalent to a constant cooling rate which corresponds to the conditions used to create continuous cooling transformation (CCT) diagrams. The dashed line in Fig. 2b shows the constant cooling rate curve plotted for this "apparent cooling rate". Using this method to define the apparent cooling rate, the following apparent rates were calculated for the FAQA test conditions; 14, 17, 24, 28 and 50 °C/s as shown in Fig. 2b. By overlaying the USIBOR® 1500P CCT diagram [25] in Fig. 2b, the austenite transformed into bainite for the lowest cooling rate while a fully martensitic phase transformation occurred at the highest apparent cooling rate. This was confirmed in a phase identification study that is presented in the next section of this article.

A CNC milling machine was used to cut the quenched blanks into miniature dogbone specimens. The specimens were flushed with coolant during machining and the depth of cut was small in order to ensure that heating of the specimens was minimized.

2.3. As-quenched phase identification

For each quench condition, the average measured temperature versus time curves from the FAQA experiments (Fig. 2b) were based

Table 1
Composition of USIBOR® 1500P sheet metal used in this work (wt. %).

C	Mn	B	Si	P	Cu	Ni	Cr	Al	Ti	Mo
0.22	1.23	0.004	0.25	0.008	0.03	0.02	0.20	0.03	0.037	<0.02

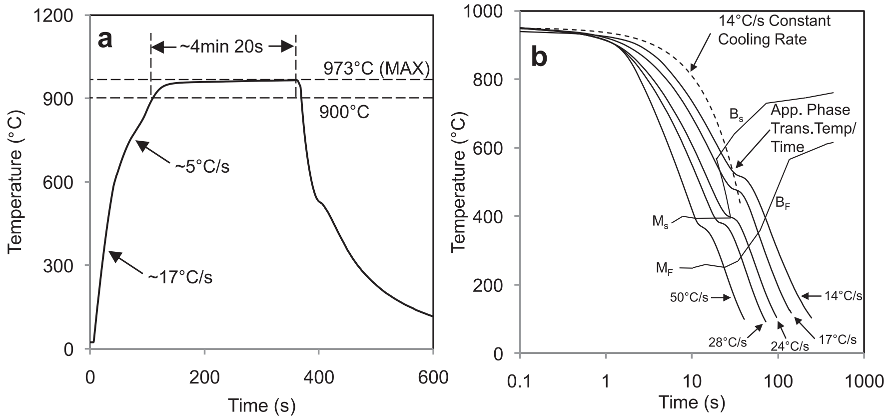

Fig. 2. (a) The measured temperature versus time history of an FAQA specimen that was quenched at 14 °C/s (b) Average measured temperature versus time curves for the five quench conditions tested in the FAQA. The overlaid CCT diagram is for USIBOR® 1500P that was austenized with similar composition and temperature versus time conditions used in the FAQA tests [25].

on 6 repeat measurements. Although the temperature versus time measurement repeatability was good [24], small changes in the temperature versus time due to the manual nature of the FAQA experiments resulted in small Vickers hardness variations, due to consequent variation of the as-quenched volume fractions of daughter phases. In an effort to minimize the volume fraction variations for the purpose of quantifying the as-quenched phases, a Gleeble thermo-mechanical apparatus was used to prescribe the average measured temperature versus time history from the FAQA experiments to boron steel specimens. The Gleeble processed specimens were then polished and etched to reveal the as-quenched phases using scanning electron microscopy. Also, the dilation of the specimens was measured during quenching and the data was used to indicate the start and finish of the decomposition of austenite into daughter phases.

Gleeble Experiments – A Gleeble 3500 Thermo-Mechanical simulator was used to simulate the FAQA experiments by prescribing the average temperature versus time histories shown in Fig. 2b. A schematic of the specimen geometry is shown in Fig. 3a with the control thermocouple location indicated and the longitudinal axis being parallel to the rolling direction of the sheet. The specimen prior to testing in the Gleeble is shown in Fig. 3b. The quench media was compressed air which was applied using quench heads positioned above and below the specimen. The upper quench head can be seen in Fig. 3b. The quartz C-gauge shown in Fig. 3b was used to measure the change in width (or dilation) of the sheet metal specimen during quenching. The dilation measurements were used to indicate the start and finish temperature of phase transformations. The C-gauge and thermocouple data acquisition frequency was 200 Hz during quenching.

The average measured temperature versus time history from the FAQA experiments (Fig. 2b) was used to prescribe the input temperature versus time for the Gleeble tests as shown by the blue curves in Fig. 3c. Prior to quenching, the specimens were heated at 17 °C/s up to 600 °C, then at 5 °C/s up to 900 °C, at which point the austenization process began and the temperature increased to a maximum of 973 °C in 4 min and 20 s. Upon completion of the austenization process, the specimens were allowed to cool to 950 °C, to replicate the heat loss due to transfer from the furnace to the FAQA apparatus, and then quenched. The measured temperature versus time histories for the five different quench conditions are plotted as the thin black curves with open circular markers in Fig. 3c. The excellent temperature versus time control of the Gleeble apparatus resulted in nearly no deviation between the prescribed and measured curves.

Metallography – The thermally processed specimens from the Gleeble experiments were cut at the control thermocouple location and prepared for metallographic examination. The specimens were mounted in epoxy resin, ground and polished to a mirror finish using 500, 1200 and 4000 grit SiC paper; followed by 3 and 1 μm diamond paste. A 2% Nital etching solution was used to reveal the microstructure. A JEOL JSM 840 scanning electron microscope (SEM) was used to create micrographs of the variable cooling rate specimens using secondary electron imaging (SEI). The area fraction of the phases present within each micrograph was quantified by manually selecting the phases using image analysis software and conducting a pixel count. The section area used to quantify the area fraction was from the plane normal to the longitudinal axis of the specimen (see Fig. 3a) and at the control thermocouple location. The area of the section was 510 μm (along the sheet mid-plane to surface direction) by 350 μm wide. This area was composed of six smaller micrographs that were individually quantified.

2.4. Micro-hardness

Micro-hardness measurements were made with a LECO MHT Series 2000 hardness tester using a 1000 g load. All of the specimens used for hardness measurements were mounted in epoxy resin, ground and polished to a mirror finish using 500, 1200 and 4000 grit SiC paper; followed by 3 and 1 μm diamond paste. For the specimens quenched using the FAQA apparatus, three blanks were randomly selected for each quench conditions. Hardness specimens were cut from the blanks and the hardness was tested through the thickness of the sheet at a location that corresponds to the centre of the gauge length of the subsequently cut tensile specimens (see [24] for a schematic of the location). The hardness was measured at five locations through the thickness of each hardness specimen. The hardness of the specimens processed with the Gleeble was measured through the thickness of the sheet (at five locations) and at the control thermocouple location, as shown in Fig. 3a.

2.5. Uniaxial tension testing

Uniaxial tension tests were conducted on specimens that were machined from the blanks quenched in the FAQA at the following nominal strain rates; 0.003, 1.0, 85 and 1075 s^{-1}. The following

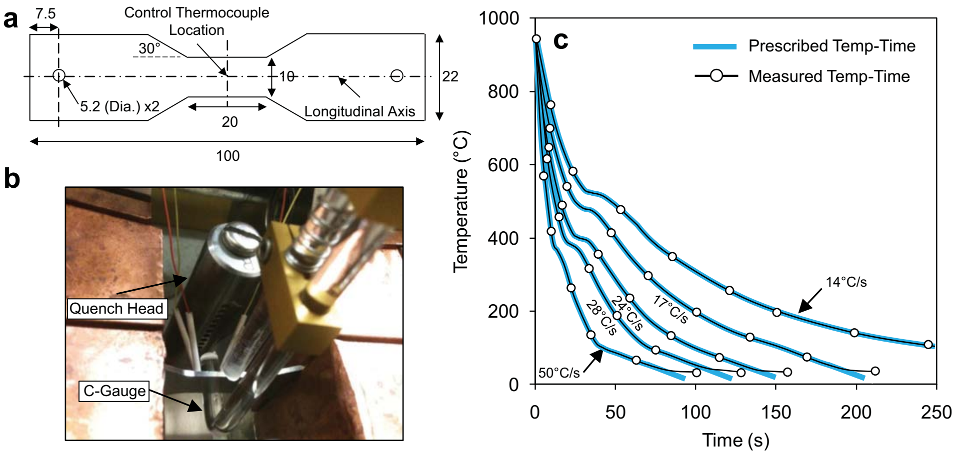

Fig. 3. (a) Gleeble specimen geometry [dimensions are in mm] (b) The specimen shown prior to testing with the C-gauge and quench head (c) The input and measured temperature versus time histories from the Gleeble experiments. (For interpretation of the references to colour in this figure legend, the reader is referred to the web version of this article.)

section briefly describes the specimen geometry and equipment used to conduct the uniaxial tension tests.

Specimen Geometry – The miniature dog-bone style specimen (see Fig. 4) used in this work was developed by Smerd et al. [26] for aluminium alloy sheet metal. Small sample gauge lengths are mandated in high rate testing to minimize signal rise time and achieve very high strain rates. Smerd et al. [26] demonstrated that that stress versus strain curves from quasi-static tension tests conducted on ASTM (E 8M-04) specimens matched those of the miniature specimens up to the ultimate tensile strength (UTS), which is acceptable since the flow stress is of importance in constitutive models. This correlation was also confirmed in the current work. Subsize ASTM (E 8M-04) specimens were cut from the quenched blanks and tested in tension at a strain rate of 0.003 s^{-1}. Fig. 4 plots the resultant engineering stress versus strain curves (up to UTS) for the subsize ASTM and miniature dog-bone specimens, which agree with each other and justify the use of the miniature specimens for this work.

Quasi-Static Strain Rate – An Instron model 1331 servo-hydraulic testing machine was used to conduct the quasi-static strain rate tests. Specimen elongation was measured using a ±5 mm extensometer and the specimens were mounted in a pair of custom grips as shown in Fig. 5a. Cross-head velocities of 0.0375 mm/s and 1.0 mm/s were used to deform the specimens at true strain rates of 0.003 s^{-1} and 0.9 s^{-1}, respectively.

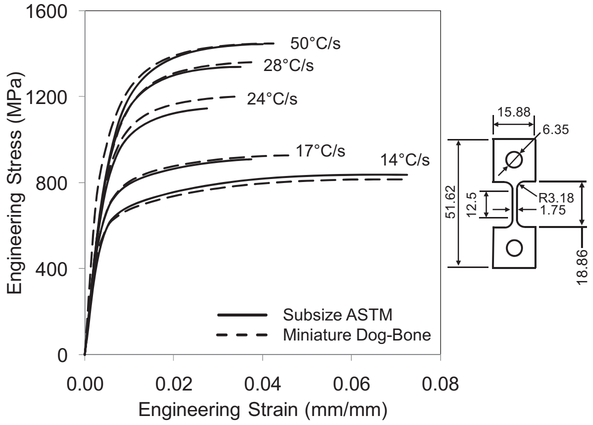

Fig. 4. Engineering stress versus strain curves (up to the UTS) of the miniature dog-bone and subsize ASTM specimens (at 0.003 s^{-1}).

Intermediate Strain Rate – Intermediate strain rate tests were conducted using an IMATEK instrumented falling weight impactor (IFWI) which is also known as a drop tower. A schematic of the IFWI is shown in Fig. 5b while a more rigorous description of the apparatus can be found in [27]. The specimen is attached to a fixed upper grip and then loaded in tension by a free falling striker. Load is measured using a Kistler piezoelectric load cell and an enhanced laser velocity system (ELVS) is used to measure the displacement of the lower grip. Due to the nature of the IFWI apparatus, wave effects cause ringing in the force-time signal, resulting in force data that contains oscillations. To combat these effects, rubber damping pads were placed at the striker/lower grip interface, as shown in Fig. 5b. These pads serve to dampen the impact and thus reduce the oscillations in the force-time signal. Although the oscillations were reduced, the addition of the pads increase the rise time prior to which a constant strain rate is achieved. The raw force-displacement data measured during each test was manually post-processed using Microsoft Excel to determine the stress, strain, and strain rate. For this work, the weighted fork assembly was released from a height of 0.10 m (measured from the top of the rubber damping pads) to deform the specimen at an average true strain rate of 85 s^{-1}.

High Strain Rate – A tensile split Hopkinson bar (TSHB) apparatus was used to conduct high strain rate tension tests at an average true strain rate of 1075 s^{-1}. A photograph of the apparatus is shown in Fig. 5c and a detailed description of the equipment and methods used to calculate the engineering stress versus strain can be found in [26,27], while a brief review follows. For the current work, 15.88 mm (5/8″) diameter aluminium round bar stock material was used for the incident and transmitter bars that had a length of 2057 mm and 1816 mm, respectively. In order to minimize wave distortion at the bar-specimen interface and provide adequate clamping force to prevent specimen slipping during loading, the miniature dog-bone specimens (see Fig. 4) were mechanically fastened to the bar ends as outlined by Smerd et al. [26]. The incident and transmitter bar strain gauge stations utilized a half-bridge configuration and a gas gun was used to propel

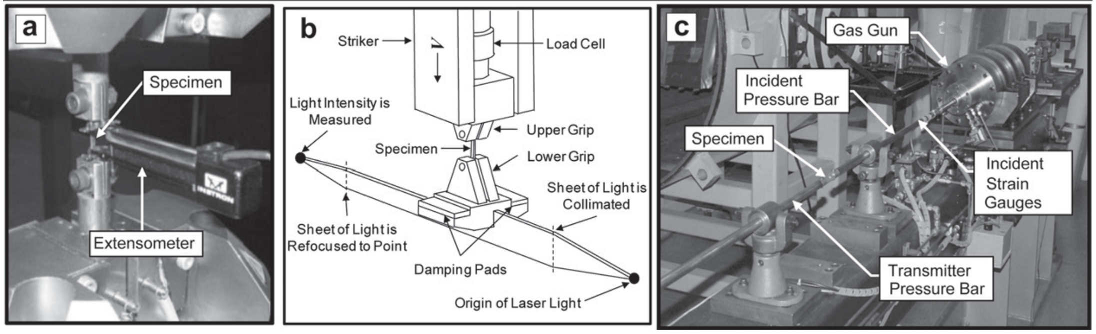

Fig. 5. (a) Quasi-static test apparatus (b) Instrumented falling weight impactor (IFWI) schematic and (c) Split Hopkinson tensile bar apparatus at the University of Waterloo.

a 508 mm (20″) hollow striker tube, located concentrically on the incident bar, towards an end cap, which generates the incident loading pulse. High speed amplifiers and a 20 M sample/s data acquisition system are used to excite the strain gauge stations and record the raw waveform data, respectively. The in-house TSHB post-processing software, CSHB [28], was used to separate the raw waveforms and conduct a spectral analysis to back-propagate the waves to the bar–specimen interface, which at the same time reverses the effects of wave attenuation and dispersion [28]. The code then uses classical Hopkinson bar equations [29] to determine the stress, strain, and strain rate from the waveform data.

Intermediate and High Strain Rate Test Specimen Elongation – A key difference in the strain measurements between the various test apparatus' used in this work lies in the gauge length over which the elongation is measured. The Instron tests utilize a clip-on extensometer which has a gauge length of 12.5 mm as shown in Fig. 5a. In contrast, because there is no "dynamic extensometer" for the IFWI apparatus, these experiments utilize the ELVS to measure the extension across the specimen shoulders which has a length of 18.86 mm (Fig. 4) and therefore also measures deformation that occurs outside of the gauge length region of the sample. The TSHB method measures the displacements at the bar ends which is equivalent to the measure of displacement in the IFWI experiments. This difference in specimen elongation measurement introduces additional deformation (primarily elastic) from outside the gauge length that is measured and when converted to engineering strain, results in a lower apparent or "effective" Young's modulus. In the current work, the use of an "effective modulus" in the calculation of effective plastic strain in each experiment serves to compensate for the different elongation measurements and provides a measure of effective plastic strain that is relatively insensitive to the manner in which elongation is measured. This approach reflects the fact that the majority of the deformation in the specimen shoulder is elastic such that the plastic deformation is essentially concentrated in the gauge length region of the sample.

2.6. True strain rates

The true strain rate versus true strain for a single test conducted at each nominal strain rate is shown in Fig. 6. For each repeat test, the true strain rate was calculated as the average strain rate from the apparent strain at yield to the end of the test and the average true strain rate for each quench rate condition is shown in Table 2. The strain rate curves shown for the 0.003 s^{-1}, 1.0 s^{-1} and 1075 s^{-1} tests in Fig. 6 indicate a constant strain rate throughout the loading duration of the specimen, while the strain rate for the 85 s^{-1} test increases during the initial loading of the specimen due to the use of damping pads in the IFWI tests.

3. Experimental results and discussion

The following sections present the measured phase area fractions, hardness measurements and stress versus strain curves as measured for the various quench conditions and strain rates.

3.1. Area fraction of the as-quenched phases

Samples of the SEM micrographs used to quantify the as-quenched area fraction of martensite and bainite for the Gleeble specimens are shown in Fig. 7 for the 14, 24 and 50 °C/s quench conditions. The 50 °C/s cooling rate specimen shown in Fig. 7a, exhibits the packets of the parallel lath crystals that are characteristic of martensite which contains less than 0.60% carbon [30,31]. The microstructure observed in Fig. 7c is that of ferritic bainite, as reported for similar materials/conditions by Feng et al. [32], Tariq et al. [33] and Saeglitz et al. [34]. The characteristic features of ferritic bainite are a ferrite matrix with dispersed cementite particles [35–37]. Although this microstructure appears to be primarily bainite, a small area fraction of an irregular constituent which appears to be martensite was observed, as shown in Fig. 7c. Similarly, the 50 °C/s specimens contained a small area fraction of a secondary phase which appeared to be bainite as indicated in Fig. 7a. Fig. 7b shows the mixed martensite–bainite

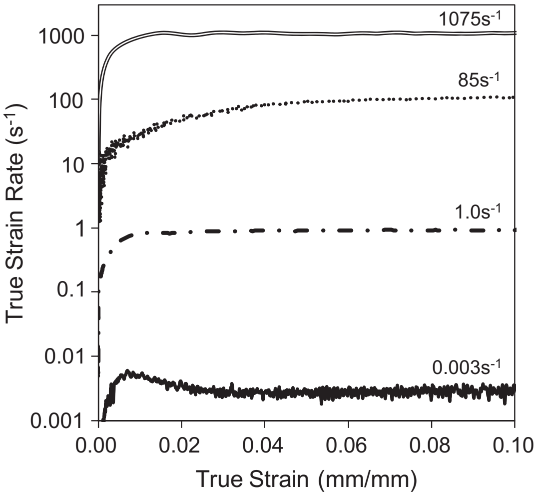

Fig. 6. True strain rate versus true strain curves for tests conducted at nominal strain rates of 0.003 s^{-1} to 1.075 s^{-1}.

Table 2
Mechanical properties of the specimens quenched in the FAQA under the various quench rate condition. The average Vickers hardness and area fraction of martensite/bainite measured from specimens processed using the Gleeble are shown as well.

App. cooling rate (°C/s)	Avg. Vickers hardness	Avg. Vickers hardness (Gleeble Exp.)	Avg. % area fraction martensite/bainite (Gleeble Exp.)	Avg. true strain rate (s^{-1})	Avg. ultimate tensile strength (MPa)	Avg. % area reduction
14	268	272	3%/97%	0.0028	816	70%
			Max: 3%/97%	0.9	833	–
			Min: 2%/98%	90	899	–
				1091	950	69%
17	318	283	12%/88%	0.0028	929	69%
			Max: 15%/85%	0.9	967	–
			Min: 10%/90%	84	1022	–
				1098	1054	69%
24	399	392	57%/43%	0.0028	1203	63%
			Max: 61%/39%	0.9	1235	–
			Min: 50%/50%	81	1299	–
				1074	1365	64%
28	442	449	86%/14%	0.0028	1360	63%
			Max: 89%/11%	0.9	1380	–
			Min: 80%/20%	82	1420	–
				1063	1537	62%
50	466	472	97%/3%	0.0028	1447	58%
			Max: 99%/1%	0.9	1457	–
			Min: 94%/6%	83	1511	–
				1053	1617	57%

microstructure for the 24 °C/s specimen. Based on the bainite and martensite phase structure characteristics, the area fraction of martensite and bainite was quantified for each condition and is reported in Table 2.

The decomposition of austenite into daughter phases results in a volumetric change due to the difference in crystal structure between the phases. Dilatometer experiments are typically conducted under constant cooling rates to measure these phase transformations, which are used to construct continuous cooling transformation (CCT) diagrams such as the one shown in Fig. 1 [36–38]. For this work, dilatometer type experiments were conducted and the change in the specimen width (or dilation) was measured during quenching with the C-gauge shown in Fig. 3b. The C-gauge measurements were used to determine the start and finish of phase transformations, as shown by the dilation curves in Fig. 8. For this particular material, the CCT diagram provided by the supplier indicates that the decomposition of austenite to ferrite occurs at cooling rates less than 8 °C/s, therefore the transformation of ferrite is not expected for the quench conditions tested. The beginning and end of the phase transformations is clearly shown by the classic shape of the dilation curves and the martensite and bainite start temperatures are denoted as MS and BS respectively, while the martensite and bainite finish temperature are denoted as MF and BF respectively. Please note that the dilation at 800 °C was offset along the *y*-axis of the graph in Fig. 8 in order to distinguish the curves for clarity.

3.2. *Micro-hardness measurements*

The measured hardness distribution through the thickness of the FAQA specimens was relatively constant (see [24]) which indicates a homogenous microstructure for each quench condition. The average measured Vickers hardness (based on 15 individual measurements) is presented in Table 2 and plotted versus cooling rate as the black circular data points in Fig. 9a. A linear trendline (black dashed line) is shown to fit the average FAQA hardness measurements for cooling rates between 14 and 28 °C/s.

The average measured Vickers hardness of the specimens quenched with the Gleeble apparatus are shown in Fig. 9a as the blue data points. As expected, the average measured hardness of the FAQA and Gleeble specimens is similar and within the scatter of the data as shown by the error bars. The Gleeble 17 °C/s test condition resulted in a hardness that was 11% less than the FAQA result which may be due to some variability in the FAQA temperature versus time curves used to construct the prescribed temperature versus time input curves. A linear trendline (blue dashed line) is shown to fit the average Gleeble specimen hardness measurements for cooling rates between 14 and 28 °C/s and the similarity of the Gleeble and FAQA trendlines indicates that the as-quenched microstructures are similar as well. The average measured hardness of the Gleeble processed specimens is plotted versus the measured percent area fraction martensite for the five quench conditions in Fig. 9b. Note that 0% and 100% martensite area

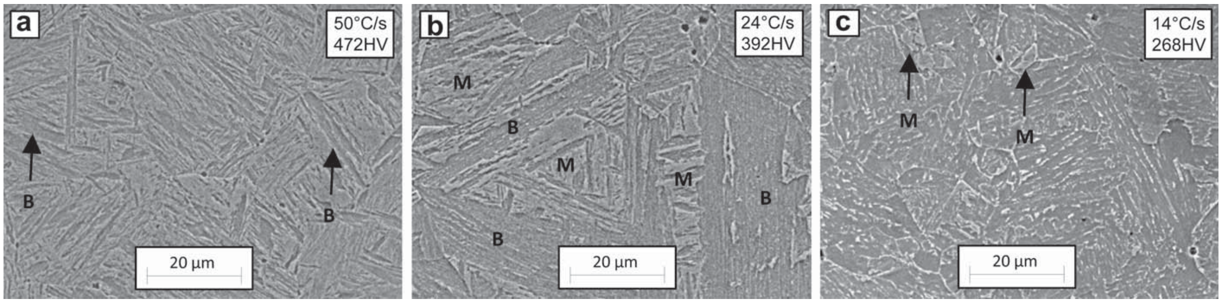

Fig. 7. SEM micrographs of the Gleeble specimens showing (a) an almost fully martensitic microstructure for the 50 °C/s specimen (b) a mixed bainitic/martensitic microstructure for the 24 °C/s specimen and (c) a predominantly bainitic microstructure for a 14 °C/s specimen. (B = bainite, M = martensite).

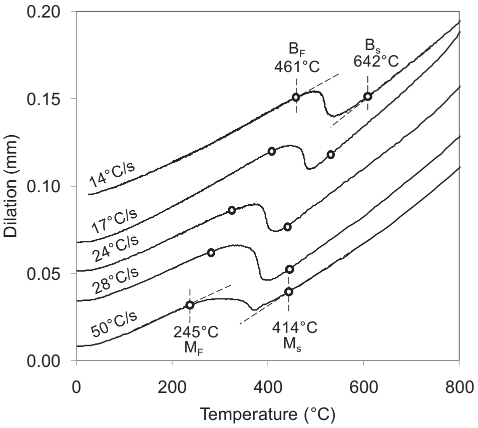

Fig. 8. The C-gauge (dilation) measurements from the Gleeble tests.

fractions refer to 100% and 0% bainite area fractions, respectively. A linear trendline was fit to the data and is shown as equation (1), where HV is the Vickers hardness number and %*M* refers to the area fraction of martensite (the balance of the area fraction being bainite). As an indication of the goodness of fit, the *R*-squared value was calculated to be 0.997, which suggests a strong linear relationship between Vickers hardness and area fraction of martensite and bainite present in the microstructure.

$$\mathrm{HV} = 217.85(\%M) + 263.15 \qquad [1]$$

3.3. Engineering stress versus strain results

Fig. 10 presents the engineering stress versus strain curves for all of the quench conditions tested in this work. The thin grey curves are the individual tests and the thick black curves indicate the average interpolated curves. To calculate an average interpolated curve for each quench condition, the raw data set was interpolated at strain increments of 0.00025. The interpolated curves were then used to create a single average curve for each cooling rate and strain rate as shown by the thick black curves in Fig. 10. The scatter in the repeat tests was greatest for the 17 °C/s, 24 °C/s and 28 °C/s tests because the as-quenched microstructure of these specimens contained a mixed area fraction of martensite and bainite, as shown in Table 2. The ratio of martensite to bainite and resulting strength is much more sensitive to variations in the FAQA quench experiments than the fully martensitic (50 °C/s) and fully bainitic (14 °C/s) material conditions. For the cooling rate conditions which were more repeatable, three repeat tests were used to establish the average curve. For the intermediate quench rate conditions, up to 14 repeat tests were conducted for each condition.

The ultimate tensile strength (UTS) was extracted from each test and used to determine an average UTS for each cooling rate and strain rate is reported in Table 2. The average UTS is plotted against the true strain rate in Fig. 11a and the data for all of the cooling rates indicates that the strain rate sensitivity is low from 0.003 s^{-1} to 1.0 s^{-1} and moderate to high as the strain rate increases from 1.0 s^{-1} to 1075 s^{-1}. The average UTS for the 28 °C/s and 50 °C/s tests conducted at 1075 s^{-1} is slightly exaggerated due to the oscillation in stress level for these test conditions as shown in Fig. 10d. These elevated UTS values suggest that the higher quench rate conditions (or more martensitic) are more strain rate sensitive than the specimens quenched at the lower cooling rates, which would be a false assumption.

3.4. Flow stress results

All of the raw engineering stress versus strain curves were converted into the true stress versus effective plastic strain (or flow stress) curves, as shown by the thin grey curves in Fig. 12. Close examination of the quasi-static, IFWI and TSHB tests shows a slight variation in the elastic modulus, as shown in Fig. 10. The apparent modulus was used to calculate the effective plastic strain by subtracting the elastic strain from the total strain. This difference can be attributed to rise-time effects associated with the IFWI and TSHB experiments, as well as any small variations in alignment of the samples. Hence, an “effective modulus” was determined for every test by calculating the modulus from the raw engineering stress versus strain data. The raw flow stress data was then interpolated at strain increments of 0.00025 and the individual interpolated curves were used to create a single average flow stress curve for each quench rate condition as shown by the thick black curves in Fig. 12.

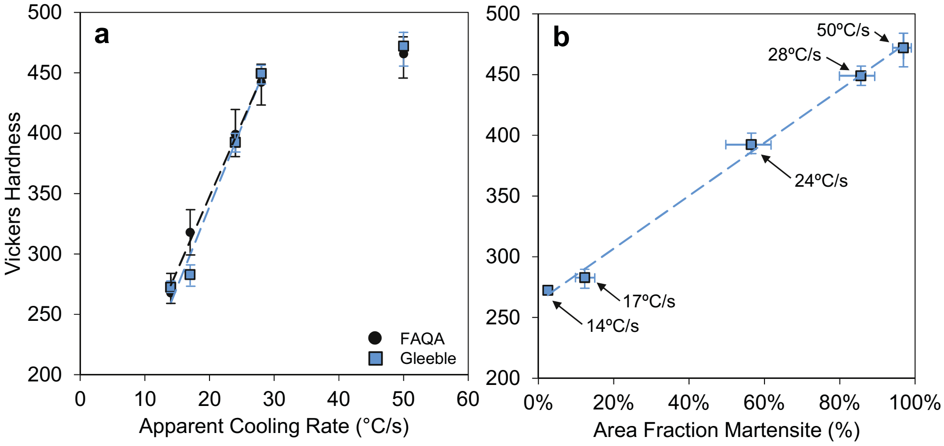

Fig. 9. (a) The average Vickers hardness measurements for the various cooling rate conditions. (b) The average Vickers hardness versus percent area fraction martensite for the specimens thermally processed with the Gleeble. Note that 0% and 100% area fraction martensite refers to 100% and 0% area fraction bainite, respectively. The vertical and horizontal error bars indicate the maximum and minimum measured values from the repeat measurements. (For interpretation of the references to colour in this figure legend, the reader is referred to the web version of this article.)

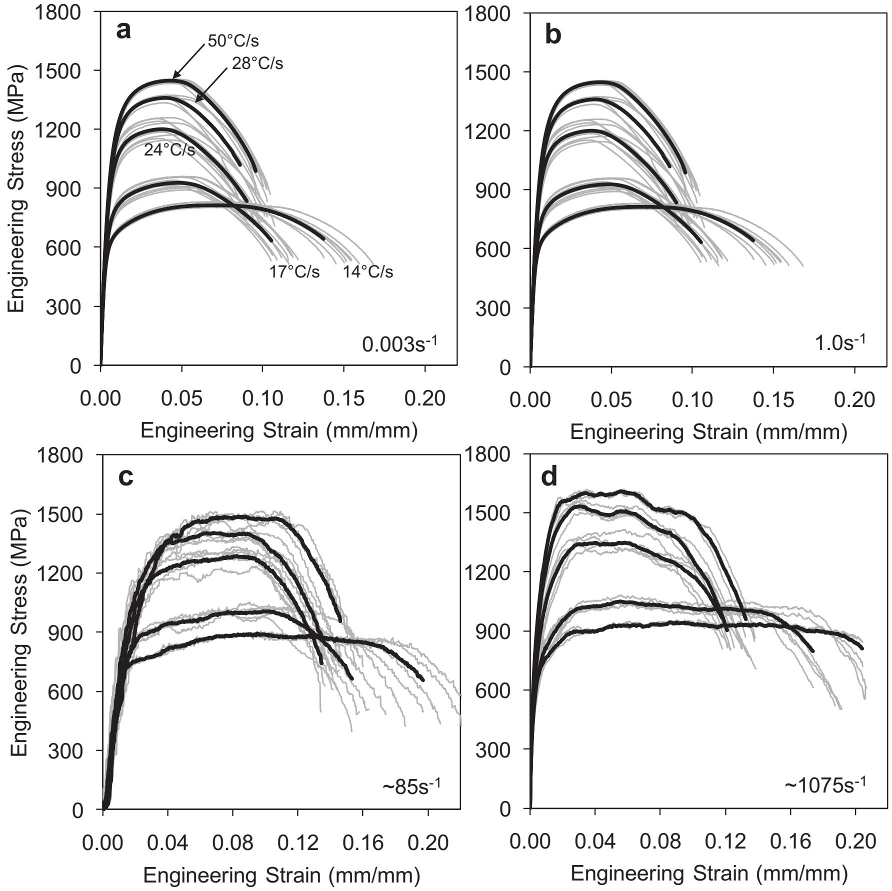

Fig. 10. The engineering stress versus strain curves measured at the following nominal strain rates (a) 0.003 s^{-1} [Quasi-Static] (b) 1.0 s^{-1} [Quasi-Static] (c) 85 s^{-1} [IFWI] and (d) 1075 s^{-1} [TSHB]. The thin grey curves are the individual tests and the thick black curves indicate the average interpolated curves.

Fig. 11b is a plot of the true stress (at an effective plastic strain of 0.025) versus true strain rate. The strain rate dependence of the true stress in Fig. 11b follows a similar trend to that observed in Fig. 11a for the UTS. The data indicates a small increase in stress from 0.003 s^{-1} to 1.0 s^{-1} and a moderate to high increase in stress as the strain rate increases from 1.0 s^{-1} to 1075 s^{-1}.

The average flow stress curves from the data presented in Fig. 12 are plotted together in Fig. 13 for the specimens quenched at

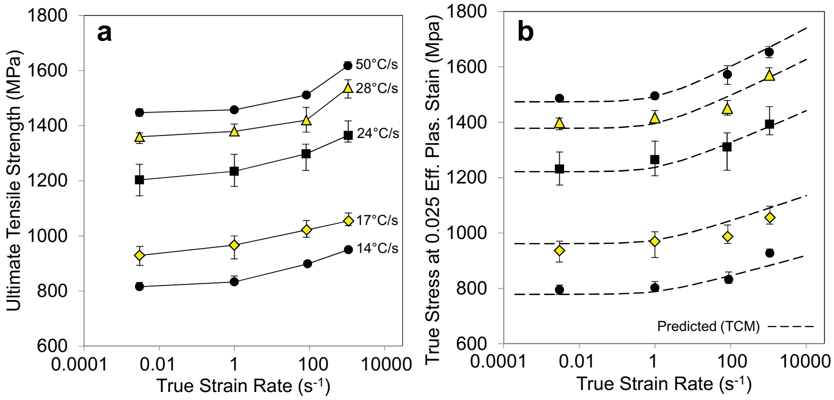

Fig. 11. Effect of strain rate on the (a) ultimate tensile strength and (b) true stress at 0.025 effective plastic strain for all of the quench conditions. The error bars indicate the maximum and minimum measured values from the repeat tests.

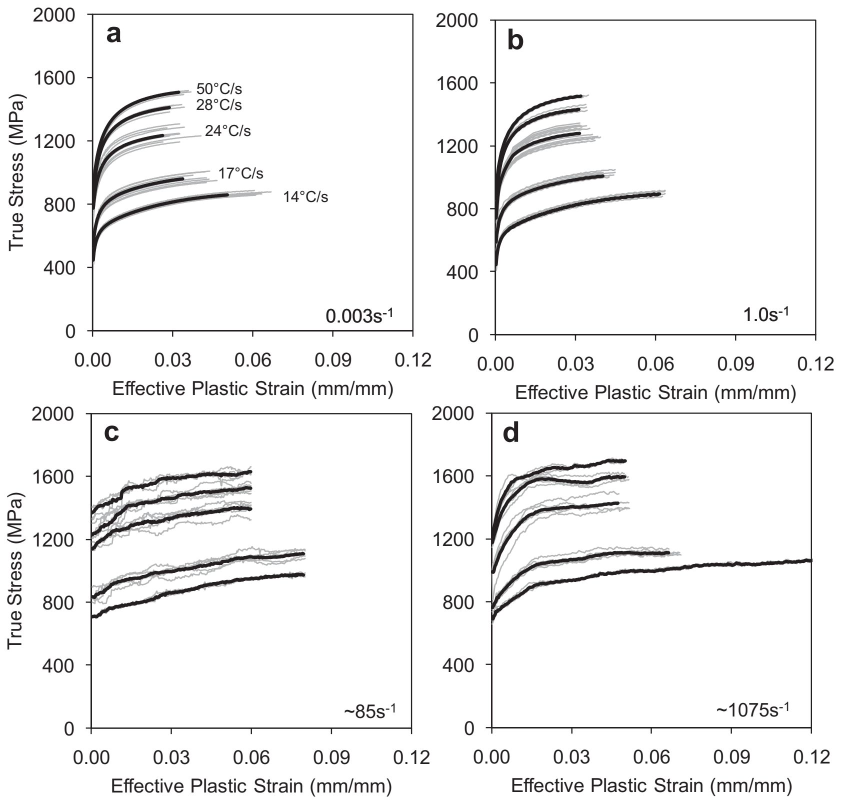

Fig. 12. The true stress versus effective plastic strain curves measured at the following nominal strain rates (a) 0.003 s^{-1} [Quasi-Static] (b) 1.0 s^{-1} [Quasi-Static] (c) 85 s^{-1} [IFWI] and (d) 1075 s^{-1} [TSHB]. The thin grey curves are the individual tests and the thick black curves indicate the average interpolated curves.

14 °C/s, 17 °C/s, 24 °C/s and 50 °C/s. The 28 °C/s flow stress curves were omitted for clarity. Due to the oscillation of the IFWI and TSHB stress data, the strain at UTS was difficult to determine, therefore, a larger part of the curve was used to create the flow stress curves and resulted in a greater effective plastic strain than the quasi-static curves shown in Fig. 13. The initial strain hardening behaviour (up to ~0.01 strain) observed in the quasi-static and TSHB tests was not observed for the intermediate rate IFWI tests. This may be due to the variation in strain rate (at low strains) during the IFWI test which is a direct result of the damping pads used to reduce oscillations in the stress data (see Fig. 6). The specimens quenched at 14 °C/s and 17 °C/s have a gradually increasing early strain hardening behaviour up to a strain of approximately 0.06, while the specimens quenched at 24 °C/s and 50 °C/s have a stronger hardening behaviour that appears to saturate at lower effective plastic strain levels.

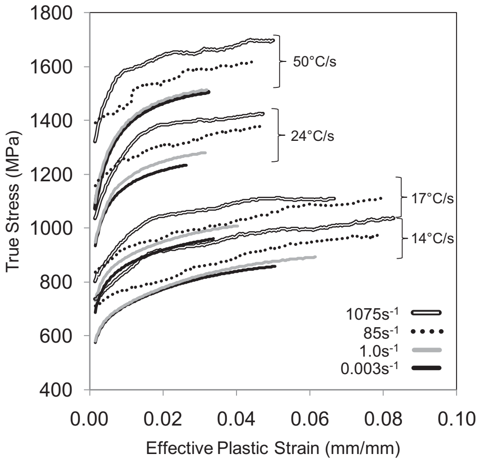

Fig. 13. The average flow stress curves for the specimens quenched at 14 °C/s, 17 °C/s, 24 °C/s and 50 °C/s. The 28 °C/s flow stress curves were omitted for clarity.

3.5. *Fractography*

A qualitative assessment of the fracture behaviour for the various quench conditions was conducted through metallographic observation of the tensile fracture surfaces using a JEOL JSM 840 scanning electron microscope (SEM) and an Olympus BH60 optical microscope. Specimens pulled at a strain rate of 0.003 s^{-1} were observed and Fig. 14a–c shows the SEM fracture surface images for the 14, 24 and 50 °C/s specimens. Specimens quenched at 14, 17, 24, 28, 50 °C/s and pulled at a strain rate of 0.003 s^{-1}, were mounted in epoxy resin and polished to reveal the cross-section optical microscope images of the fracture surface shown in Fig. 14d.

The 14 °C/s specimen exhibited ductile fracture behaviour as is evident from the fibrous fracture surface due to dimpling and void growth shown in Fig. 14a. Well defined and deep dimples are also shown in the higher magnification image on the right. Fig. 14d shows the classic cup and cone fracture surface, which indicates ductile fracture behaviour for the 14 and 17 °C/s quench conditions.

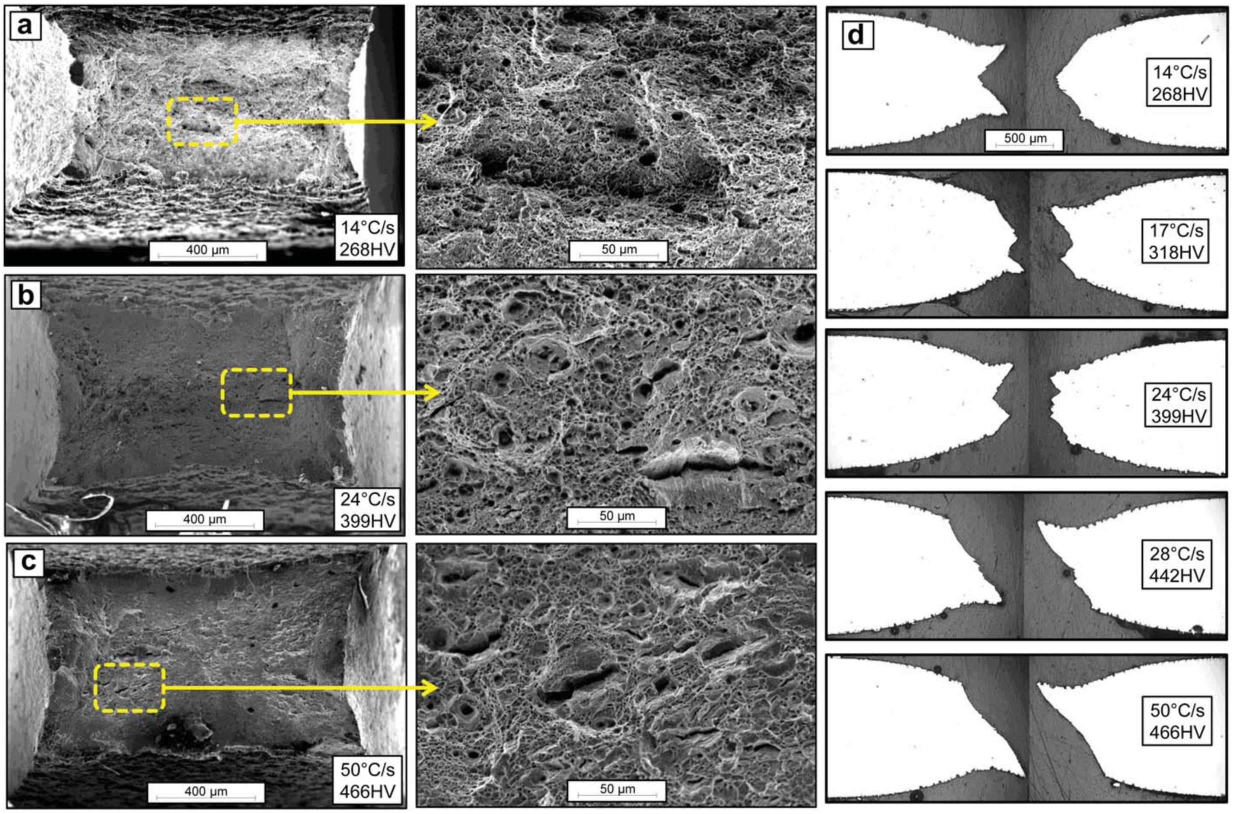

Fig. 14. SEM images of fracture surfaces for the (a) 14 °C/s (b) 24 °C/s and (c) 50 °C/s specimens pulled at a quasi-static strain rate (0.003 s^{-1}). (d) Optical microscope images of the fracture surface (cross-sectional views) for specimens quenched at 14–50 °C/s.

For the 24 °C/s cooling rate specimen in Fig. 14b, the fracture surface is planar with small fibrous regions that surround surface cracks. These characteristics are common to a material that behaves in a ductile-shear manner as can also be seen by the mixed ductile and shear fracture surface characteristics in Fig. 14d for the 24 °C/s specimen. A shear failure mechanism was evident for the 50 °C/s specimen as shown by the planar fracture surface in Fig. 14c. Large surface cracks surrounded by small fibrous regions with very shallow dimples confirm the shear fracture mechanism observed in these specimens. The large shear lips and smooth fracture surface shown in the optical images for the 28 °C/s and 50 °C/s specimens in Fig. 14d suggest shear fracture behaviour.

The reduction in cross-sectional area at the fracture surface of specimens pulled to failure was measured for all quench rate conditions. SEM images of the fracture surface were taken for all five quench condition specimens that were pulled under quasi-static (0.003 s^{-1}) and high strain rate (1075 s^{-1}) loading. For each condition, three specimens were measured and the average percent area reduction is plotted as a function of percent area fraction of martensite in Fig. 15a. The vertical scatter bands correspond to the range of the area reduction measurements and the horizontal error bars correspond to the variation in measured area fraction of martensite from the Gleeble specimens. As expected, the area reduction is greatest for the 14 °C/s specimens, which indicates good ductility, and lowest for the 50 °C/s specimens which fail in a shear manner and show poor ductility. The 17 °C/s to 28 °C/s specimens also show a lower area reduction as the area fraction of martensite increases. A linear trendline fit well to the data for both the quasi-static and TSHB data, indicating improved ductility as the area fraction of bainite increases for the measurements conducted in this work. The trendlines suggest that ductility slightly decreases for specimens pulled at higher strain rates, although the scatter in the measurements is relatively high for some of the measurements presented in Fig. 15a. It is interesting to note that the elongation to failure does not follow the same linear trend with respect to martensite fraction, rather a logarithmic trend as shown by the trendline in Fig. 15b for the quasi-static cases. This difference can be attributed to the elongation to failure being more a function of the necking and localization behaviour of the sample whereas reduction in area is more a measure of the material fracture strain, often after the onset of necking.

4. Constitutive model development

A variety of constitutive models have been developed to describe the flow stress of materials loaded at different strain rates. The Johnson-Cook [39,40] and Zerilli-Armstrong [41] constitutive models were fit to the flow stress data but were not able to capture the change in hardening behaviour for the various quench rate conditions.

The Voce [42] hardening model is primarily used to describe the flow stress of materials that exhibit a saturation in the stress level at relatively large strains. This saturation response corresponds to the end of the Stage III of multiple-stage work hardening shown by mono-crystalline materials [43]. The Voce model on its own is not strain rate sensitive, therefore the addition of a multiplicative strain

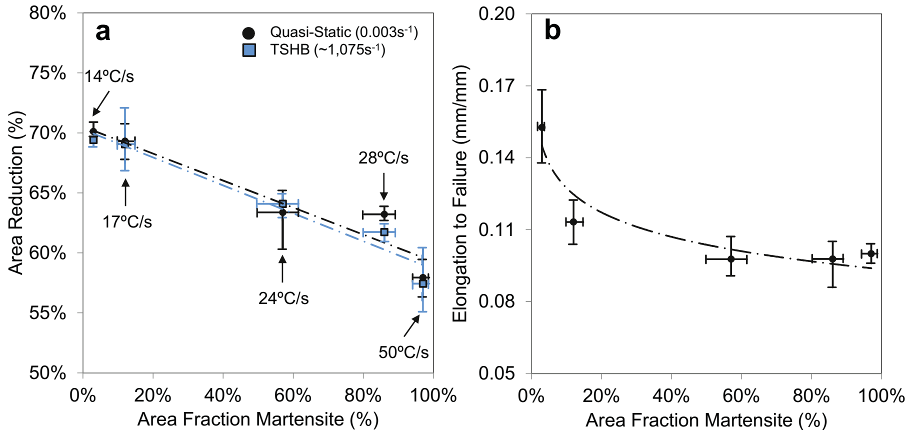

Fig. 15. (a) Percent area reduction versus % area fraction martensite. (b) The measured elongation to failure versus % area fraction martensite from the quasi-static (0.003 s^{-1}) tension tests. Note that 0% and 100% area fraction martensite refers to 100% and 0% area fraction bainite, respectively. The vertical and horizontal error bars indicate the maximum and minimum measured values from the repeat measurements.

rate sensitive term of the form adopted by Camacho and Ortiz [44] and implemented within a Johnson-Cook model for a high strength steel by Børvik et al. [45] was added as shown in equation (2). This exponential-type strain rate sensitivity term was selected because of the elevated strain rate sensitivity for the intermediate and high strain rate test conditions as measured in the experiments and shown in Fig. 11.

$$\sigma = \left[A + \left[(B - A)e^{-\frac{\varepsilon}{c}}\right]\right]\left[1 + \dot{\varepsilon}\right]^{D} \qquad [2]$$

where A is the saturation stress, B is the initial yield stress, C is the relaxation strain and D is the strain rate coefficient.

For the TSHB tests, heat generated within the specimen due to plastic work cannot be dissipated during the loading period and subsequently acts to thermally soften the material. The rise in

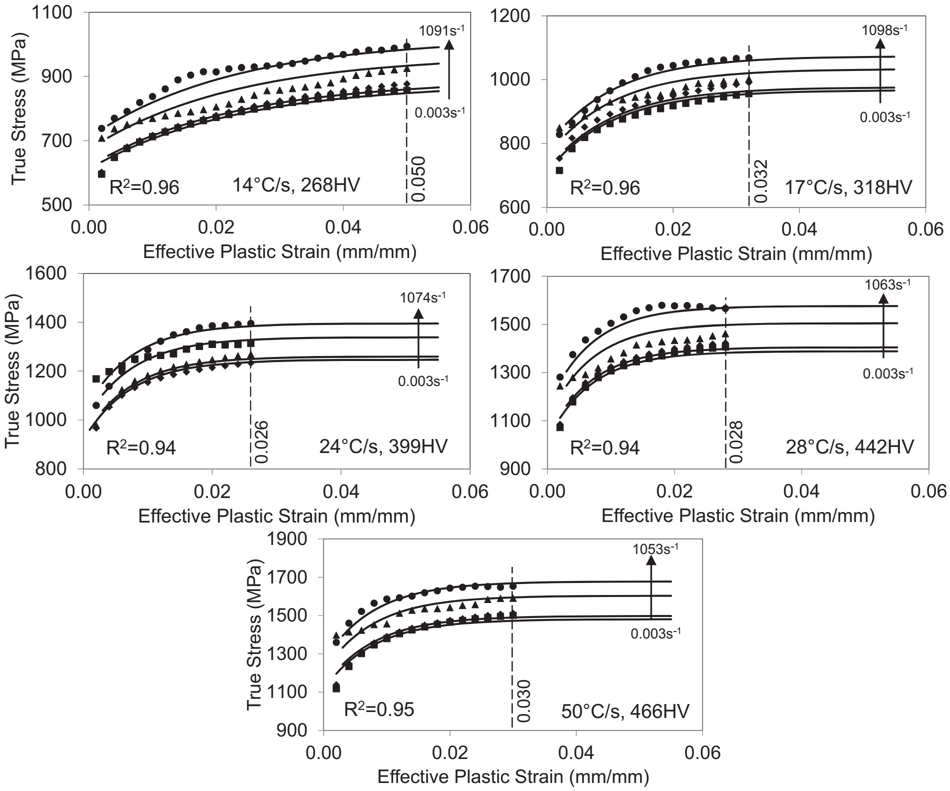

Fig. 16. Results of the Voce constitutive model (solid lines) fits to the measured flow stress data (data points).

Table 3
The Voce constitutive model parameters used for the constitutive fits shown in Fig. 16.

Apparent cooling rate (°C/s)	Vickers hardness (HV)	*A*, saturation stress (MPa)	*B*, yield stress (MPa)	*C*, relaxation strain (mm/mm)	*D*, strain rate coeff.
14	268	878.3	612.0	0.0229	0.0212
17	318	967.1	711.2	0.0105	0.0149
24	399	1246.9	918.0	0.0073	0.0161
28	442	1388.6	1019.7	0.0069	0.0182
50	466	1480.5	1113.6	0.0079	0.0180

temperature due to plastic work can be calculated using the following equation,

$$\Delta T = \frac{\beta}{\rho C_p}\int_0^{\varepsilon_p} \sigma d\varepsilon_p \qquad [3]$$

where ρ is the steel density, C_p is the specific heat capacity of the steel, β is the fraction of work converted into heat and the remainder of the equation is the area under the flow stress curve. Typically, a thermal softening term is added to a strain rate sensitive constitutive model but in this case, due to the relatively low strains at UTS observed for all of the quench conditions, the maximum rise in temperature for the 1075 s^{-1} test did not exceed 18 °C; therefore thermal softening was not accounted for in this model. While less rigorous, such an approach is often preferred in the crash modelling community since it reduces computational cost by avoiding a requirement to calculate temperature rise in vehicle crash simulations.

In order to fit equation (2) to the measured flow stress data, the average curves shown in Fig. 12 were first interpolated at strain increments of 0.002 as shown by the symbols in Fig. 16. For each quench rate condition, the interpolated data was truncated at the lowest measured strain value which was dictated by the quasi-static tests conducted at 0.003 s^{-1} and shown by the dashed line. The true strain rate used in the analysis for each condition was the average true strain rate measured from the tests and presented in Table 2. The statistical analysis software MYSTAT 12 was used for the non-linear regression analysis and the results of the fitted Voce constitutive model for each quench condition is shown by the black curves in Fig. 16. The Voce model was able to fit the data well and, as an indication of the goodness of fit, the *R*-squared values are also shown in the figure.

The Voce model parameters (*A*, *B*, *C* and *D*) are shown in Table 3 for each quench rate condition along with the Vickers hardness. As expected, the saturation stress (*A*) and initial yield stress (*B*) increase with Vickers hardness value. The relaxation strain (*C*) decreases for increasing hardness and then changes very little for the specimens quenched at 24 °C/s (399 HV) and higher which are fully martensitic. This material parameter is related to the hardening behaviour and shows that the higher strength materials reach their saturation stress at lower effective plastic strains than the lower strength materials, which was observed in the experiments. Also, the hardening behaviour remains relatively unchanged for hardness values greater than 399 HV. The strain hardening coefficient (*D*) describes the strain rate sensitivity and does not appear to change significantly for the different quench rate conditions.

The Voce constitutive model parameters (*A*, *B*, *C* and *D*) from Table 3 are plotted in Fig. 17a (the symbols) with respect to Vickers hardness. This parameter data was then fit with simple linear and polynomial mathematical expressions shown as equations (4)–(7) for which the constants are presented in Table 4. The fits are also plotted as black curves in Fig. 17a. The Vickers hardness was chosen to fit the Voce parameters rather than the apparent cooling rate because the constitutive response of the as-quenched material is defined by the final area fraction of martensite and bainite present in the microstructure which was shown to behave linearly with respect to Vickers hardness in Fig. 9b. In practice, the cooling rates in industrial hot stamping operations are not constant and it is not recommended to fit the Voce parameters with respect to cooling rate.

$$A\left(\mathrm{HV}\right) = A_2\mathrm{HV}^2 + A_1\mathrm{HV} + A_0 \qquad [4]$$

$$B(\mathrm{HV}) = B_1\mathrm{HV} + B_0 \qquad [5]$$

$$\begin{aligned} C(\mathrm{HV})_{266<\mathrm{HV}<375} &= C_3\mathrm{HV}^3 + C_2\mathrm{HV}^2 + C_1\mathrm{HV} + C_0 \\ C(\mathrm{HV})_{\mathrm{HV}>375} &= C_{0^*} \end{aligned} \qquad [6]$$

$$D(\mathrm{HV}) = D_0 \qquad [7]$$

$$\begin{aligned} \sigma &= f\left(\varepsilon, \dot{\varepsilon}, \mathrm{HV}\right) \\ &= \left[A(\mathrm{HV}) + \left[(B(\mathrm{HV}) - A(\mathrm{HV}))e^{\left(-\frac{\varepsilon}{C(\mathrm{HV})}\right)}\right]\right]\left[1 + \dot{\varepsilon}\right]^{D(\mathrm{HV})} \end{aligned} \qquad [8]$$

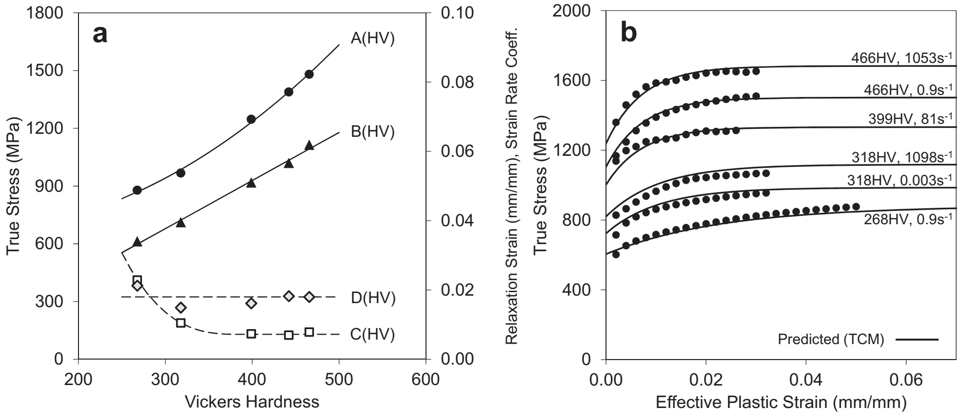

Fig. 17. (a) Voce material parameters plotted as a function of the Vickers hardness and (b) The measured (symbols) and TCM predicted (curves) flow stress curves for a variety of as-quenched Vickers hardness and strain rate values.

Table 4
The constant parameters for equations (4)–(7).

$A(\text{HV})$	–	$A_2 = 5.318 \times 10^{-3}$	$A_1 = -0.7902$	$A_0 = 699.49$
$B(\text{HV})$	–	–	$B_1 = 2.499$	$B_0 = -71.24$
$C(\text{HV})_{266<\text{HV}<375}$	$C_3 = -7.747 \times 10^{-9}$	$C_2 = 9.222 \times 10^{-6}$	$C_1 = -3.652 \times 10^{-3}$	$C_0 = 0.4884$
$C(\text{HV})_{\text{HV}>375}$	–	–	–	$C_{0^*} = 0.0072$
$D(\text{HV})$	–	–	–	$D_0 = 0.018$

The constant Voce constitutive model parameters in equation (2) were then replaced by equations (4)–(7) and the now modified-Voce constitutive model, referred to as the "Tailored Crash Model (TCM)", becomes a function of effective plastic strain (ε), true strain rate ($\dot{\varepsilon}$) and Vickers hardness (HV) as shown by equation (8). Alternatively, equation (8) can be expressed as a function of percent area fraction of martensite (%M) by substituting equation (1) for the variable HV in equation (8). This would allow further analysis of the hardening behaviour with respect to the material composition. The TCM accurately predicts the full range of flow stress curves quenched to various Vickers hardness values and deformed at different strain rates. Fig. 17b shows some of the measured experimental flow stress curves and the predicted flow stress curves using the TCM. Fig. 11b shows that the predicted (TCM) true stress at an effective plastic strain of 0.025 for the five different quench conditions matches the measured experimental data very well.

The TCM can be used to define the high strain rate constitutive properties of tailored hot stamped components in finite element (FE) crash simulations. In practice, component level or full scale vehicle crash models are preceded by a hot stamping simulation to predict the as-quenched microstructure within the tailored regions of a single part. Currently, LS-DYNA [46] contains the hot stamping constitutive model (*MAT_UHS_STEEL [47]) due to Akerstrom [5], which is used to model both the high temperature material properties and the phase transformation kinetics that predict the as-quenched percent volume fraction of daughter phases formed (martensite, bainite, pearlite and ferrite) and the corresponding Vickers hardness for each element in a hot stamping FE model. The Vickers hardness predictions for each element within a hot stamped FE model can then be used to define the crash model material properties with the TCM equations. Bardelcik et al. [48] outline a numerical procedure in which an impact model of a tailored hot stamping is developed and modelled using the TCM.

5. Conclusions

Based on the results presented in this article, the following conclusions can be made:

1. The Vickers hardness for the specimens quenched from 14 °C/s to 50 °C/s showed a linear dependence with respect to the percent area fraction of martensite/bainite present in the microstructure.
2. For all of the quench conditions, the low to high strain rate uniaxial tension data (UTS and flow stress) showed low strain rate sensitivity from 0.003 s^{-1} to 1.0 s^{-1} and moderate to high strain rate sensitivity from 1.0 s^{-1} to 1075 s^{-1}. For the highest quench rate condition, the strength was high and the ductility was low due to the fully martensitic microstructure. By introducing bainite into the microstructure, and thus tailoring the properties, the strength of the material was reduced and the ductility improved.
3. A Voce hardening model, coupled with an exponential-type strain rate sensitivity term was successfully fit to the experimental uniaxial tension data for all of the quench conditions. The model parameters were then fit with respect to hardness (or area fraction martensite/bainite) and a single constitutive model, the Tailored Crash Model (TCM) was developed and shown to accurately capture the change in hardening behaviour and strain rate sensitivity for the tailored material properties examined in this work.
4. SEM and optical microscope images of the fracture surfaces revealed that the specimens quenched at 14 °C/s behaved in a ductile fracture mode while the 50 °C/s quench conditions specimens displayed a strong shear fracture behaviour.

Acknowledgements

Support for this research from Honda R&D Americas, Promatek Research Center (Cosma International), ArcelorMittal, the Natural Sciences and Engineering Research Council, and the Ontario Research Fund is gratefully acknowledged. The help of Mr. Naveen Ramisetti of ArcelorMittal Global R&D in the identification of bainite and martensite was greatly appreciated.

References

[1] Altan T. Hot-stamping boron-alloyed steels for automotive parts, part I: process methods and used. Stamping Journal Magazine 2006:40–1.
[2] Aspacher J. Forming hardening concepts. In: 1st international conference on hot sheet metal forming of high-performance steel. Kassel, Germany: 2008. p. 77–81.
[3] Hein P. A global approach of the finite element simulation of hot stamping. Adv Mater Res 2005;6–8:763–70.
[4] Jonsson M. Press hardening, from innovation to global technology. In: 1st international conference on hot sheet metal forming of high-performance steel. Kassel, Germany: 2008. p. 253–65.
[5] Akerstrom P. Modelling and simulation of hot stamping. PhD. University of Lulea; 2006.
[6] Babbit M. Some highlights on new steel products for automotive use. Steel Res Int 2006;77(9–10):620–6.
[7] Karbasian H, Tekkaya AE. A review on hot stamping. J Mater Process Technol 2010;210(15):2103–18.
[8] Maikranz-Valentin M, Weidig U, Schoof U, Becker HH, Steinhoff K. Components with optimised properties due to advanced thermo-mechanical process strategies in hot sheet metal forming. Steel Res Int 2008;79(2):92–7.
[9] Munera DD, Pic A, Abou-Khalil D, Shmit F, Pinard F. Innovative press hardened steel based laser welded blanks solutions for weight savings and crash safety improvements. SAE Int J Mater Manuf 2009;1(1):472–9.
[10] Munera DD, Pinard F, Lacassin L. Very and ultra high strength steels based tailored welded blanks: a step further towards crashworthiness improvement. SAE Trans J Mater Manuf 2007;115(2006 Transactions):796–804.
[11] Wilsius J, Tavernier B, Abou-Khalil D. Experimental and numerical investigation of various hot stamped B-pillar concepts based on usibor 1500P. In: 3rd international conference on hot sheet metal forming of high-performance steel. Kassel, Germany: 2011. p. 427–35.
[12] Ma N, Hu P, Zhao YH. Research on tailored microstructure material in hot forming and its application. In: 3rd international conference on hot sheet metal forming of high-performance steel. Kassel, Germany: 2011. p. 331–40.
[13] Hein P, Wilsius J. Status and innovation trends in hot stamping of USIBOR 1500 P. Steel Res Int 2008;79(2):85–91.
[14] George R. Hot forming of boron steels with tailored mechanical properties: experiments and numerical simulations. Waterloo, Ontario, Canada: MASc, University of Waterloo; 2011. p. 1–123.
[15] George R, Bardelcik A, Worswick MJ. Hot forming of boron steels using heated and cooled tooling for tailored properties. J Mater Process Technol, in press, http://dx.doi.org/10.1016/j.jmatprotec.2012.06.028.
[16] Graff S, Gerber T, Lenze F, Sikora S. About the simulation of microstructure evolution in the hot sheet stamping process and the correlation of resulting mechanical properties and crash-performance. In: 3rd international conference on hot sheet metal forming of high-performance steel. Kassel, Germany: 2011. p. 323–30.
[17] Erturk S, Sester M, Selig M, Feuser P, Roll K. A thermo-mechanical-metallurgical FE approach for simulation of tailored tempering. In: 3rd international conference on hot sheet metal forming of high-performance steel. Kassel, Germany: 2011. p. 447–54.
[18] Svec T, Merklein M. Tailored tempering – heat transfer and resulting properties in dependecny of tool temperatures. In: 3rd international conference on hot sheet metal forming of high-performance steel. Kassel, Germany: 2011. p. 21–9.
[19] Uenishi A, Yoshida H, Kuriyama Y, Takahashi M. Material characterization at high strain rates for optimizing car body structures for crash events. Nippon Steel 2003:22–6.

[20] Mahadevan K, Liang P. Effect of strain rate in full vehicle frontal crash analysis. In: 2005 SAE World congress. Detroit, Michigan, USA: 2000.
[21] Chen XM, Shi MF, Chen G, Kamura M, Watanabe M, Omyia Y. Crash performances of advanced high-strength steels of DP780, TRIP780 and DP980. In: 2005 SAE World congress. Detroit, Michigan, USA: 2005.
[22] Simunovic S, Nukala PKVV, Fekete J, Meuleman D, Milititsky M. Modeling of strain rate effects in automotive impact. SAE Transactions: Journal of Materials & Manufacturing 2004;112:733–43.
[23] Bardelcik A, Salisbury CP, Winkler S, Wells MA, Worswick MJ. Effect of cooling rate on the high strain rate properties of boron steel. Int J Impact Eng 2010; 37(6):694–702.
[24] Bardelcik A, Wells M, Worswick MJ. The effect of cooling rate on the mechanical properties and energy absorption potential of hardened boron steel. In: 2nd international conference on hot sheet metal forming of high-performance steel. Lulea, Sweden: 2009. p. 105–13.
[25] ArcelorMittal – Usibor 1500P CCT diagram (personal communication); 2009.
[26] Smerd R, Winkler S, Salisbury C, Worswick M, Lloyd D, Finn M. High strain rate tensile testing of automotive aluminum alloy sheet. Int J Impact Eng 2005;32(1–4):541–60.
[27] Thompson AC. High strain rate characterization of advanced high strength steels. Waterloo, Ontario, Canada: MASc, University of Waterloo; 2006. p. 1–209.
[28] Salisbury CP. Spectral analysis of wave propagation through a polymeric Hopkinson bar. Waterloo, Ontario, Canada: MASc, University of Waterloo; 2001. p. 1–114.
[29] Gray III GT. ASM handbook: mechanical testing and evaluation. Materials Park, OH: ASM International; 2000. p. 462–476.
[30] Krauss G. Principles of heat treatment of steel. 1st. Ohio: American Society for Metals, Metals Park; 1980. p. 1–291.
[31] Naylor JP. Influence of the lath morphology on the yield stress and transition-temperature of martensitic–bainitic steels. Metall Trans A 1979;10(7): 861–73.
[32] Feng C, Fang H, Zheng Y, Bai B. Mn-series low-carbon air-cooled bainitic steel containing niobium of 0.02%. J Iron Steel Res Int 2010;17(4):53–8.
[33] Tariq F, Naz N, Baloch R, Ali A. Evolution of microstructure and mechanical properties during quenching and tempering of ultrahigh strength 0.3C Si–Mn–Cr–Mo low alloy steel. J Mater Sci 2010;45(6):1695–708.
[34] Saeglitz M, Bake K, Gernert U. Microstructure and mechanical properties in the transition zone of a low carbon steel after partial hardening. In: Ralf Kolleck, editor. Proceedings of IDDRG 2010 international conference. Graz, Austria: Graz University of Technology; 2010. p. 91–100.
[35] Bhadeshia HKDH, Christian JW. Bainite in steels. Metall Trans A 1990;21(4): 767–97.
[36] Porter DA, Easterling KE, Sherif MY. Phase transformations in metals and alloys. 3rd. Boca Raton, Florida: CRC Press; 2008. p. 1–520.
[37] Smith WF. Structure and properties of engineering alloys. 2nd. New York: McGraw-Hill; 1993. p. 1–630.
[38] Doane V, Kirkaldy JS. Hardenability concepts with applications to steel. New York: Metallurgical Society of AIME; 1978. p. 1–626.
[39] Johnson GR, Cook WH. A constitutive model and data for metals subjected to large strains, high strain rates, and high temperatures. In: 7th international symposium on mallistics; 1983. p. 541–7.
[40] Johnson GR, Cook WH. Fracture characteristics of three metals subjected to various strains, strain rates, temperatures and pressures. Eng Fracture Mechanics 1985;21(1):31–48.
[41] Zerilli FJ, Armstrong RW. Dislocation-mechanics-based constitutive relations for material dynamics calculations. J Appl Phys. 1987;61(5):1816–25.
[42] Voce E. The relationship between stress and strain for homogeneous deformation. J I Met 1948;74(11):537–62.
[43] Naderi M, Durrenberger L, Molinari A, Bleck W. Constitutive relationships for 22MnB5 boron steel deformed isothermally at high temperatures. Mater Sci Eng A–Struct Mater Prop Microstruct Process 2008;478(1–2):130–9.
[44] Camacho GT, Ortiz M. Adaptive lagrangian modelling of ballistic penetration of metallic targets. Int J Comp Meth Appl Mech Engng 1997;142: 269–301.
[45] Børvik T, Hopperstad OS, Berstad T, Langseth M. A computational model of viscoplasticity and ductile damage for impact and penetration. Eur J Mech A/Solids 2001;20:685–712.
[46] Hallquist JO. LS-DYNA keyword users manual, version 971. Livermore, California, USA: LSTC; 2007. p. 1–2206.
[47] Olsson T. An LS-DYNA material model for simulations of hot stamping processes of ultra high strength steels. In: 2nd international conference on hot sheet metal forming of high-performance steel. Lulea, Sweden: 2009. p. 43–9.
[48] Bardelcik A, Ghavam K, George R, Worswick MJ. An impact model of a hot stamped lab-scale b-pillar with tailored properties. In: 3nd international conference on hot sheet metal forming of high-performance steel; 2011. p. 221–8.

APPENDIX C: PART 3

Bardelcik A, Worswick MJ, Wells MA. The Influence of Martensite, Bainite and Ferrite on the As-Quenched Constitutive Response of Simultaneously Quenched and Deformed Boron Steel – Experiments and Model. *Submitted for possible publication*, 2012.

The Influence of Martensite, Bainite and Ferrite on the As-Quenched Constitutive Response of Simultaneously Quenched and Deformed Boron Steel – Experiments and Model

Alexander Bardelcik*, Michael J. Worswick, Mary A. Wells

University of Waterloo, Department of Mechanical and Mechatronics Engineering, 200 University Avenue West, N2L 3G1, Waterloo, Ontario, Canada

* Corresponding Author:
Ph: +1-519- 888-4567 ext. 36936, Fax: +1-519-885-8562, abardelc@uwaterloo.ca

ABSTRACT

This paper examines the relationship between as-formed microstructure and mechanical properties of hot stamped boron steels used in automotive structural applications. Boron steel sheet metal blanks were austenized and quenched at cooling rates of 30 °C/s, 15 °C/s and 10 °C/s within a Gleeble thermal-mechanical simulator. For each cooling rate condition, the blanks were simultaneously deformed at various temperatures. Approximately 0.20 strain was imposed in the middle of the blanks, from which miniature tensile specimens were extracted. Depending on the cooling rate and deformation temperature imposed on the specimens, some of the as-quenched microstructures consisted of predominantly martensite and bainite, while others consisted of martensite, bainite and ferrite. Optical and SEM metallographraphic techniques were used to quantify the area fractions of the phases present and quasi-static (0.003 s^{-1}) uniaxial tests were conducted on the miniature tensile specimens. The results revealed that an area fraction of ferrite greater than 6% led to an increased uniform elongation and an increase in *n*-value without affecting the strength of the material for equivalent hardness levels. This finding resulted in improved energy absorption due to the presence of ferrite and showed that a material with a bainitic microstructure containing 16% ferrite (with 257 HV) resulted in a 28% increase in energy absorption when compared to a material condition that was fully bainitic with a hardness of 268 HV. Elevated strain rate tension tests were also conducted at 10 s^{-1} and 80 s^{-1} and the effect of strain rate on the ultimate tensile strength (σ_{UTS}) and yield strength (σ_Y) was shown to be moderate for all of the conditions with an average increase in σ_{UTS} of ~80 MPa for an increase in strain rate from 0.003 s^{-1} to 80 s^{-1}. The true stress versus effective plastic strain (flow stress) curves generated from the tension testing were used to develop the “Tailored Crash Model II” (TCM II) which is a strain rate sensitive constitutive model that is a function of effective plastic strain, true strain rate and area fraction of martensite, bainite and ferrite. The model was shown to accurately capture the change in hardening behaviour and strain rate sensitivity of the multiphase material conditions examined.

Keywords: hot stamping, boron steel, tailored properties, phase transformations, constitutive model, rate sensitivity

1 Introduction

The current demand to reduce vehicle weight for improved fuel efficiency, while maintaining crash performance, has led to the application of new and innovative materials and manufacturing processes in the automotive industry. One such process is hot stamping of boron steel, which allows conventionally stamped parts to attain ultra high strength steel (UHSS) properties with tensile strengths on the order of 1500 MPa. The UHSS properties are a result of in-die quenching, which causes a hot blank to undergo a solid-state phase transformation from austenite to 100% martensite during the stamping process [1]. In order to achieve a fully martensitic phase transformation the hot stamping process must be designed to impose cooling rates greater than the critical cooling rate for the martensitic transformation, which is ~27 °C/s for the most commonly used boron steel grade, 22MnB5 [1-3]. The elevated strength of hot stamped parts allows the use of thinner gauge sheet metal, which results in weight reduction while maintaining structural integrity. The hot stamping process is currently used to manufacture structural components such as bumper beams, door intrusion beams, A- and B-pillars, roof and side rails [1,3-7], which are critical crash components, providing intrusion protection within vehicles.

Although components with a fully martensitic microstructure are often desired due to their exceptional high strength and intrusion resistance, some structural components, such as a B-pillar, may benefit from the introduction of regions of lower strength and greater ductility for improved energy absorption [8-13]. One method that lower strength/higher ductility regions can be realized is by locally reducing the cooling rate imposed on the blank to less than the critical cooling rate. The reduced cooling rate allows some volume fraction of the lower strength and more ductile bainite and/or ferrite phases to form. These lower (or sub-critical) cooling rates can be achieved by heating a portion of the hot stamping die, which is a technique know as in-die heating that is reviewed by Karbasian and Tekkaya [1] and George et al. [14]. In the work of George et al. [14] the in-die heating technique was successfully implemented in the hot stamping of a lab-scale B-pillar which resulted in tailored properties. They showed that the Vickers hardness of the tailored region was 52% less than the fully martensitic region and tension tests were conducted on a specimen cut from the tailored region which revealed that the ultimate tensile strength decreased by 49% and the uniform elongation increased by 84% when compared to the fully martensitic material state. For all of the heated die temperature conditions tested, it was found that the reduced hardness and improved ductility can be attributed to the presence of bainite and ferrite (in addition to martensite) within the as-quenched microstructure. The presence of ferrite was found to be more pronounced in regions of the B-pillar where deformation (thinning) was observed.

Plastic deformation during simultaneous quenching of a hot stamping boron steel was examined by Barcellona and Palmeri [15]. They used as Gleeble thermal-mechanical simulator to quench and isothermally deform a boron steel at various temperatures and quench rates. The results of their study revealed that plastic deformation caused the entire continuous cooling transformation (CCT) diagram to shift towards the left, or lower quench times. This phenomenon resulted in the decomposition of austenite into bainite and ferrite at quench rates for which these phase transformations would normally be suppressed. Also, the morphology of the bainite that was observed in the quenched and deformed specimens was that of granular bainite. Min et al. [16] conducted similar experiments to those presented in [15] and concluded that the increase in stored energy due to the plastic deformation of austenite contributes to increasing the driving force and shortening the incubation time for the ferrite phase transformation. The increase in driving force and shortening of the incubation time for the ferrite phase transformation was also shown to be increased as the deformation temperature was reduced. Unlike the granular bainite morphology reported by Barcellona and Palmeri [15], Min et al. [16] reported that bainite transformed at the austenite grain boundaries was *conventional bainite* (CB) and appeared as packets of parallel ferrite laths separated by a martensite-austenite constituent, while the bainite transformed at intergranular sites was *acicular ferrite* (AF) which grows as randomly oriented ferrite laths or groups of laths which contain discrete martensite-austenite particles. The CB and AF bainitic structures observed in this work were the same as those observed in a study by Zhang and Boyd [17] on bainite transformations of deformed austenite in a low-carbon microalloyed steel. Naderi et al. [18] conducted similar experiments in which a cylindrical 22MnB5 boron steel specimen was quenched at 50 °C/s and simultaneously deformed (in compression) at various temperatures within a dilatometer apparatus. The imposed deformation in their experiments resulted in the phase transformation of martensite and bainite and also indicated that the CCT diagram shifted towards the left and down. Abassi et al. [19] conducted isothermal hot compression tests using the same apparatus as in [18]. They showed that 50% deformation imposed at a quench rate of 50 °C/s resulted in the volume fraction of bainite and ferrite to increase as the deformation temperature was decreased from 900 °C to 650 °C. Nikravesh et al. [20] conducted experiments that were similar to those presented in [18]. They simultaneously quenched and compressed cylindrical specimens at various cooling rates and showed that the critical cooling rate (for a fully martensitic phase transformation) increased from 20 °C/s to 60 °C/s when approximately 40% plastic deformation was imposed. Micrographs of the quenched and deformed specimens revealed a greater area fraction of ferrite when compared to micrographs generated at equivalent cooling rates where no deformation was imposed. Shi et al. [21] used a Gleeble thermal-mechanical simulator to simultaneously quench and deform a 22SiMn2TiB hot stamping boron steel and concluded that the diffusional phase transformations of polygonal ferrite and bainitic ferrite were facilitated by the non-isothermal deformation during quenching. Fan et al. [22] conducted a smaller scale quenching/deformation study in which a small volume fraction of ferrite was detected in otherwise fully martensitic microstructures at quench rates of 25 °C/s and 30 °C/s for a boron steel.

Based on the above cited research, a considerable effort has been undertaken to understand (and show) the effect of deformation during simultaneous quenching on the final microstructure of hot stamped boron steels. For a *conventionally* hot stamped component which is fully martensitic, it is critical to avoid the transformation of bainite, ferrite or pearlite within the as-quenched microstructure. However, hot stamped components with *tailored properties* created through the in-die heating process depend on the phase transformations of the softer phases which result due to sub-critical cooling rates. It is inevitable that plastic deformation will occur during the hot stamping of a component with tailored properties and introduce some volume fraction of ferrite as shown in [14]. This is the main motivation for the current work which focuses on imposing various thermo-mechanical processing routes on a boron steel to produce as-quenched material conditions with varying volume fractions of martensite, bainite and ferrite. Characterization and quantification of the as-quenched phases, and data from mechanical testing (at various strain rates) of the mixed-phase material conditions is used to develop a strain rate sensitive constitutive model. The constitutive model developed in this work introduces the effect of ferrite to the TCM constitutive model developed by Bardelcik et al. [12] for as-quenched boron steel with a mixed volume fraction of martensite and bainite only.

2 Experimental Methods

2.1 USIBOR® 1500P Boron Steel

The boron steel sheet metal used for this work is USIBOR® 1500P which is produced by ArcelorMittal and has a nominal thickness of 1.2mm. This sheet metal has an Al-Si coating and the as-received microstructure of boron steel consists of ferrite/pearlite with a yield strength and ultimate tensile strength of 485 MPa and 612 MPa, respectively. The chemical composition of the steel is given in Table 1.

Table 1 - Chemical composition (wt. %) of the USIBOR® 1500P steel used in this work.

C	Mn	B	Si	P	Cu	Ni	Cr	Al	Ti	Mo
0.22	1.23	0.004	0.25	0.008	0.03	0.02	0.20	0.03	0.037	<0.02

2.2 Simultaneous Quench and Deformation Experiments

Boron steel blanks were quenched and simultaneously deformed in an effort to simulate the thermo-mechanical processing conditions present during a hot stamping process in which sub-critical cooling rates are imposed. A Gleeble 3500 thermo-mechanical simulator was used to heat up, austenize and quench boron steel blanks at constant cooling rates of 10 °C/s, 15 °C/s and 30 °C/s. For each cooling rate condition, the blanks were subjected to simultaneous hot deformation at a temperature of 800 °C and 600 °C as shown in the temperature versus time schematics in Figure 1a. In addition to the hot deformation tests, blanks were also quenched without deformation to serve as baseline conditions. Figure 1b is a photograph of the experimental setup within the Gleeble during the austenization process and Figure 1c shows the dimensions of the boron steel blanks used in this work. Custom quench heads with a large cooling zone were designed and built as a part of this work and shown in Figure 1b.

Prior to achieving the austenization temperature, the blanks were heated at 17 °C/s up to 600 °C, then at 5 °C/s up to 900 °C, at which point the austenization process began and the temperature increased to a maximum of 973 °C in 4 minutes and 20 seconds. This heating and austenization schedule replicates the average measured (via thermocouple) temperature-time for hot stamping experiments conducted by Bardelcik et al. [12]. Scanning electron microscopy was used to generate micrographs of rapidly quenched USIBOR® 1500P specimens that were subjected to the above mentioned austenization schedule. The martensitic microstructure formed within the prior austenite grains, whose grain boundaries were quite evident from which an ASTM grain size of 6.8 was measured. Upon completion of the austenization process, the specimens were allowed to cool to 950 °C, to replicate the heat loss due to transfer from a furnace during industrial hot stamping operations. Quenching initiated at 950 °C and the good thermal-mechanical control of the Gleeble resulted in almost no deviation from the prescribed temperature-time curves for all of the quench rates examined in this work. It should be noted that a small tensile pre-load was applied to the blanks in order to prevent buckling of the specimens due to the thermal expansion during heating and austenization. During quenching, the thermal contraction of the blank also contributed to the pre-load. The deformation imposed on the blank during each test was due to a 10 mm displacement of one end of the blank as indicated in Figure 1d. The deformation imposed in the region of interest was measured by scribing a line pattern onto the blank and using a strain grid measurement system with a micro-CCD video camera to measure the change is spacing (or strain) after thermo-mechanical processing. The 10mm blank displacement resulted in a deformation of approximately 0.20 engineering strain as indicated in Figure 1d. The deformation time for all of the tests was 0.5 s, therefore the nominal strain rate during deformation was approximately 0.4 s^{-1}, which is within the range of strain rates encountered during conventional stamping. The as-quenched boron steel blanks were surface ground (equally from both sides) to a nominal thickness of 1.0 mm while being flushed with coolant to minimize heating of the blank. Miniature dog-bone style tensile specimens were machined from the middle of each blank as shown by the overlaid specimen schematic in Figure 1d. A CNC milling machine was used to cut the tensile specimens, which were flushed with coolant during machining. The depth of cut was kept small in order to ensure that heating of the specimens was minimized.

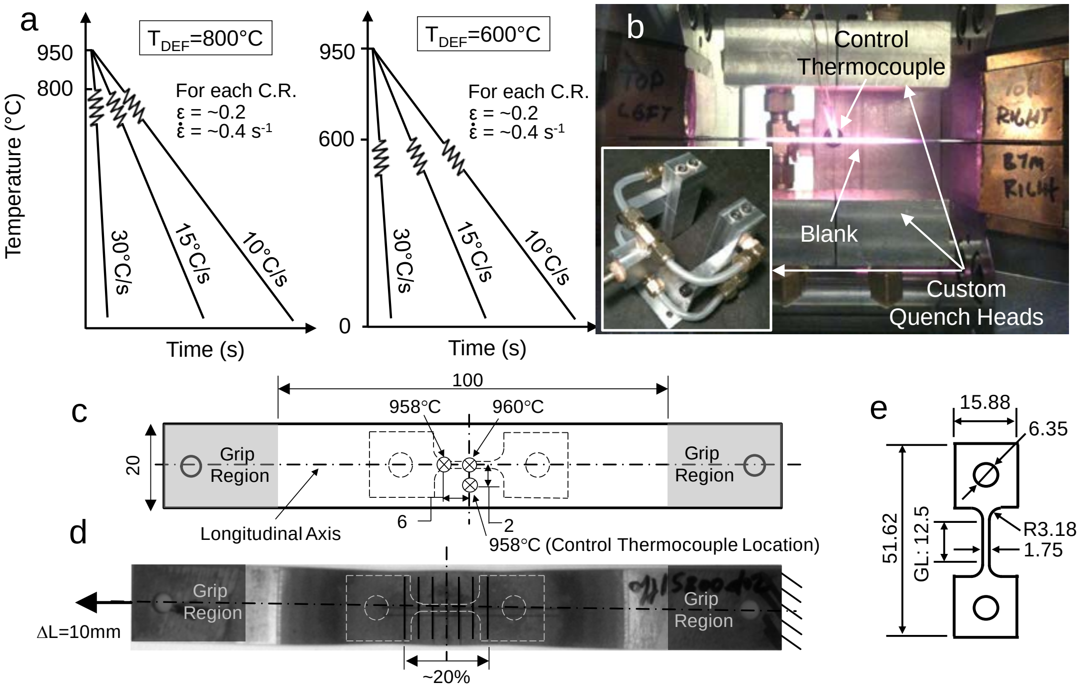

Figure 1 - (a) Temperature versus time schematic for the two hot deformation temperature conditions (b) An image of a Gleeble test showing the custom quench head and blank during austenization (c) A schematic showing the blank geometry, temperature distribution and an overlaid outline of the miniature dog-bone specimen geometry that was cut from the blank after thermal-mechanical processing. (d) An image of a blank that was quenched at 15 °C/s and deformed at T_{DEF}=800 °C (e) Dimensions of the miniature dog-bone specimen.

In order to ensure that the machined dog-bone specimens had a homogeneous microstructure throughout their gauge length, it was critical that the thermal gradient across the boron steel blank was minimal at the location where the gauge length of the tensile specimens was located, as shown in Figure 1c. Thermocouple measurements revealed that during the austenization process, the temperature was 2 °C lower at a position 6 mm (along the longitudinal axis) from the centre of the blank and 2 °C lower at 2 mm from the centre of the blank (perpendicular to the longitudinal axis) as shown in Figure 1c. This thermal gradient was small enough to ensure that the gauge region of the dog-bone specimens was subjected to a relatively uniform temperature-time schedule during quenching and deformation. Also, the deformation zone over which the strain was uniform and approximately 0.20, as shown in Figure 1d, was sufficiently large to contain the entire gauge length of the tensile specimens.

2.3 Metallography

In order to identify and measure the area fractions of the as-quenched phases present within the quenched and deformed blanks, a metallographic analysis was conducted for all of the conditions. For the phase identification analysis, a single specimen was observed for each quench rate/deformation condition. The authors recognize that a single part introduces uncertainty in the data and may not be representative of the sample population, but the excellent repeatability of the Gleeble apparatus (see [12]) supports the use of measurements from a single part. All of the specimens were mounted in epoxy resin, ground and polished using 500, 1200 and 4000 grit SiC paper, followed by 3 μm and 1 μm diamond paste. Two different metallographic observations were made on micrographs that were created using (i) scanning electron microscopy (SEM) images after etching with nital and (ii) a two-stage colour tint etching procedure that was used to reveal the various phases in different colours when observed with an optical microscope. The same procedure was undertaken in the work by George et al. [14] and it was shown that it is critical to have both the SEM and optical micrographs to discern some nuances in the bainitic and martensitic structures due to the different quenching/deformation conditions.

For the SEM procedure, specimens were etched with a 2% nital solution and a JEOL JSM 6460 SEM was used to create micrographs of the specimens using secondary electron imaging (SEI). High resolution micrographs revealed the characteristic structures of the various phases, but the images were not useful for quantifying volume fractions when multiple phases were present. The two-stage colour tint etching procedure adopted for this work was developed for multiphase steels by De et al. [23]. For the first stage, the specimens were etched in a picric solution that was followed by etching in a sodium metabisulfite solution. Details of the preparation and etching procedure can be found in [14]. Using this procedure, martensite is tinted brown, bainite is tinted black/blue and ferrite is revealed as white. The etched specimens were observed using an Olympus BH60 optical microscope equipped with ImagePro Plus image analysis software. The ImagePro Plus software was used to manually colour the various phases and subsequently conduct a pixel count to quantify the area fractions present. For each specimen, three 220 μm x 160 μm micrographs were used to generate an average measured area fraction. The optical micrograph images were extracted at the mid-thickness of the sheet and along the longitudinal axis as shown in Figure 1c. One image was taken at the center of the miniature dog-bone specimen gauge length, while the other two images were taken at a location that was approximately ± 5 mm from the center of the specimen gauge length.

2.4 Micro-Hardness

A LECO MHT Series 2000 micro-hardness tester (with 1000 g load) was used to measure the Vickers hardness in this work. All of the micro-hardness specimens were mounted in epoxy resin and polished to a mirror finish. The micro-hardness was measured along the gauge length of the subsequently cut miniature dog-bone specimens. A total of seven measurements were made for each specimen and the location of the indents was along the mid-thickness of the sheet and along the longitudinal axis as shown in Figure 1c.

2.5 Quasi-Static and Intermediate Uniaxial Tension Tests

Uniaxial tension tests were conducted on specimens that were machined from the quenched and deformed blanks at the following nominal strain rates; 0.003 s^{-1}, 10 s^{-1} and 80 s^{-1}. The following section briefly describes the specimen geometry and equipment used to conduct the uniaxial tension tests.

Specimen Geometry - The miniature dog-bone style specimen (see Figure 1e) used in this work was developed by Smerd et al. [24] for aluminum alloy sheet metal. The thermal-mechanically processed blanks shown in Figure 1d contain a uniformly quenched and deformed region that is too small to accommodate the gauge length of a conventional ASTM (E 8M) specimen; hence, the use of the miniature tensile specimen. For aluminium [24] and martensitic/bainitic steels [12], it was demonstrated that that stress versus strain curves from quasi-static tension tests conducted on ASTM (E 8M-04) specimens matched those of the miniature specimens up to the ultimate tensile strength (UTS), which is acceptable since this is the useful range of test data that can be used to develop constitutive models.

Quasi-Static Strain Rate - An Instron model 1331 servo-hydraulic testing machine was used to conduct the quasi-static, low strain rate tests. Specimen elongation was measured using a ±5 mm extensometer and the specimens were mounted in a pair of custom grips as shown in [12]. A cross-head velocity of 0.0375 mm/s was used to deform the specimens at a nominal strain rate of 0.003 s^{-1}.

<u>Intermediate Strain Rate</u> - The intermediate strain rate tensile experiments were conducted using a hydraulic intermediate strain rate (HISR) apparatus, which is shown in schematic form in Figure 2. The apparatus functions by accelerating the engagement sleeve to a constant velocity which then contacts the engagement piston at the bottom of the stroke at which point the specimen elongation commences. A KISTLER piezoelectric load cell, which is located directly above the upper grip assembly, measures the load during the test while an enhanced laser velocity system (ELVS) is used to measure the specimen elongation, as illustrated in Figure 2. Refer to [12] for a detailed explanation of the elongation measurement using the ELVS. The ELVS system is composed of a diode laser which emits a diverging sheet of light that is then collimated by a plano-cylindrical lens and fixed to a 25.4 mm width by a rectangular aperture. A convex lens is used to focus the laser sheet to a point, where the intensity is measured by a high-speed PIN photodetector. The intensity is converted to a voltage which is recorded by the data acquisition system and converted to elongation upon processing. The sample rate of the data acquisition was 60,000 samples/s for the 10 s^{-1} tests and 250,000 samples/s for the 80 s^{-1} tests. Due to electromagnetic noise present in the ELVS voltage signal, a running 25 point central average is applied to the signal upon processing. The load and displacement are acquired using a National Instruments data acquisition module that is coupled with a desktop computer. Due to the nature of the metal-on-metal contact within the engagement piston/sleeve assembly of the HISR, wave effects can cause ringing in the force-time signal, resulting in data that contains mechanical oscillations. To reduce ringing, a damper (rubber o-ring) is placed at the piston and sleeve interface, as shown in Figure 2. Although the oscillations were reduced substantially, the addition of the damper increases the rise time prior to which a constant strain rate is achieved; however, the rise time is confined to relatively low strain levels (~2%) which is judged to be acceptable. For this work, the velocity of the hydraulic actuator was 125 mm/s and 1000 mm/s to deform the specimen at a nominal strain rate of 10 s^{-1} and 80 s^{-1}, respectively.

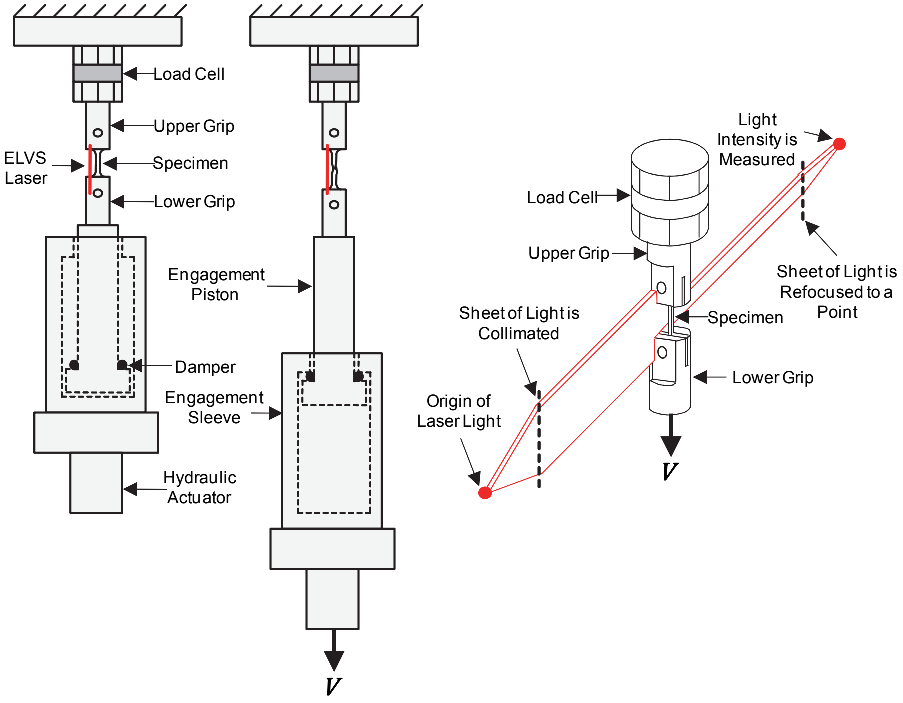

Figure 2 - A schematic of the Hydraulic Intermediate Strain Rate (HISR) apparatus.

True Strain Rates - The true strain rate versus true strain for a single test conducted at each nominal strain rate is shown in Figure 3. The strain rate becomes relatively constant after the approximate yield point (at ~ 0.01 true strain) is reached for all of the material conditions tested in this work. The effect of using a damper to prevent ringing in the force-time signal is evident in the slight delay in achieving a constant strain rate. The increased rise time is minimal and deemed to have a negligible effect on the test results. For each repeat test, the true strain rate was calculated as the average strain rate from a true strain of 0.02 to the end of the test. The average true strain rate for each quench rate condition is reported in the experimental results, below.

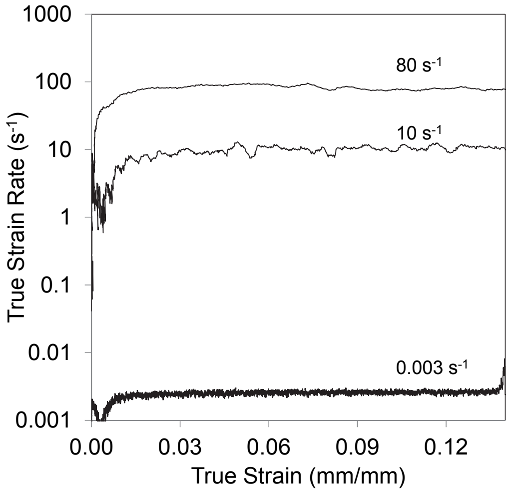

Figure 3 - True strain rate versus true strain for tests conducted at the three nominal strain rates. The results shown are for the following material condition C.R. = 30°C/s, T_{DEF} = 600 °C.

3 Experimental Results

3.1 Continuous Cooling Transformation Diagram (5 °C/s to 50 °C/s)

Figure 4a is a plot of the continuous cooling transformation (CCT) diagram for the material (coil) used in this study. The CCT was generated using a Gleeble 3500 thermal-mechanical apparatus with the same blank geometry and experimental procedure as described in [12]. Constant cooling rates were applied from a start temperature of 950 °C and varied from 5 °C/s to 50 °C/s. The heating and austenization schedule was the same as the schedule described in section 2.2. During quenching, the dilation of the blank was measured with a quartz C-gauge and the change in the constant dilation rate (with respect to temperature) was used to define the martensite and bainite, start and finish temperatures which are shown as the data points in Figure 4a. Approximate curves (dashed lines) were fit to the data points which indicate the shape of the CCT diagram. It should be noted that no metallographic analysis was conducted on the as-quenched microstructures to verify the phases present in the as-quenched condition, but due to the general CCT diagram supplied for this material by ArcelorMittal [2] and shown overlaid with the CCT diagram determined in this work in Figure 4b, one can assume that the transformation start temperatures indicated by the dashed lines are those for the martensite and bainite phase transformations. Because the transformation of ferrite occurs at cooling rates less than 8 °C/s for this material [2], the single data point labelled (F_S) is expected to be the ferrite start temperature since this point was due to a 5 °C/s cooling rate. The three constant cooling rates imposed in this work are shown in Figure 4a, along with the start of deformation for the T_{DEF}=600 °C and T_{DEF}=800 °C conditions. The temperature-time curves with simultaneous deformation shown overlaid on the CCT diagram in Figure 4a define the sub-critical cooling rates and deformation temperatures that will result in the as-quenched mixed phase material conditions examined in this work. From an industrial process perspective, similar cooling rates (albeit not constant) may be achieved in practice due to quenching within a heated die, thus defining a process window when hot stamping a tailored component.

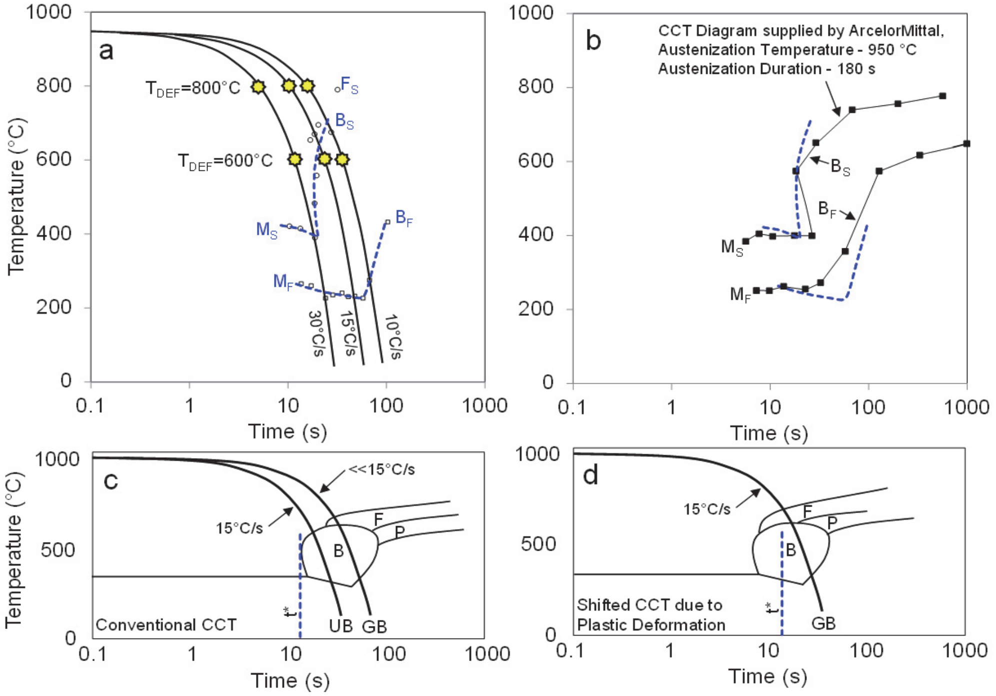

Figure 4 – (a) Continuous cooling transformation (CCT) diagram for the USIBOR® 1500P boron steel used in this work. This CCT was generated using cooling rates that varied from 5 °C/s to 50 °C/s. The three constant cooling rate curves shown in the CCT diagram are those from the measured control thermocouple temperature versus time data for the ND conditions. The stars indicated the time when simultaneous deformation occurred for the T_{DEF} = 600 °C and T_{DEF} = 800 °C conditions. M_S=martensite start, M_F=martensite finish, B_S=bainite start, B_F=bainite finish, F_S=ferrite start (b) A comparison of the CCT diagram generated for this work (dashed lines) and a general CCT diagram supplied for this material by ArcelorMittal [2]. (c) A schematic of a conventional CCT diagram and (d) a schematic of a shifted CCT diagram due to plastic deformation during quenching. B=bainite, M=martensite, F=ferrite, P=pearlite, UB=upper bainite type morphology, GB=granular bainite.

3.2 Effect of Quench Conditions on Measured Micro-Hardness

One miniature dog-bone specimen from each test condition was not tension tested, but instead was used to measure the micro-hardness along the gauge length, as shown in the Figure 5 inset. The measured hardness distributions are shown in Figure 5 and presented in Table 3 for each condition. Based on the fairly constant measured hardness distributions, the majority of the specimens are expected to have a homogeneous microstructure throughout the gauge length, but some results, such as the 30 °C/s specimen with T_{DEF} = 600 °C in Figure 5c, show a deviation from the average hardness which suggests that the microstructure may be slightly different. Figure 5d shows the average measured Vickers hardness versus cooling rate for the simultaneously quenched and deformed experiments. Also shown in Figure 5d is the standard deviation calculated for each quench condition. As expected, the no deformation (ND) average hardness for the 30 °C/s quench rate condition was 458 HV, which is in the expected range for a material condition that is predominantly martensitic [12,14,25]. The T_{DEF} = 800 °C result shows little softening due to deformation during quenching for the 30 °C/s cooling rate condition, but considerable softening for the two lower cooling rates. The level of softening due to deformation at T_{DEF} = 600 °C is significant for all three cooling rates.

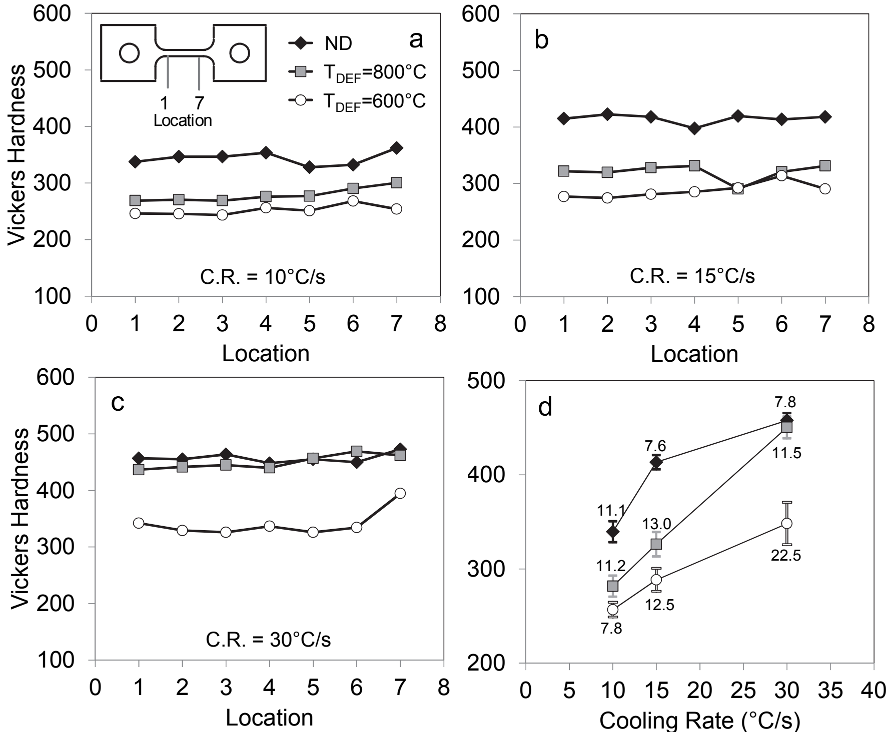

Figure 5 - Measured Vickers hardness distributions within the gauge length of the thermal-mechanically processed specimens at (a) 10 °C/s (b) 15 °C/s and (c) 30 °C/s. (d) Vickers hardness versus cooling rate. The error bars indicate +/- the standard deviation as measured from the population of repeat measurements and the values adjacent to the data points indicate the calculated standard deviation. (ND = no deformation).

3.3 Effect of Quench Conditions on Area Fraction of Phases

The micrographs used to quantify the area fraction of martensite, bainite and ferrite for the 30 °C/s, 15 °C/s and 10 °C/s quench rate conditions are shown in Figure 6, Figure 7 and Figure 8, respectively. The SEM images provide a detailed view of the mixed microstructures for each condition while the color tint-etched optical micrographs were used to generate the post-processed images for which a pixel count was conducted and the area fractions quantified. For each condition, the micrographs are shown at the same scale for comparison, but do not correspond to the same image. Table 2 summarizes the average measured area fractions for all of the quench rate conditions and Figure 9 plots the average area fractions of martensite, bainite and ferrite as a function of deformation condition.

The specimen quenched at 30 °C/s with no deformation (ND) revealed a predominantly martensitic microstructure as would be expected based on the high hardness of 458 HV. The ND SEM micrograph in Figure 6a exhibits packets of parallel lath crystals that are characteristic of martensite containing less than 0.6% carbon [26]. Bainite was also found within the microstructure as shown by the characteristic carbides that are oriented along a common direction and dispersed throughout the sheaves of a bainitic ferrite matrix. These morphological characteristics are typically used to describe upper bainite [27], but have also been used to describe lath-like bainitic structures [28] and conventional bainite structure as well [16,17]. A very small area fraction of ferrite is also distinguishable as the flat and featureless constituent in the SEM micrograph. Ferrite is not expected for this cooling rate condition and may have formed due to a small tensile pre-load on the blank as the specimen thermally contracted during quenching. The colour tint-etching procedure resulted in an optical micrograph that revealed martensite as brown or straw colour, bainite as blue/black and ferrite as white as shown in Figure 6a. Plastically deforming the specimen at T_{DEF} = 800 °C during the 30 °C/s quench resulted in a small reduction in hardness which was due to an increased area fraction of bainite when compared to the ND case as shown in Figure 6b. The bainitic structure in this case was similar to that observed for the ND case. The T_{DEF} = 600 °C case resulted in the transformation of bainite with a structure characterized by a relatively coarse constituent dispersed throughout a ferritic matrix as shown in the SEM micrograph in Figure 6c. This bainitic structure is consistent with that of granular bainite which is characterized by either martensite, retained austenite or martensite/retained austenite islands dispersed within a ferritic matrix [15,27,29-31]. It is widely accepted that the morphology of bainite transitions from an upper bainite type morphology to a granular type morphology as the continuous cooling rate is decreased [29,30,32] as shown by the schematic CCT diagram in Figure 4c. This phenomenon can be used to explain the formation of granular bainite in the current study, which is illustrated by Figure 4d. The addition of plastic deformation during quenching shifts of the CCT diagram towards the left, or lower transformation times. This in effect, is similar to reducing the cooling rate, since a constant cooling rate of 15 °C/s plotted on a conventional CCT diagram would appear further to the right of the bainite window when plotted on a CCT diagram that has been shifted towards the left. Barcellona and Palmeri [15] also observed granular bainite in their as-quenched microstructure of quenched and deformed

22MnB5 boron steel, which is identical to the USIBOR® 1500P boron steel used in this study. Min et al. [16] also observed this type of bainitic structure, but referred to it as acicular ferrite. The characteristic martensite structure is also present with islands of ferrite dispersed throughout. Based on the colour tint-etched optical micrograph in Figure 6c, it appears that ferrite (white) is a dominant constituent. This would be a false assumption because the ferritic matrix within the bainite appears white and should not be counted as purely ferrite. This fact must be taken into account when selecting the bainite and ferrite phases during post-processing to quantify area fractions using an image analysis software.

The 15 °C/s quench specimens are shown in Figure 7 and the ND condition shows a mixed martensite/bainite structure with a small area fraction of ferrite. The bainite appears as islands throughout the mostly martensitic microstructure and consists of an upper bainite-type morphology. For the T_{DEF} = 800 °C deformation condition, the dominant structure is granular bainite and martensite appears as small irregularly shaped islands throughout, while ferrite is observed as large islands throughout the microstructure. When compared to the T_{DEF} = 800 °C condition, a more refined ferritic microstructure is observed for the T_{DEF} = 600 °C condition and granular bainite is the dominant structure. The more refined ferritic structure observed in the optical micrograph (Figure 7d), which was used to quantify the area fractions, may have contributed to a measured area fraction of 12%, which is lower than the measured area fraction of 18% for the T_{DEF} = 800 °C condition.

At a quench rate of 10 °C/s, the effect of deformation has a minimal role on the volume fraction of bainite that is transformed, but increases the area fraction of ferrite and decreases the area fraction martensite by nearly equal proportions. Although the area fraction of bainite changes little as the temperature during deformation changes, the morphology of bainite changes from the upper bainite-like structure for the ND condition, to granular bainite for the two deformation conditions. The structure of martensite also becomes irregular and dispersed throughout the microstructure for the two deformation conditions.

Figure 9 shows the effect of deformation during quenching on the measured area fraction of martensite, bainite and ferrite for the three different quench rates and deformation temperatures. For the 30 °C/s and 15 °C/s quench rate conditions, the results indicate decreasing martensitic area fractions and increasing area fractions of bainite and ferrite as the deformation condition changes from ND to T_{DEF} = 600 °C. At 10 °C/s, the area fraction of bainite remains almost unchanged for the three deformation conditions examined and the decrease in martensite is offset by the increase in ferrite as the deformation condition changes from ND to T_{DEF} = 600 °C.

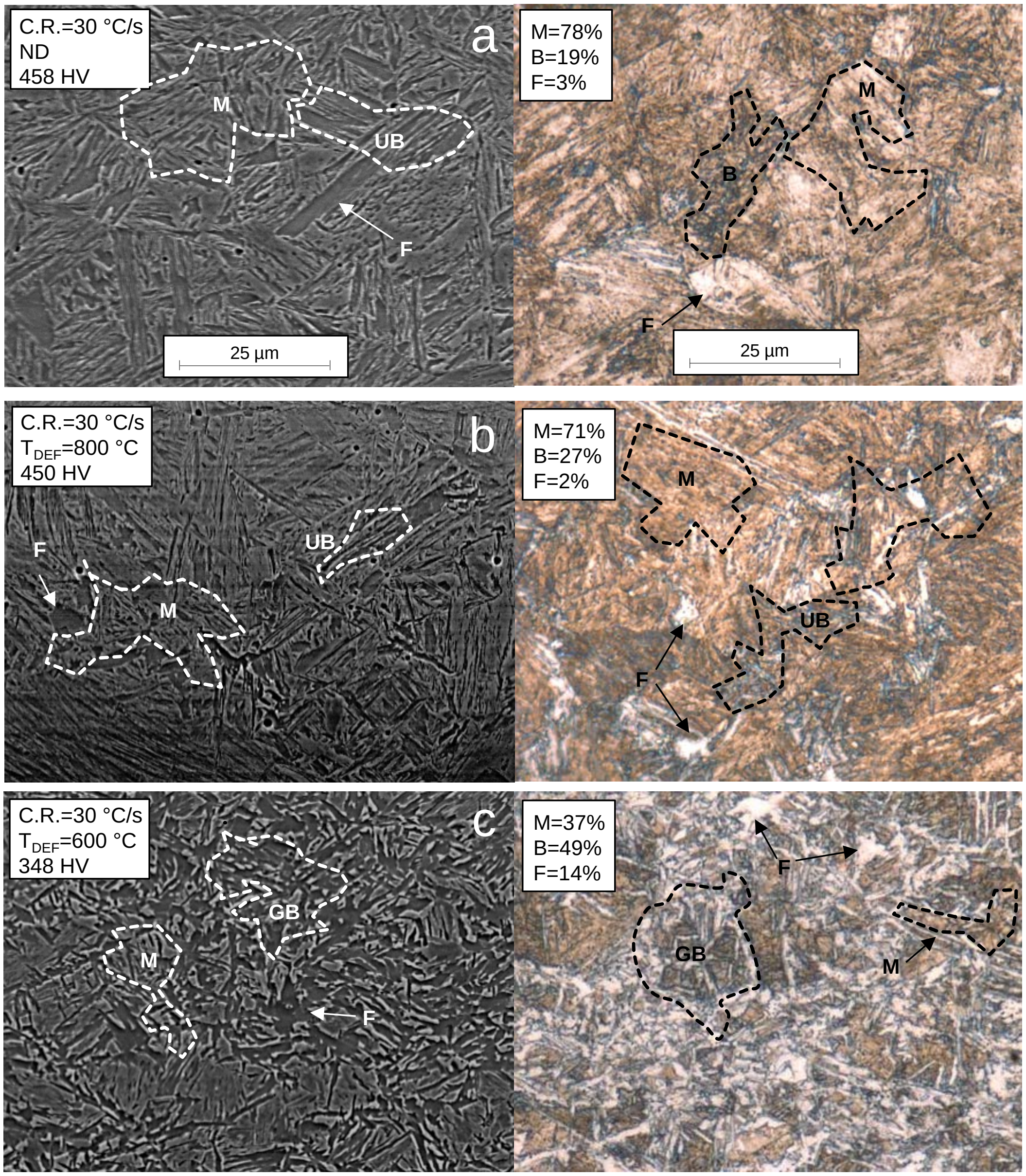

Figure 6 - The SEM micrographs and color tint-etched optical micrographs for the specimens quenched and deformed at 30 °C/s.

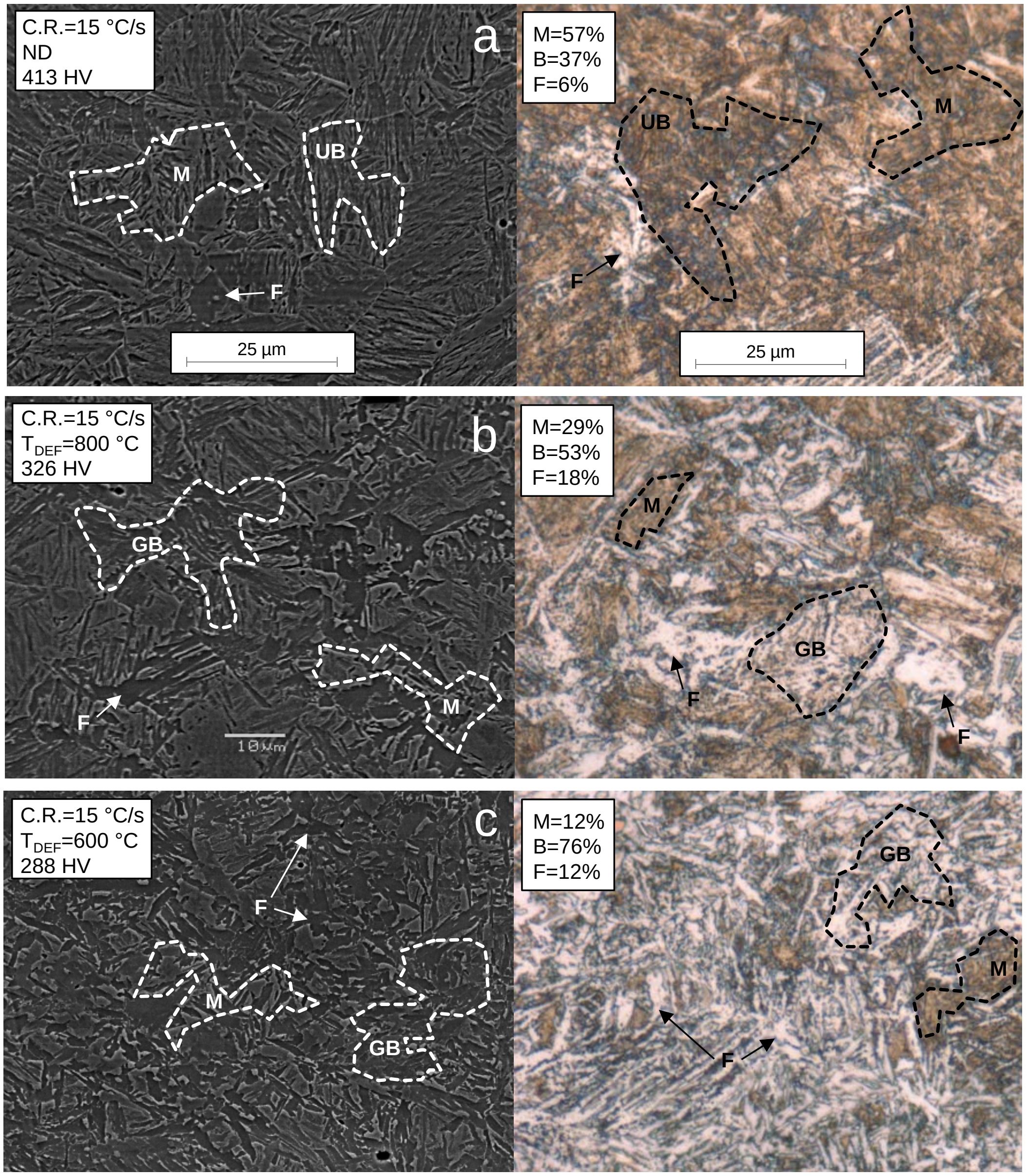

Figure 7 – The SEM micrographs and color tint-etched optical micrographs for the specimens quenched and deformed at 15 °C/s.

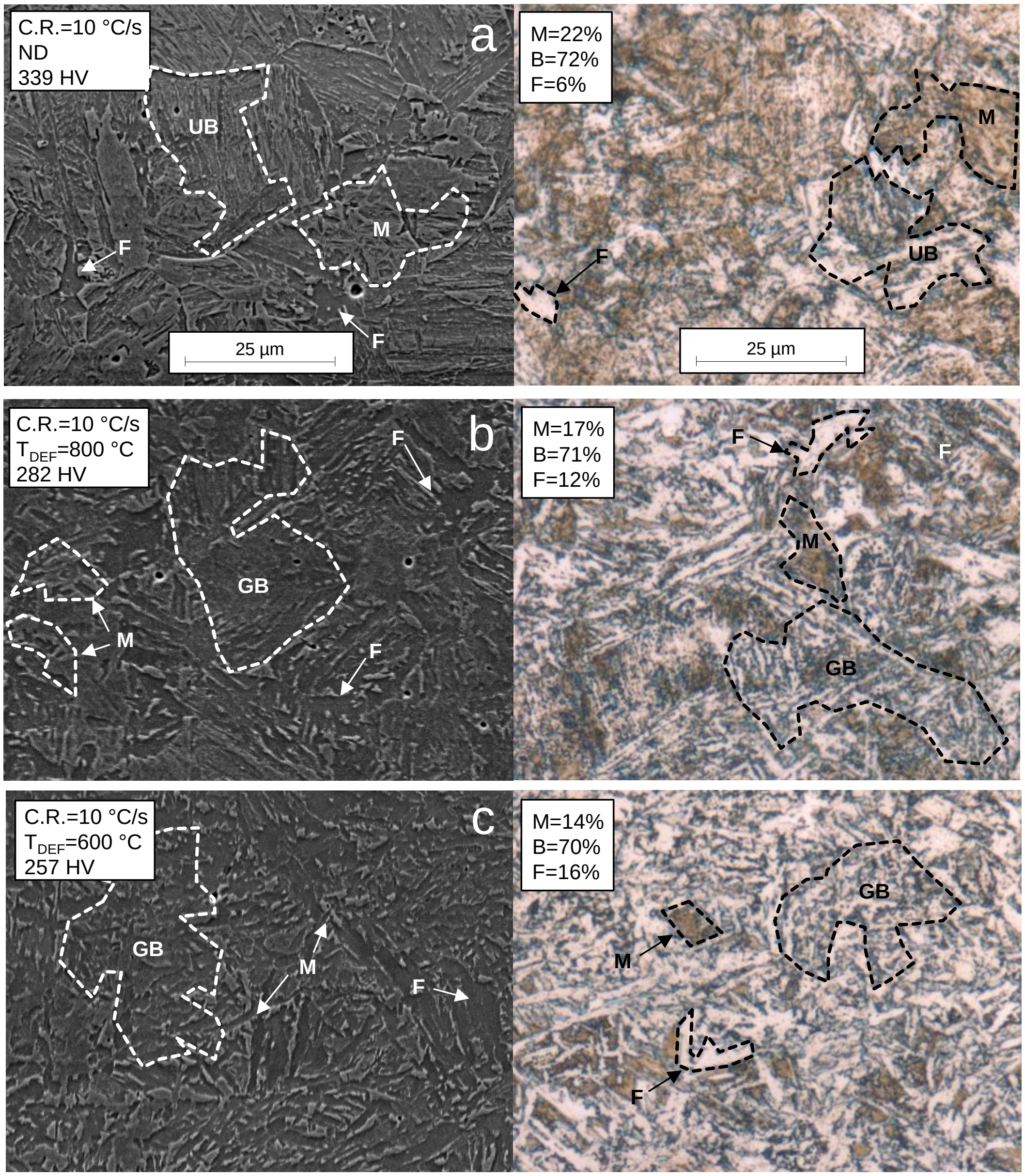

Figure 8 - The SEM micrographs and color tint-etched optical micrographs for the specimens quenched and deformed at 10 °C/s.

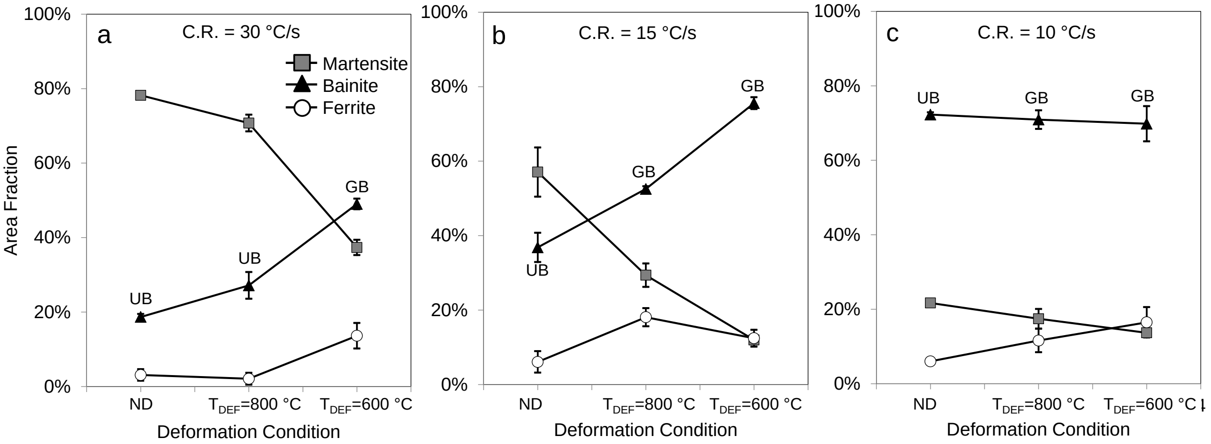

Figure 9 - The average measured area fraction of martensite, bainite and ferrite for all of the quenching and deformation conditions. The error bars indicate +/- the standard deviation as measured from the population of repeat measurement results (3 micrographs used per condition). GB-granular bainite, UB-upper bainite like morphology.

Table 2 - Summary of the area fraction measurements. For each condition, three different micrographs were used and the standard deviation for each condition is shown by the error bars in Figure 9.

Cooling Rate (°C/s)	T_{DEF} (°C)	Avg. Vickers Hardness	Avg. Area Fraction Mart., M (%)	Avg. Area Fraction Bainite, B (%)	Avg. Area Fraction Ferrite, F (%)	Mart.-Bain. Area Fraction Relationship, M/(M+B) (%)
10	ND	339	22	72	6	23
	800	282	17	71	12	20
	600	257	14	70	16	16
15	ND	413	57	37	6	61
	800	326	53	29	18	64
	600	288	12	76	12	14
30	ND	458	78	19	3	81
	800	450	71	27	2	72
	600	348	37	49	14	43

3.4 Measured Mechanical Behavior

Stress-Strain Analysis of Quasi-Static Results - The average engineering stress versus strain curves from the uniaxial tension tests conducted at a strain rate of 0.003 s^{-1} are presented in Figure 10a-c and the average mechanical properties can be found in Table 3. Each of the curves represent an average of three repeat tests which showed excellent repeatability as indicated by the low scatter of the ultimate tensile strength (σ_{UTS}) and 0.2% yield strength (σ_Y) shown in Figure 11a. To calculate an average curve for each condition, the raw data set was interpolated at strain increments of 0.002 and the interpolated values were then used to create a single average curve for each condition. In addition to the simultaneously quenched and deformed tensile data generated in this work, the average engineering stress versus strain curves from [12] are shown as the dashed curves in Figure 10d for comparison to the ND condition curves. These specimens were quenched without deformation using a forced air quenching apparatus (FAQA) which resulted in as-quenched area fractions that varied from martensitic to bainitic. The area fraction of ferrite for the FAQA quenched specimens was not quantified, but was assumed to be negligible due to the absence of deformation during quenching. The average measured Vickers hardness and average area fraction (%) of ferrite present in the microstructure for each material condition are shown adjacent to the curves in Figure 10a-d.

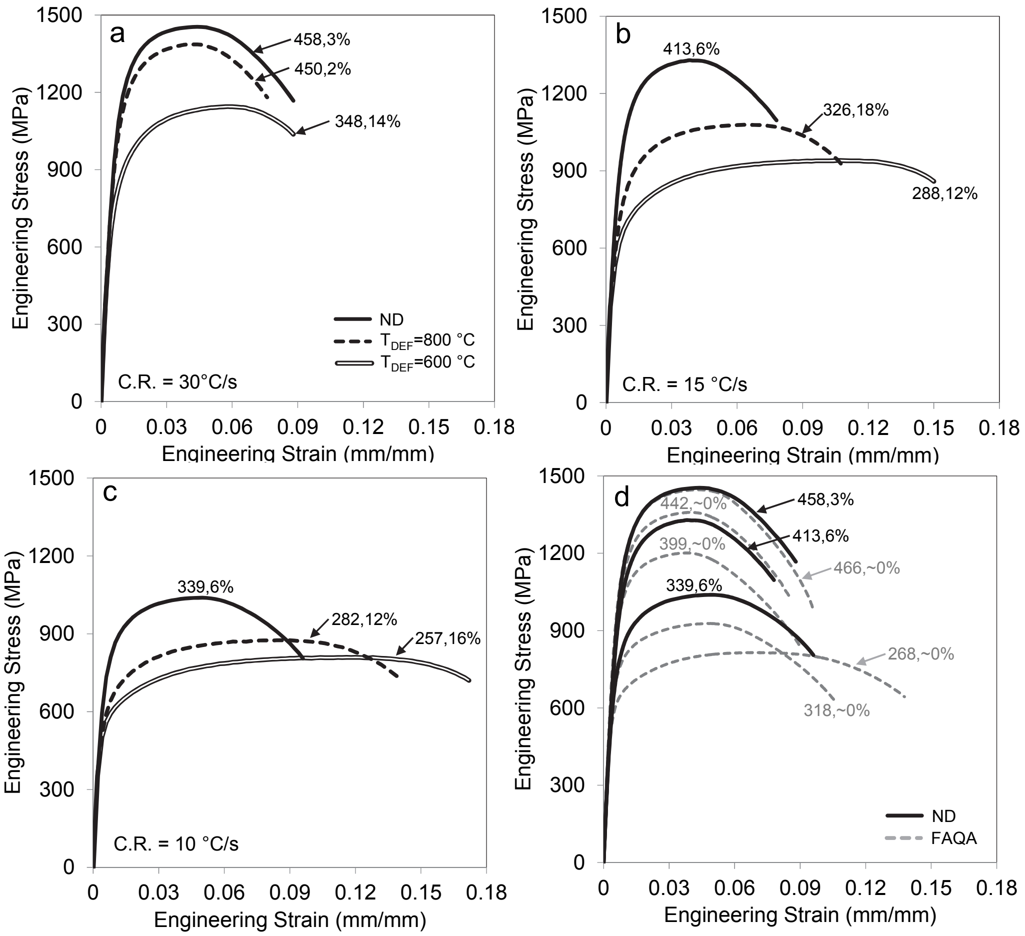

Figure 10 – Average engineering stress versus strain curves for the (a) 30 °C/s (b) 15 °C/s and (c) 10 °C/s specimens pulled at a strain rate of 0.003 s^{-1}. The numbers that correspond to each curve are the average measured Vickers hardness and the percent values represent the average measured area fraction of ferrite within the microstructure. (d) A comparison of the ND curves from a-c to the average engineering stress versus strain curves for specimens quenched in the FAQA and pulled at a strain rate of 0.003 s^{-1} [12]. The microstructure of the FAQA specimens ranges from approximately martensitic to bainitic.

The average σ_{UTS} and σ_Y for the quenched and deformed specimens is plotted as a function of the average measured Vickers hardness in Figure 11a (round data points). Both the σ_{UTS} and σ_Y data lie along linear trend lines, irrespective of quench condition or the area fraction of phases present in the microstructure. Also plotted in Figure 11a are the σ_{UTS} and σ_Y data points from the FAQA processed specimens which do not contain ferrite. With respect to the yield strength, the FAQA data lies along the same trend line as the quenched and deformed results measured in the current work for equivalent hardness levels. When compared to the

FAQA data, the ultimate tensile strength measured for the quenched and deformed specimens was slightly elevated for an equivalent hardness level. This is shown by the two trend lines that were fit to both data sets as labeled in Figure 11a. The trend line of the quenched and deformed material conditions, which containing ferrite, is offset (vertically) by approximately 60 MPa when compared to the FAQA trend line.

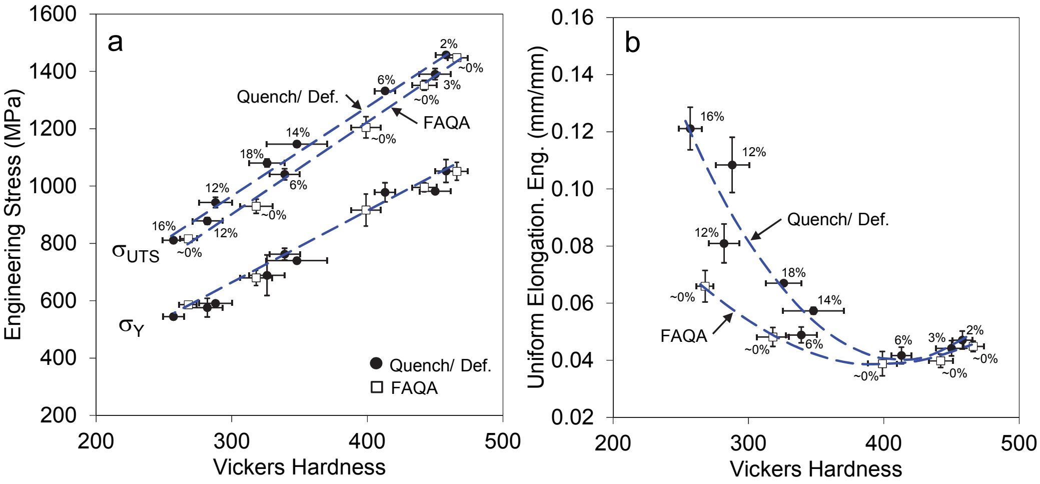

Figure 11 - (a) The measured ultimate tensile strength (σ_{UTS}) and 0.2% yield strength (σ_Y) versus average Vickers hardness from the quasi-static tension tests conducted at a strain rate of 0.003 s^{-1} (b) The average uniform elongation versus the average measured Vickers hardness. The percent values indicate the average measured area fraction of ferrite within the microstructure. The error bars indicate +/- the standard deviation as measured from the population of repeat measurements. The FAQA results are those measured from Figure 10d and presented in [12]. The microstructure of the FAQA specimens ranges from approximately martensitic to bainitic with negligible levels of ferrite.

While a linear relationship exists between strength level and hardness for the quenched and deformed specimens, this is not the case for the strain hardening behaviour observed for the curves presented in Figure 10a-c. Qualitatively, it appears that the degree of strain hardening occurs over a larger range of strain when the area fraction of ferrite is greater than ~6%, even though the hardness and strength levels are similar. This behaviour is illustrated in Figure 12 which serves to compare the average stress versus strain curves at material conditions with similar hardness levels. For the two pairs of curves with a hardness of ~260 HV and ~330 HV, the material exhibits a larger uniform elongation strain when the amount of ferrite present within the microstructure increases. Figure 11b plots the average uniform elongation strain (engineering) for the quenched and deformed specimens (also in Table 3) and the specimens quenched in the FAQA for which it is assumed that no ferrite formed and only martensite and bainite are present within the microstructure. Polynomial trend lines were fit to the two data sets and are shown as the dashed trend lines in Figure 11b. The quenched and deformed specimens containing area fractions of ferrite greater than 6% are indicated by the ferrite area fraction values adjacent to the round data points. The two trend lines shown in Figure 11b indicate that for equivalent hardness levels less than 400 HV, the uniform elongation is greater for the quenched and deformed materials when compared to the FAQA curves. As the hardness level approaches approximately 250 HV, the difference in uniform elongation between the quenched and deformed specimens and the FAQA specimens is amplified as shown in Figure 12 for the two pairs of curves with a hardness of ~260 HV and ~330 HV.

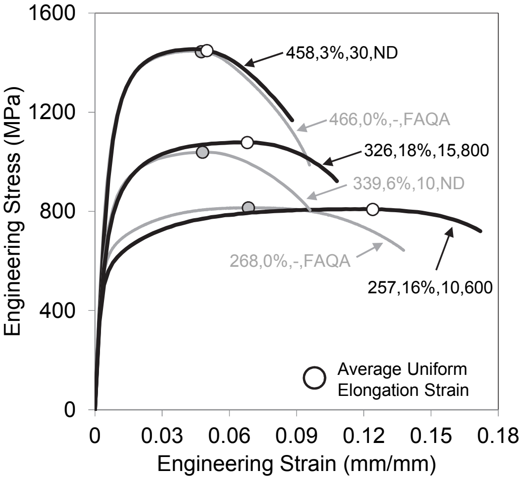

Figure 12 – The effect of area fraction of ferrite on the uniform elongation strain. Shown for a variety of as-quenched material conditions. Average engineering stress versus strain curves for a variety of as-quenched material conditions tested in this work and from the FAQA experiments [12]. The tensile tests were conducted at a strain rate of 0.003 s^{-1} and the label corresponding to each curve indicates: [avg. Vickers hardness, avg. measured area fraction of ferrite, cooling rate, deformation condition].

The slightly elevated ultimate tensile strength and increased uniform elongation for a given hardness level leads to an increase in the energy absorption potential of the quenched and deformed material conditions. To illustrate the increased energy absorption, Figure 13a is a plot of the toughness for each material condition. For each individual repeat test, the toughness was calculated as the area under the engineering stress versus strain curve. The toughness data points plotted in Figure 13a are the average calculated based on the population of repeat tests. A polynomial trend line was fit the data set and shows an improvement in energy absorption as the toughness increases from 127.3 MJ/m^3 at a hardness of 458 HV with 2% ferrite to 144.2 MJ/m^3 at a hardness of 257 HV with 16% ferrite. This increase in toughness represents a 13% increase in energy absorption potential. The calculated toughness is also plotted for the FAQA materials that are void of ferrite and the results show that the toughness decreased from 126.0 MJ/m^3 at a hardness of 466 HV to 113.0 MJ/m^3 at a hardness of 268 HV. Although a 10% reduction in energy absorption is observed as the microstructure transitions from martensitic to bainitic, the benefits of the improved ductility (uniform elongation strain) for the bainitic material condition may offset the relatively small reduction in energy absorption. At the lowest hardness condition for which the main constituent is bainite, the quenched and deformed specimen containing 16% ferrite with a hardness of 257 HV resulted in a 28% increase in toughness when compared to the FAQA specimen that did not contain ferrite and had a hardness of 268 HV. For both the quenched and deformed and FAQA specimen toughness distributions shown in Figure 13a, the lowest toughness values occur at approximately 375 HV and increase as the hardness increases. This trend is due to the small increase in uniform elongation strain as the hardness increases from approximately 375 HV as shown in Figure 11b. This observation is unexpected since these material conditions have minimal to no ferrite and increasing volume fractions of martensite as the hardness increases from approximately 375 HV to 460 HV. This phenomenon may be due to the shape effect of the bainite islands as the volume fraction of bainite diminishes for increasing hardness levels. From a structural component design perspective, the toughness distribution shown in Figure 13a indicates that tailored hot stampings with as-quenched hardness levels ranging from approximately 300 HV to 425 HV may be undesirable due to their reduced energy absorption capacity. Although toughness is typically measured up to the point of fracture, some may consider the onset of necking (uniform elongation strain) as the point where material failure initiates. Figure 13b is a plot of the toughness, which was calculated up to the uniform elongation strain rather than fracture. The trend lines plotted in Figure 13b indicate that the reduction in energy absorption capacity for hardness ranging from approximately 300 HV to 425 HV is less severe than presented in Figure 13a. At the lowest hardness condition, the quenched and deformed material containing 16% ferrite had a toughness of 88.7 MJ/m^3 at a hardness of 257 HV, while the toughness of the FAQA specimen, which is void of ferrite, is 54.9 MJ/m^3 at a hardness of 268 HV. This increase in toughness, due to the addition of ferrite, resulted in a 62% increase in energy absorbing capacity. For the highest hardness condition (~ 460 HV), the toughness was approximately 60 MJ/m^3 for the quenched and deformed and the FAQA specimens.

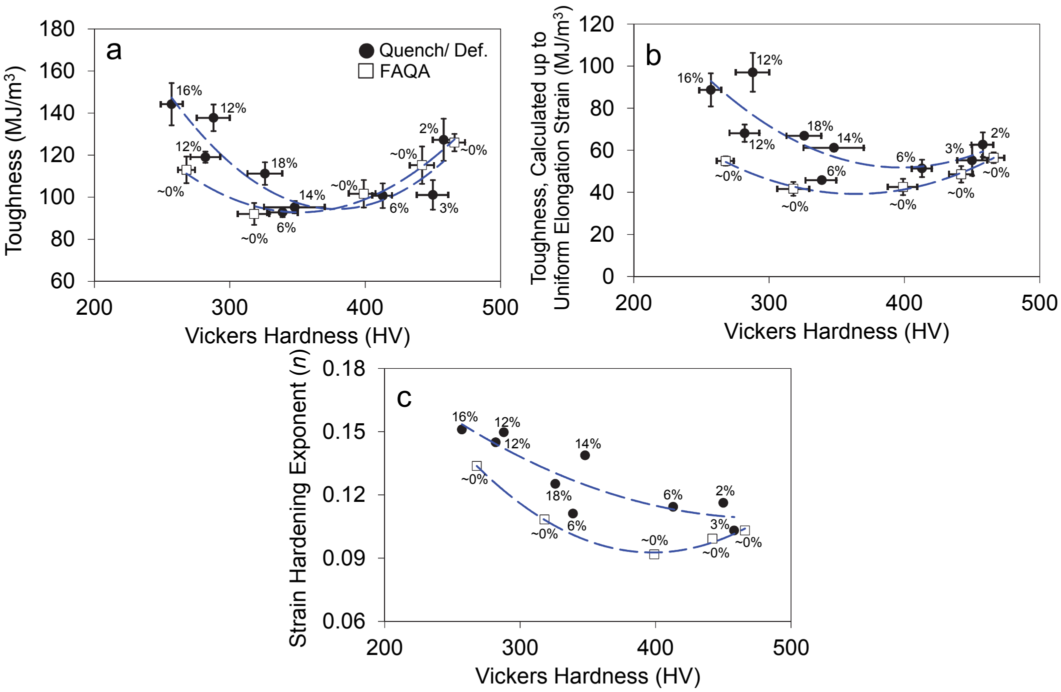

Figure 13 – (a) Toughness (or energy absorption) versus Vickers hardness for the quenched and deformed specimens (b) Toughness (or energy absorption) up to the uniform elongation strain versus Vickers hardness for the quenched and deformed specimens (c) The strain hardening exponent versus the Vickers hardness for the quenched and deformed specimens. Also included in (a) and (b) is the data for the specimens quenched in the FAQA, from [12]. The percent values indicate the average measured area fraction of ferrite within the microstructure and the error bars indicate +/- the standard deviation as measured from the population of repeat measurements.

Strain Hardening Rates - The strain hardening behaviour for all of the average curves presented in Figure 10 was quantified by converting the engineering stress versus strain data into true stress versus strain and fitting the curves with the power law function due to Hollomon [33],

$$\sigma = K\varepsilon^{n} \tag{1}$$

where K is the strength coefficient (MPa) and n is the strain-hardening exponent that is also referred to as the n-value. The n-value provides an empirical parameter used to rank the stretch formability of similar metallic systems and is useful for estimating the true strain at the onset of necking in a uniaxial tension test [34,35]. Materials that are characterized by high n-values strain harden more, than similar materials with low n-values. The average engineering stress versus strain curves were converted into true stress versus strain for each test condition and fit with equation 1 from a strain level of 0.016 up to the limit of uniform elongation. This portion of each curve was selected because changes occur in the n-value at low strains for most metals and in particular for martensitic steels [36,37]. The K, n-value and R-squared fitting parameters are presented in Table 3 and the n-values are plotted versus the Vickers hardness in Figure 13c. A trend line was fit to the data and clearly shows that the n-value increases from ~0.10 at the highest hardness levels to ~0.15 at the lowest hardness levels which indicates increased ductility and an increase in strain hardening as the material hardness (or strength) reduces. The n-value was also captured and plotted in Figure 13c for the specimens quenched in the FAQA where no ferrite was present. A trend line was also fit to this data, which clearly indicates that the presence of ferrite increases the n-value and strain hardening behaviour of the materials for equivalent hardness (or strength) levels.

Effect of Strain Rate on Mechanical Properties – For the intermediate strain rate tests, two repeat tests were conducted for the no deformation (ND) conditions and three repeat tests were conducted for the remainder of the conditions. The average ultimate tensile strength (σ_{UTS}) and 0.2% yield strength (σ_{Y}) for both strain rates can be found in Table 3 and are plotted in

Figure 14a. The tests showed excellent repeatability as indicated by the low scatter of the σ_{UTS} and σ_Y shown in Figure 14a. Figure 14b is a plot of the average σ_{UTS} versus the average true strain rate and shows moderate strain rate sensitivity for the majority of the conditions tested.

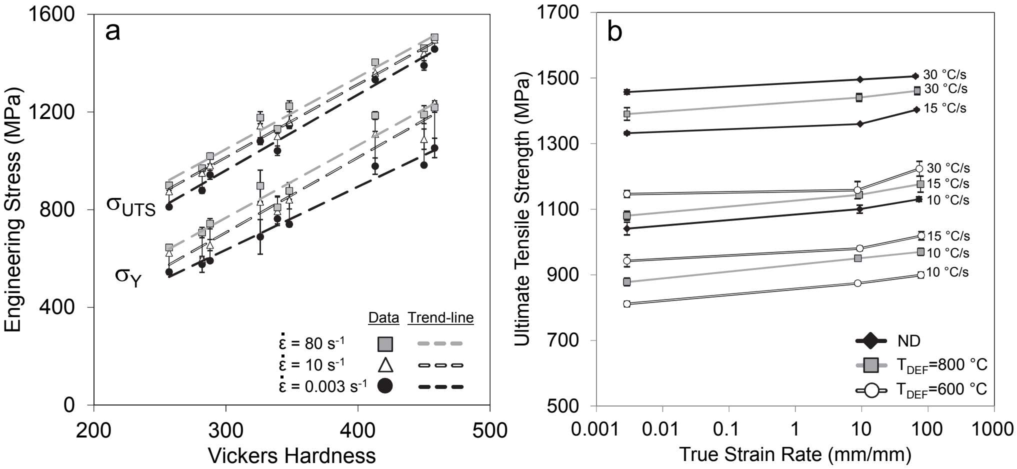

Figure 14 – (a) The ultimate tensile strength (σ_{UTS}) for and 0.2% yield strength (σ_Y) versus Vickers hardness for all of the quenched and deformed specimens tested at nominal strain rates of 0.003 s^{-1}, 10 s^{-1} and 80 s^{-1} (b) The effect of strain rate on σ_{UTS}. The error bars indicate +/- the standard deviation as measured from the population of repeat measurements.

Figure 15 is plot of the average increase in ultimate tensile strength ($\Delta\sigma_{UTS}$) for an increase in strain rate from 0.003 s^{-1} to 80 s^{-1} as a function of the Vickers hardness. The average $\Delta\sigma_{UTS}$ for the quenched and deformed specimens is ~80 MPa. Also plotted in Figure 15 is the $\Delta\sigma_{UTS}$ (between 0.003 s^{-1} to 85 s^{-1}) for the specimens quenched in the FAQA, from [12]. A trend line was fit to all of the data shown in Figure 15 and the general trend indicates slightly elevated strain rate sensitivity for the softer and lower strength material condition, as suggested in the initial work on tailored properties by Bardelcik et al. [25]. The percent values adjacent to the data points in Figure 15 are the average measured area fraction of ferrite within the microstructures of each material condition. There does not appear to be a correlation between the value of $\Delta\sigma_{UTS}$ and the presence of ferrite in the as-quenched material condition; therefore the increased strain rate sensitivity is thought to be solely a function of material strength.

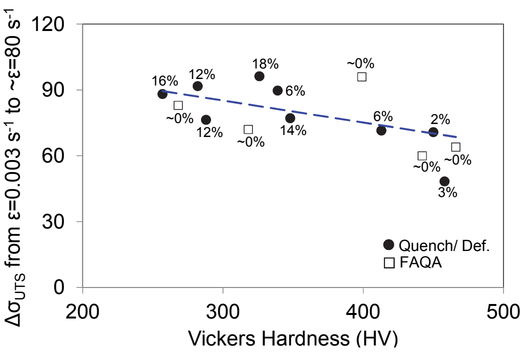

Figure 15 - The change in average ultimate tensile strength ($\Delta\sigma_{UTS}$) due to a nominal strain rate increase from 0.003 s^{-1} to 80 s^{-1} versus the Vickers hardness for the quenched and deformed specimens. Also shown are the results for the FAQA specimens [12], where the change in ultimate tensile strength ($\Delta\sigma_{UTS}$) due to an average true strain rate increase from 0.003 s^{-1} to 85 s^{-1} is plotted. The percent values indicate the average measured area fraction of ferrite within the microstructure.

All of the measured engineering stress versus strain curves were converted into true stress versus effective plastic strain (or flow stress) curves. For each individual repeat test, the effective plastic strain was calculated using an "effective modulus" (see [12]) which was extracted from the raw engineering stress versus strain data. To calculate an average curve for each condition, the raw data set was interpolated at strain increments of 0.002 strain and the interpolated curves were then used to create a single average curve for each condition corresponding to the data points in Figure 16. For all of the quench rate conditions, the strain rate sensitivity is clearly shown by a scaling of the flow stress curves to higher stress levels at the higher strain rate conditions. The yield point for each material condition shown in Figure 16 appears to be scaled up for increasing strain rates. This effect of strain rate on yield point observation is also shown in Figure 14a, which suggests that a multiplicative term can be used within a constitutive model to capture the strain rate sensitivity. Figure 17a-c are plots of the true stress (data points) at an effective plastic strain of 0.03 versus the true strain rate. Similar to the effect of strain rate on σ_{UTS} , the rate dependence of the true stress in Figure 17a-c is moderate when the loading rate increases from 0.003 s^{-1} to 80 s^{-1} as indicated by an average change in flow stress of approximately 76 MPa for all of the conditions.

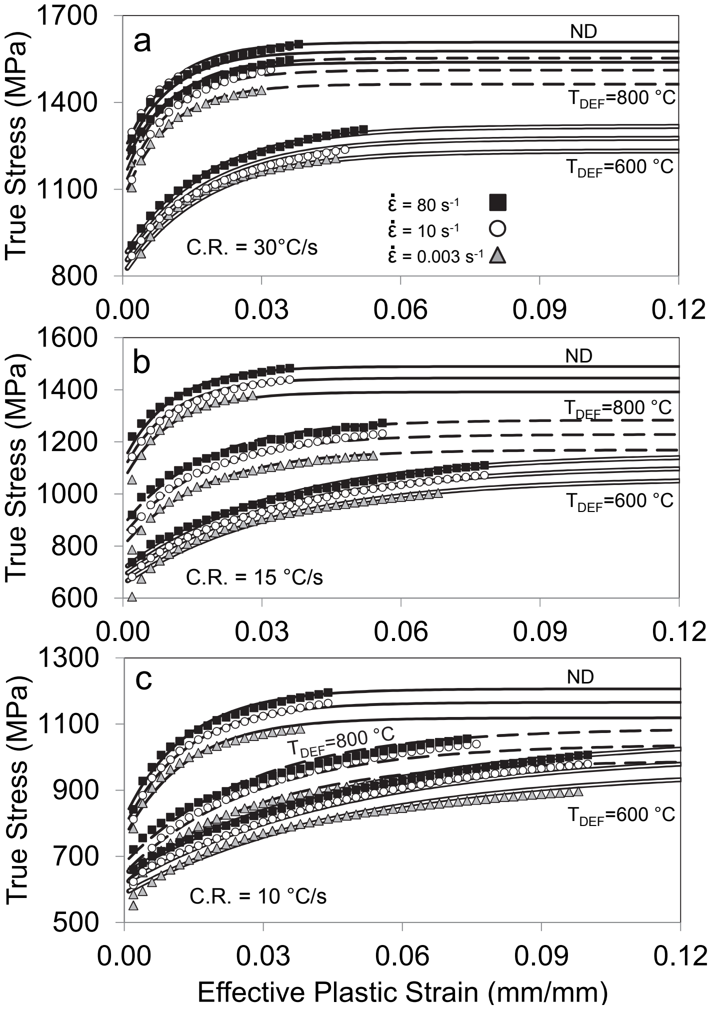

Figure 16 - The average measured flow stress curves for the specimens quenched at (a) 30 °C/s (b) 15 °C/s (c) 10 °C/s. The data points represent the measured flow stress data and the continuous curves represent the predicted flow stress due to equation 2 (see Section 4) for each quenched and deformed condition.

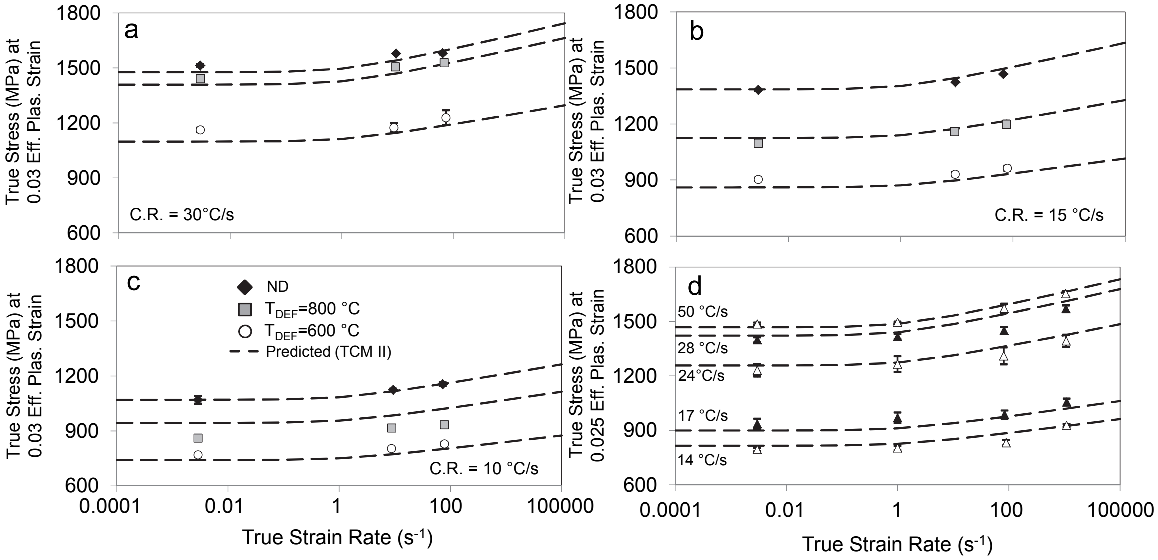

Figure 17 - The true stress versus true strain rate for the specimens quenched at (a) 30 °C/s (b) 15 °C/s (c) 10 °C/s. (d) The true stress versus true strain rate for the specimens quenched in the FAQA, from [12]. The data points represent the measured true stress data and the dashed curves represent the predicted true stress due to the TCM II model (see Section 4). The error bars indicate +/- the standard deviation as measured from the population of repeat measurements.

Table 3 - Tensile properties of the simultaneously quenched and deformed specimens.

Cooling Rate (°C/s)	T_{DEF} (°C)	Avg. Vickers Hardness	Avg. True Strain Rate (s^{-1})	Avg. UTS (MPa)	Avg. Yield Str., 0.2% (MPa)	Avg. Uni. El. Strain (mm/mm)	Avg. Toughness, (MJ/m^3)	Strength Coeff., *K* (MPa)	*n*-Value	R^2 Value
10	ND	339	0.003	1041	736	0.049	92.8	1542.9	0.111	0.99
			9.4	1100	794	-	-	-	-	-
			73.0	1130	809	-	-	-	-	-
	800	282	0.003	878	576	0.081	119.0	1388.2	0.145	0.99
			8.8	950	598	-	-	-	-	-
			77.6	970	706	-	-	-	-	-
	600	257	0.003	811	545	0.121	144.2	1273.5	0.116	0.98
			8.7	874	623	-	-	-	-	-
			78.0	899	645	-	-	-	-	-
15	ND	413	0.003	1332	978	0.042	100.7	2021.7	0.114	0.98
			9.5	1360	1110	-	-	-	-	-
			67.4	1403	1185	-	-	-	-	-
	800	326	0.003	1080	689	0.067	111.2	1641.5	0.125	0.98
			9.1	1144	836	-	-	-	-	-
			76.9	1176	897	-	-	-	-	-
	600	288	0.003	943	591	0.108	137.7	1482.5	0.150	0.99
			9.4	980	655	-	-	-	-	-
			79.4	1019	742	-	-	-	-	-
30	ND	458	0.003	1457	1052	0.047	127.3	2178.2	0.103	0.97
			9.5	1495	1237	-	-	-	-	-
			64.6	1506	1218	-	-	-	-	-
	800	450	0.003	1390	982	0.044	101.1	2113.8	0.116	0.98
			9.1	1440	1088	-	-	-	-	-
			68.9	1461	1189	-	-	-	-	-
	600	348	0.003	1146	740	0.057	95.2	1827.6	0.139	0.98
			8.6	1158	840	-	-	-	-	-
			73.8	1223	877	-	-	-	-	-

4 Constitutive Model Development

The Taylor model [38] forms the basis of many physically based constitutive models (such as the Bergstrom model [39]) which are capable of capturing the constitutive response of crystalline materials by mathematically expressing the competitive interaction of dislocation storage and annihilation. Fitting the results of the current work to the Bergstrom model was initially considered in an attempt to understand the role of dislocation dynamics on the constitutive behaviour of these multiphase materials, but due to the complexity of the of martensitic and bainitic phases, which themselves behave as composite structures, this approach was deemed intractable at present. Considering the complexity of the multiphase material conditions examined in this work, it was deemed that a phenomenological approach to characterizing the constitutive response would be taken.

In previous work, Bardelcik et al. [12] developed the strain rate sensitive Tailored Crash Model (TCM) for quenched boron steel with tailored properties. The model is phenomenological and the material conditions that were used to develop the TCM varied from martensitic to bainitic. Due to the variation in strain hardening rate between these material conditions, it was found that the Voce [40] hardening model with a multiplicative strain rate sensitive term in the form of an exponential type function was able to capture the change in hardening rate better than other strain rate sensitive constitutive models such as Johnson-Cook [41,42] and Zerilli-Armstrong [43], for example. The maximum temperature rise due to adiabatic heating for tests conducted at a strain rate of ~1075 s^{-1} was minimal at 18 °C and therefore thermal softening was not accounted for in the model. The Voce hardening model with the exponential-type strain rate sensitivity term is shown in equation 2 where constant A is the saturation stress, B is the initial yield stress, C is the relaxation strain and D is the strain rate coefficient.

$$\sigma = \left[A + \left[[B - A]e^{\left(-\frac{\varepsilon}{C}\right)}\right]\right][1 + \dot{\varepsilon}]^{D} \qquad [2]$$

The TCM was developed by fitting equation 2 to the various as-quenched material conditions from the FAQA [12]. The Voce constants were then plotted with respect to Vickers hardness for each of the five material conditions, which revealed that constants A and B varied linearly with respect to hardness and constant C varied in a polynomial manner with respect to hardness. The strain rate coefficient did not vary significantly and was taken to be a constant. Although the TCM was developed as a function of as-quenched Vickers hardness, the model could also be expressed as a function of martensite/bainite area fraction due to the linear relationship between hardness and area fraction martensite/bainite [12].

In the current work (Section 3.4), it has been shown that the Vickers hardness and strength levels can be similar for an as-quenched microstructure composed of bainite/martensite and bainite/martensite/ferrite, but significant differences in hardening rate occur depending upon the level of ferrite present in the as-quenched microstructure. This effect of ferrite on the hardening rate has motivated the development of a new model, presented herein and referred to as the “Tailored Crash Model II” (TCM II) constitutive model, which is a function of effective plastic strain, true strain rate and area fraction of martensite, bainite and ferrite. The following three sections (4.1 to 4.3) lay out the steps undertaken to develop the TCM II: (i) for each material condition, fit equation 2 to the flow stress data; (ii) mathematically relate the equation 2 constants for each material condition to area fraction martensite, bainite and ferrite; and, (iii) construct and verify the TCM II. This approach is similar to the one taken to develop the TCM in [12].

4.1 Fitting of Flow Stress Data with Rate-Sensitive Voce Hardening Model

The Voce hardening model with the exponential-type strain rate sensitivity term shown in equation 2 was fit to the average measured flow stress curves (from 0.003 s^{-1} to 80 s^{-1}) for each of the quenched and deformed conditions shown in Figure 16. A non-linear regression analysis was conducted to fit the model using the statistical analysis software MYSTAT 12. Table 4 presents the model parameters determined from the regression analysis for each material condition and Figure 16 plots the predicted flow stress curves using those constants. Examination of the predicted curves reveals that equation 2 was able to fit the measured data very well for all of the strain rates considered. The goodness of fit, indicated by the high R-squared values in Table 4 confirms the excellent fit of equation 2 to each material condition.

4.2 Effect of Martensite, Bainite and Ferrite on the Voce Model Parameters

In order to introduce the dependency of the strain rate sensitive Voce model parameters on the phases present after thermo-mechanical processing, the following approach was taken. There are three potential phases present, of which the volume fraction of any two can be regarded as independent variables. For the first independent variable, the martensite – bainite area fraction relationship, which is calculated as the ratio of area fraction martensite to the total area fraction of martensite plus bainite $[M/(M+B)]$ was adopted and is shown in Table 2 for all of the conditions tested in this work. This parameter was adopted since it allows one-to-one comparison with the TCM model for cases in which no ferrite is formed (no deformation during quenching). The second independent parameter adopted was the volume (area) fraction of ferrite (F) formed after processing.

By simply fitting the A, B and C Voce parameters (Table 4) with respect to the [$M/(M+B)$] independent variable (Table 2) for each material condition, there was no clear mathematical relationship that could be implemented within a new model, hence the introduction of the area fraction ferrite (F) was considered since it was shown to play a significant role in the hardening behaviour of these steels. It was found that a three-dimensional surface function was able to capture the Voce model parameters with respect to [$M/(M+B)$] and F. The regression tool within MATLAB 2012a was used to fit the Voce model parameters presented in Table 4, along with the Voce parameters determined in [12] for the FAQA experiments. The [$M/(M+B)$] and F values used in the fitting procedure can be found in Table 2 for the quenched and deformed materials and in [12] for the FAQA values. The polynomial surface function shown in equation 3 was used to fit the A, B and C parameters with respect to [$M/(M+B)$] and F.

$$f\left(\left[\frac{M}{M+B}\right], F\right) = \beta_1 + \beta_2 \cdot \left[\frac{M}{M+B}\right] + \beta_3 \cdot F + \beta_4 \cdot \left[\frac{M}{M+B}\right]^2 + \beta_5 \cdot \left[\frac{M}{M+B}\right] \cdot F + \beta_6 \cdot F^2 \qquad (3)$$

The surface function constants that were determined from the regression analysis are shown in Table 5 for each of the constants. As an indication of the goodness of fit, the R-squared values from the regression analysis are shown in Table 5 and indicate good agreement between the surfaces and data points. The surface function for the saturation stress (A) and yield stress (B) are plotted in Figure 18a and b, respectively. The shape of the surface indicates the expected increase in A and B for greater [$M/(M+B)$]. The concavity of these two surfaces for increasing area fractions of ferrite indicate a slight strengthening effect for area fractions of ferrite from 0 to ~10% and then a decrease in A and B for area fractions of ferrite from ~10% to 20%. Since the saturation stress (A) and ultimate tensile strength (σ_{UTS}) are directly related, the observed increase in σ_{UTS} due to the presence of ferrite (Figure 11a) agrees with the strengthening effect, but the strengthening effect of the yield strength (σ_Y) cannot be explained and may be a numerical artifact of the non-linear regression analysis conducted in section 4.1. The relaxation strain (C) surface plot shown in Figure 18c fits the data points very well and provides some insight into the effect of area fraction of ferrite on the strain hardening behaviour of the multiphase steel examined in this work. Because C is directly related to the strain hardening rate of a material (high C → high n-value), Figure 18c accurately reproduces the findings from [12] for a martensitic/bainitic material (zero F) condition. The addition of ferrite for low [$M/(M+B)$] (or predominantly bainitic) conditions increases C rapidly which indicates an increase in uniform elongation strain as observed in the experiments. For high [$M/(M+B)$] conditions the effect of area fraction of ferrite is less significant since the strain hardening behaviour of these materials appears to be dominated by the high area fractions of martensite present.

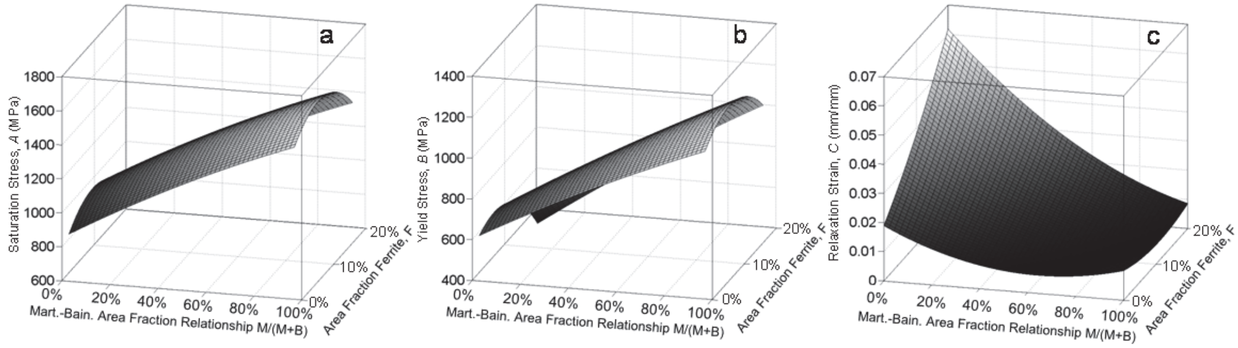

Figure 18 - The three-dimensional surface function plots for the Voce model parameters (a) A (b) B (c) C.

4.3 Tailored Crash Model II (TCM II)

The final step in developing the new "Tailored Crash Model II" (TCM II) requires the constant Voce constitutive model parameters (A, B, C, D) in equation 2 to be replaced by the functions that defined these parameters as per equation 3 and Table 5. TCM II now becomes a function of effective plastic strain (ε), true strain rate ($\dot{\varepsilon}$), martensite – bainite area fraction relationship [$M/(M+B)$] and area fraction of ferrite (F) as shown by equation 4. Figure 19a-b shows the measured experimental flow stress curves and the predicted flow stress curves using the TCM II for the quenched and deformed specimens at strain rates of 0.003 s^{-1} and 80 s^{-1}, respectively. The TCM II accurately predicts the flow stress curves for the majority of the conditions and also captures the measured increase in flow stress due to the elevated loading rate. Figure 17a-c shows the predicted (TCM II) true stress at an effective plastic strain of 0.03 versus the strain rate for all of the quenched and deformed material conditions. The predicted stress values are in excellent agreement with the measured data and support the use of the exponential type strain rate sensitivity term used in the model. In order to ensure that the TCM II can also predict the flow stress curves measured from the FAQA experiments [12], the flow stress curves from that work are plotted in Figure 19c-d at strain rates of 0.003 s^{-1} and 1000 s^{-1}, respectively. Again, the TCM II accurately captures the measured flow stress curves at both of the strain rates. Figure 17d also shows excellent agreement between the predicted (TCM II) true stress at an effective plastic strain of 0.025 versus the strain rate for all of the FAQA specimens tested in [12].

It should be noted that the surface functions used to develop the TCM II were fit based on a total of 14 (quenched/deformed and FAQA data) unique combinations of area fraction ferrite (F) and martensite – bainite area fraction relationship [$M/(M+B)$]. Although the TCM II will predict the flow stress behaviour for [$M/(M+B)$] and F combinations outside those examined in this work, it has not been validated experimentally and is the focus of future work. In cases where the TCM II may be applied to predicted the flow stress behaviour of an as-quenched material condition where the area fraction of ferrite (F) is greater than 18% (the maximum measured in this study), it is recommended that F be held at a constant value of 0.18 in equation 4, in order to prevent mathematical instabilities that may arise due to the surface functions used to define the TCM II. Based on the current and previous work [14,25] on as-quenched boron steel with fully or nearly fully martensitic microstructures, it was found that the measured Vickers hardness can range from 466 HV to as high as 516 HV. With this increase in hardness, also came an increase in material strength with seemingly no to very little change in area fraction martensite which remained at ~ 100% based on the metallography techniques used to quantify the area fraction. Bardelcik et al. [25] showed that very high quench rates resulted in a more refined martensitic structure, which most likely resulted in the observed strengthening effect observed for the as-quenched martensite. Based on these finding, it is recommended that the TCM II be used for as-quenched material conditions with Vickers hardness values less than and equal to 466 HV. For as-quenched material conditions with hardness values greater than 466 HV, the original TCM model [25] should be applied (with respect to hardness) since it is capable of predicting the strengthening effect observed for high hardness martensitic material conditions.

$$\sigma = f\left(\varepsilon, \dot{\varepsilon}, [\tfrac{M}{M+B}], F\right) =$$

$$\left[A\left([\tfrac{M}{M+B}], F\right) + \left[\left[B\left([\tfrac{M}{M+B}], F\right) - A([\tfrac{M}{M+B}], F)\right] e^{\left(-\varepsilon/C([\frac{M}{M+B}],F)\right)}\right]\right] [1+\dot{\varepsilon}]^{D} \tag{4}$$

Table 4 - The Voce constitutive model parameters used for the constitutive fits shown in Figure 16.

Cooling Rate (°C/s)	T_{DEF} (°C)	Avg. Vickers Hardness (HV)	A, Saturation Stress (MPa)	B, Yield Stress (MPa)	C, Relaxation Strain (mm/mm)	D, Strain Rate Coefficient	R-squared Value
10	ND	339	1118.7	756.0	0.0134	0.0175	0.99
	800	282	989.8	617.9	0.0279	0.0215	0.98
	600	257	963.2	587.2	0.0486	0.0218	0.99
15	ND	413	1391.5	1049.6	0.0103	0.0161	0.98
	800	326	1168.9	799.7	0.0175	0.0215	0.99
	600	288	1061.1	654.8	0.0336	0.0187	0.99
30	ND	458	1538.7	1169.1	0.0097	0.0105	0.97
	800	450	1463.1	1061.7	0.0098	0.0141	0.99
	600	348	1232.4	803.0	0.0176	0.0155	0.98

Table 5 - The three-dimensional surface function constants.

	β_1	β_2	β_3	β_4	β_5	β_6	R^2 Value
$A\left(\left[\frac{M}{M+B}\right], F\right)$	853.0	809.3	3050.0	-152.9	2.016	$-2.051\text{x}10^4$	0.96
$B\left(\left[\frac{M}{M+B}\right], F\right)$	602.7	631.8	1438.0	-98.36	980.5	$-1.599\text{x}10^4$	0.96
$C\left(\left[\frac{M}{M+B}\right], F\right)$	0.01875	-0.03875	0.16570	0.03009	-0.23000	0.24470	0.95
D	0.018	-	-	-	-	-	-

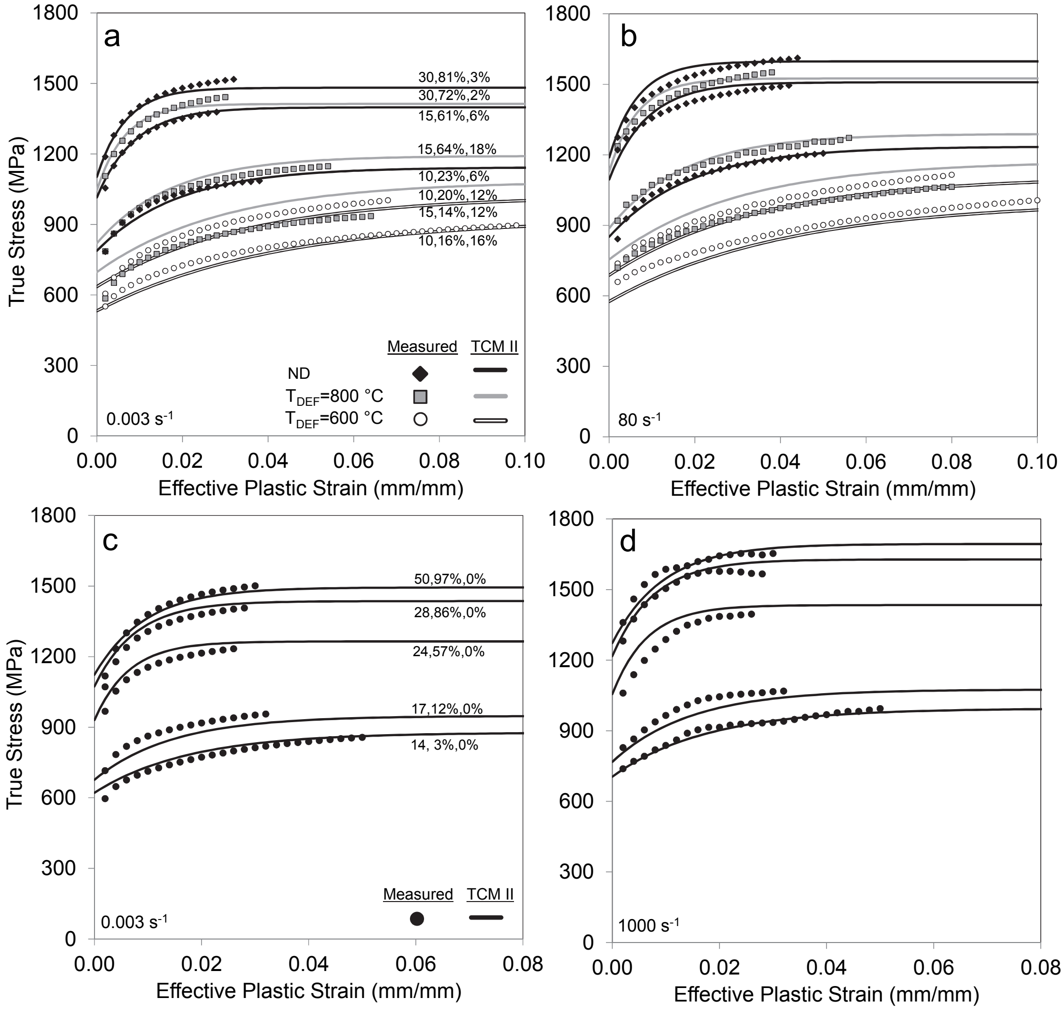

Figure 19 - The measured and predicted (TCM II) flow stress curves for the quenched and deformed specimens pulled at a strain rate of (a) 0.003 s^{-1} and (b) 80 s^{-1}. The T_{DEF}=600 °C and 30 °C/s results were omitted for clarity. The measured (from [12]) and predicted (TCM II) flow stress curves for the FAQA specimens pulled at a strain rate of (a) 0.003 s^{-1} and (b) 1075 s^{-1}. The numbers adjacent to the predicted curves indicate (cooling rate, $[M/(M+B)]$, F).

5 Discussion

It has been shown that for an equivalent Vickers hardness level, the presence of ferrite within a tailored microstructure results in an increase in the uniform elongation and n-value, a slight increase in ultimate tensile strength, but does not affect the yield strength. These combined mechanical properties resulted in increased energy absorption capacity (toughness) when compared to a material with tailored properties that is void of ferrite. From a crash perspective, one could argue that the introduction of ferrite into the soft regions of tailored hot stampings (due to inevitable or intentionally imposed deformation) can be beneficial rather than harmful. Further investigation concerning the fatigue life, impact properties and fracture toughness of material conditions tested in this work need to be conducted for a complete assessment of the overall material performance.

Although these enhanced properties have been shown to exist due to the presence of ferrite within the soft regions of the tailored microstructure, it should also be noted that the morphology of the bainite present within the tailored microstructure changes from an upper bainite type structure for a low ferrite area fraction material to a granular bainite morphology when the area fraction of ferrite is greater than approximately 6%. Limited research has been conducted into the difference in mechanical properties between a granular bainite and the upper bainite type structures observed in this work. The work of Caballero et al. [28] on the influence of bainite morphology on impact toughness revealed that the impact toughness of a lath-like upper bainite structure exhibits a higher impact toughness than a granular bainite structure due to the ease of crack propagation through the large packet size within granular bainite. Given this analysis, the enhanced mechanical properties measured for the quenched and deformed tailored microstructures containing granular bainite and ferrite (>6%) may be due to the presence of ferrite rather than the different morphology of the bainite present.

Due to inevitable plastic deformation during hot stamping of components with tailored properties, the presence of ferrite in the as-quenched microstructure is likely and must be accounted for. The primary motivation for the development of the TCM II is for improve predictive capability to more accurately predict the high strain rate (crash) constitutive behavior of tailored hot stampings in finite element crash simulations. Commercial finite element codes, such as LS-DYNA [44], contain material models developed specifically for hot stamping. These material models predict the decomposition of austenite into martensite, bainite, pearlite and ferrite due to the thermo-mechanical route that each element undergoes during a hot stamping simulation. The element history variable data after a hot stamping simulation can then be used in conjunction with the current TCM II to define the high strain rate properties as outlined for the numerical procedure described by Bardelcik et al. [11].

6 Conclusions

Based on the results presented in this article, the following conclusions can be made:

- The effect of simultaneous deformation during quenching of boron steels resulted in a significant reduction in the as-quenched hardness when the cooling rate was sub-critical, 15 °C/s and 10 °C/s. At a quench rate of 30 °C/s the as-quenched hardness was similar for the specimens that were not deformed and the specimens deformed at T_{DEF} = 800 °C. A reduction in the deformation temperature to T_{DEF} = 600 °C resulted in a significant decrease in hardness even for specimens quenched at 30 °C/s. Optical and SEM observations revealed that the softening effect was due to the presence of ferrite (in addition to martensite and bainite) within the as-quenched microstructure.

- Quasi-static uniaxial tension tests conducted on the quenched and deformed specimens revealed that for an equivalent hardness level, the presence of ferrite within the microstructure did not affect the initial yield strength (σ_Y), mildly increased the ultimate tensile strength (σ_{UTS}) and significantly increased the uniform elongation strain which in effect increased in the *n*-value. The observed effects of ferrite on the stress-strain response also improved the toughness (or energy absorption) of the materials as shown by the 28% increase in toughness for a bainitic material condition containing 16% ferrite (with 257 HV) when compared to a fully bainitic condition with a hardness of 268 HV. By analysing the toughness distribution with respect to material hardness, it was shown that as-quenched materials with hardness values ranging from approximately 300 HV to 425 HV resulted in reduced energy absorbing capacity, which must be considered during the design/development of a hot stamped component with tailored properties.

- In addition to the quasi-static (0.003 s^{-1}) uniaxial tension tests, intermediate strain rate tension tests were also conducted at approximately 10 s^{-1} and 80 s^{-1}. The effect of elevated strain rate on the σ_{UTS} and σ_Y was shown to be moderate as indicated by a change in σ_{UTS} of ~80 MPa for all of the conditions tested in this work when the loading rate was increased from 0.003 s^{-1} to 80 s^{-1}. It was also shown that the increase in σ_{UTS} (due to a change in $\dot{\varepsilon}$ from 0.003 s^{-1} to 80 s^{-1}) was slightly greater for the lower hardness (lower strength) material conditions.

- A Voce hardening model, coupled with an exponential-type strain rate sensitivity term was successfully fit to the experimental uniaxial tension data for the quench and deformed materials developed in this work and material conditions that did not contain any area fraction of ferrite from [12]. The model parameters were then fit with respect to effective plastic strain (ε), true strain rate ($\dot{\varepsilon}$), martensite – bainite area fraction relationship [$M/(M+B)$] and area fraction of ferrite (F). This resulted in the new Tailored Crash Model II (TCM II) constitutive model that was able to accurately capture the change in hardening behaviour and strain rate sensitivity of the multi-phase materials examined in this work.

Acknowledgements

Support for this research from Honda R&D North America, Promatek Research Center (Cosma International), ArcelorMittal Dofasco, the Natural Sciences and Engineering Research Council of Canada, the Ontario Research Fund and the Canada Research Chair Secretariat is gratefully acknowledged.

References

[1] H. Karbasian, A.E. Tekkaya, J. Mater. Process. Technol. 210 (2010) 2103-2118.

[2] ArcelorMittal - Usibor 1500P CCT Diagram (Personal communication).

[3] T. Altan, Hot-stamping boron-alloyed steels for automotive parts, Part I: Process methods and used, Stamping Journal Magazine. (2006) 40-41.

[4] P. Hein, Adv. Mater. Res. 6-8 (2005) 763-770.

[5] M. Jonsson, 1st International Conference on Hot Sheet Metal Forming of High-Performance Steel, Kassel, Germany, 2008, 253-265.

[6] P. Akerstrom, Modelling and simulation of hot stamping, PhD Thesis, University of Lulea, Sweden, 2006.

[7] M. Babbit, Steel Res. Int. 77 (2006) 620-626.

[8] M. Maikranz-Valentin, U. Weidig, U. Schoof, H.H. Becker, K. Steinhoff, Steel Res. Int. 79 (2008) 92-97.

[9] D.D. Munera, A. Pic, D. Abou-Khalil, F. Shmit, F. Pinard, SAE Int. J. Mater. Manuf. 1 (2009) 472-479.

[10] D.D. Munera, F. Pinard, L. Lacassin, SAE Trans. J. Mater. Manuf. 115 (2007) 796-804.

[11] A. Bardelcik, K. Ghavam, R. George, M.J. Worswick, 3rd International Conference on Hot Sheet Metal Forming of High-Performance Steel, 2011, 221-228.

[12] A. Bardelcik, M.J. Worswick, S. Winkler, M.A. Wells, Int. J. Impact Eng. 50 (2012) 49-62.

[13] J. Wilsius, B. Tavernier, D. Abou-Khalil, 3rd International Conference on Hot Sheet Metal Forming of High-Performance Steel, Kassel, Germany, 2011, 427-435.

[14] R. George, A. Bardelcik, M.J. Worswick, J. Mater. Process. Technol. 212 (2012) 2386-2399.

[15] A. Barcellona, D. Palmeri, Metall. Trans. A. 40 (2009) 1160-1174.

[16] J. Min, J. Lin, Y. Min, F. Li, Mater. Sci. Eng. A. 550 (2012) 375-387.

[17] R.Y. Zhang, J.D. Boyd, Metall. Trans. A. 41 (2010) 1448-1459.

[18] M. Naderi, A. Saeed-Akbari, W. Bleck, Mater. Sci. Eng. A. 487 (2008) 445-455.

[19] M. Abbasi, A. Saeed-Akbari, M. Naderi, Mater. Sci. Eng. A. 538 (2012) 356-363.

[20] M. Nikravesh, M. Naderi, G.H. Akbari, Mater. Sci. Eng. A. 540 (2012) 24-29.

[21] Z. Shi, K. Liu, M. Wang, J. Shi, H. Dong, J. Pu, B. Chi, Y. Zhang, L. Jian, Mater. Sci. Eng. A. 535 (2012) 290-296.

[22] D.W. Fan, H.S. Kim, B.C. De Cooman, Steel Res. Int. 80 (2009) 241-348.

[23] A.K. De, J.G. Speer, D.K. Matlock, Adv. Mater. Process. 161 (2003) 27-30.

[24] R. Smerd, S. Winkler, C. Salisbury, M. Worswick, D. Lloyd, M. Finn, Int. J. Impact Eng. 32 (2005) 541-560.

[25] A. Bardelcik, C.P. Salisbury, S. Winkler, M.A. Wells, M.J. Worswick, Int. J. Impact Eng. 37 (2010) 694-702.

[26] G. Krauss, Principles of Heat Treatment of Steel, 1st ed., American Society for Metals, Metals Park, Ohio, 1980.

[27] H.K.D.H. Bhadeshia, Bainite in Steels, Institute of Materials, United Kingdom, 2001.

[28] F.G. Caballero, H. Roelofs, S. Hasler, C. Capdevila, J. Chao, J. Cornide, C. Garcia-Mateo, Mats. Sci. Tech. 28 (2012) 95-102.

[29] N. Isasti, D. Jorge-Badiola, M. Taheri, B. López, P. Uranga, Effect of Composition and Deformation on Coarse-Grained Austenite Transformation in Nb-Mo Microalloyed Steels, Metall. Trans. A. 42 (2011) 3729-3742.

[30] B. Bramfitt, J. Speer, A perspective on the morphology of bainite, Metall. Trans. A. 21 (1990) 817-829.

[31] J.P. Wang, Z.-. Yang, B.Z. Bai, H.S. Fang, Mater. Sci. Eng. A. 369 (2004) 112-118.

[32] Y. Ohmori, H. Ohtani, T. Kunitake, Trans. Iron Steel Inst. Jpn. 11 (1971) 250-259.

[33] J.H. Hollomon, Transactions of the American Institute of Mining and Metallurgical Engineers. 162 (1945) 268-290.

[34] Standard test method for tensile strain-hardening exponents (n-values) of metallic sheet materials, ASTM. (2000) 607-613.

[35] H.J. Kleemola, M.A. Nieminen, Metall. Mater. Trans. 5 (1974) 1863-1866.

[36] M. Umemoto, Z.G. Liu, S. Sugimoto, K. Tsuchiya, Metall. Trans. A. 31 (2000) 1785-1794.

[37] K.G. Samuel, J. Phys. D-Appl. Phys. 39 (2006) 203-212.

[38] G.I. Taylor, J. Inst. Met. 62 (1938) 307-324.

[39] Y. Bergström, Mater. Sci. Eng. 5 (1970) 193-200.

[40] E. Voce, J. Inst. Met. 74 (1948) 537-562.

[41] G.R. Johnson, W.H. Cook, 7th International Symposium on Ballistics, 1983, 541-547.

[42] G.R. Johnson, W.H. Cook, Eng. Fract. Mech. 21 (1985) 31-48.

[43] F.J. Zerilli, R.W. Armstrong, J. Appl. Phys. 61 (1987) 1816-1825.

[44] J.O. Hallquist, LS-DYNA Keyword Users Manual, Version 971, (2012).

APPENDIX D: PART 4

Bardelcik A, George R, Worswick MJ. Transition Zone Tensile Properties within a Tailored Hot Stamping. *SAE World Congress 2012*, Paper# 2012-01-0531, 2012.

Transition Zone Tensile Properties within a Tailored Hot Stamping

2012-01-0531
Published
04/16/2012

Alexander Bardelcik, Ryan George and Michael J. Worswick
Univ. of Waterloo

ABSTRACT

Recent work at the University of Waterloo addressed the hot stamping of a lab-scale B-pillar using a heated and cooled die to produce a tailored part with a soft and hard region for which the microstructure was predominantly bainitic and martensitic, respectively. This paper addresses the tensile properties of the transition zone (hard to soft region) within this tailored hot stamping using experimental and numerical methods. Vickers hardness measurement showed that the fully softened and hardened material conditions were achieved across a 25 mm transition zone. Sub-size ASTM uniaxial tensile specimens were cut from the transition zone and pulled to failure. Due to the large variation in material properties within the gauge length of the specimens, apparent uniform elongations measured across the gauge length ranged from 0.02 to 0.04 engineering strain, while the calculated engineering ultimate tensile strength (UTS) varied from 798 to 913 MPa. The transition zone tension tests were simulated using the finite element (FE) code LS-DYNA and the tensile dog-bone specimen mesh used in the models was subdivided into "bins" of average hardness values as measured from transition zone hardness distributions. The constitutive response assigned to the elements of each "bin" was calculated using a strain rate sensitive constitutive model that was developed for tailored properties within hot stampings. Agreement between the predicted and measured stress-strain curves was excellent and the predicted strain distributions within the transition zone specimens agreed very well with measured strain distributions that were obtained using digital image correlation measurements.

INTRODUCTION

With the current demand to reduce vehicle weight while maintaining crashworthiness, the application of ultra high strength steel (UHSS) within vehicle structural components is desirable. The difficulty in applying UHSS is the inherently low ductility of the material. To overcome this limitation, the hot stamping process was developed in which austenized boron steel blanks are simultaneously formed and quenched within a die to produce parts with a fully martensitic microstructure that has ultimate tensile strengths of approximately 1500 MPa [1, 2, 3]. Although the fully hardened material state offers excellent intrusion resistance, the introduction of a lower strength and more ductile region within a hot stamped part may improve the crash performance of the component [4, 5, 6]. A hot stamped part containing a lower strength and more ductile region is said to have tailored properties [3].

A hot stamped component with tailored mechanical properties has been successfully produced using a custom, split-tool with both heating and cooling capabilities as shown by the CAD image in Figure 1a [7, 8]. This variation of the direct hot stamping process is referred to as the in-die partial heating technique which allows lower strength and more ductile regions to be formed within the hot stamped part, as presented in the hot stamping review article by Karbasian and Tekkaya [3]. The geometry of the hot stamped part is representative of a B-pillar structure (Figure 1b) and the advantage of imparting a soft region within a fully hardened part is the potential to improve the crash performance while maintaining the excellent intrusion resistance due to a fully hardened material state [4, 5, 9, 10]. The temperature of the heated section of the tool can be controlled from room temperature up to 400°C via cartridge heaters that have been embedded into the tool. The cooled section is maintained at or below room temperature using chilled water recirculation. A 3 mm air gap is introduced between the hot and cooled sections and serves to reduce the heat transfer. A complete description of the tooling design and hot stamping

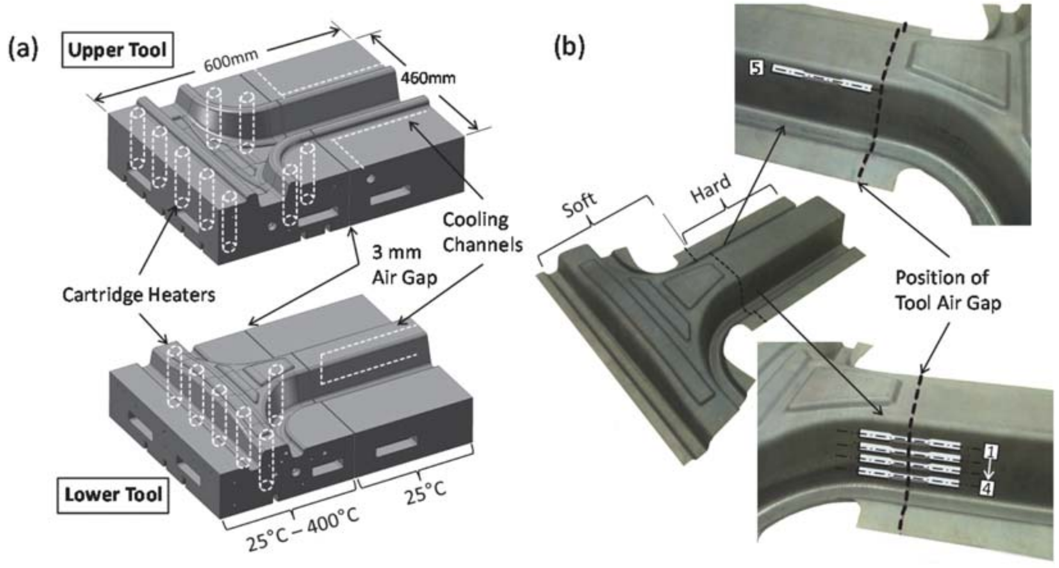

Figure 1. (a) A CAD image of the heated/cooled hot stamping die set (b) A photograph of a hot stamped part with the transition zone specimen locations highlighted. The dashed line indicates the location of the 3 mm air gap in the tool which represents the middle of the transition zone.

experiments/numerical models is presented by George et al. [7, 8]. In the aforementioned experiments, it was shown that a heated die temperature of 400°C resulted in a part with a soft (244-260 HV) and a hard (~488 HV) region for which the microstructures were predominantly bainitic and martensitic, respectively. The transition zone from the fully hard to soft material state was approximately 25 mm in width. The tensile behavior of the transition zone is deemed an area of interest and is the focus of the current work, in which the hardness distributions and tensile properties of specimens cut from the transition zone were characterized and then subsequently modeled using finite element (FE) analysis. The as-quenched material properties used in the FE models were based on a strain rate sensitive constitutive model developed for tailored properties by Bardelcik et al. [11].

HOT STAMPED TRANSITION ZONE SPECIMENS

Four transition zone tensile specimens were cut from the side wall of the hot stamped part as indicated by the overlaid specimen schematic in Figure 1b. The dog-bone tensile specimen geometry corresponds to the ASTM E8 sub-size specimen standard in which the gauge length is 25.4 mm and the overall length of the specimen is 100 mm. Four different specimen locations were selected because the deformation imposed along the side wall during hot stamping varied (nominal as-formed thickness varied) from specimen 1 to 4. This variation in deformation may have affected the phase transformation kinetics as a result of the material continuous cooling transformation (CCT) diagram shifting to lower transformation times, as shown in the work by Barcellona and Palmeri [12]. Also, the blank/die clearance during deformation in this area may have affected the as-quenched material state due to variations in heat transfer between the blank and die. For a comparison to a fully hardened material state, a specimen at location 5 for which the material is fully martensitic was also extracted and tested.

EXPERIMENTS

This section describes the tension tests, hardness measurements and digital image correlation (DIC) strain field measurements conducted in this work. The hot stamping process used to produce the B-pillar parts used in this work showed excellent repeatability [7, 8], therefore the number of parts used in the experiments was: 2 for the tension tests, 1 for the hardness measurements and 1 for the DIC study.

TENSION TESTS

An Instron model 1331 servo-hydraulic testing machine was used to conduct the uniaxial tension tests on the transition zone specimens (1-4) and the fully hardened specimen (5). Specimen elongation was measured using an Epsilon extensometer and the specimens were mounted within the Instron grips as shown in Figure 2a. A cross-head velocity of 0.076 mm/s was used to deform the specimens at a nominal strain rate of 0.003 s^{-1}. Due to the variation in mechanical properties, necking always occurred within the soft zone and in the vicinity of the extensometer attachment point. For each specimen location, two repeat tests were conducted and the average thickness (at the middle of the gauge length) for the various specimen locations is shown in Table 1. The thickness at either end of the gauge length for each specimen location was measured and the maximum variation in thickness along the gauge length was shown to be less than 2%.

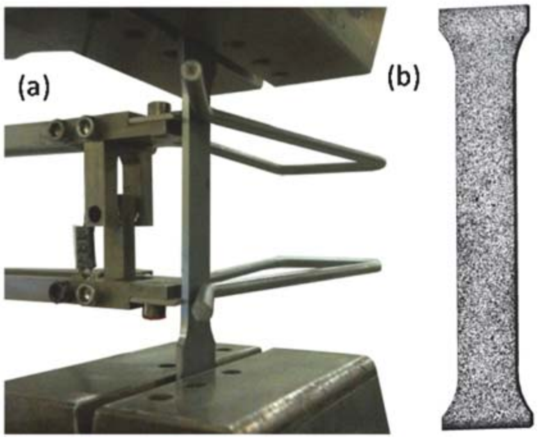

Figure 2. (a) A photograph of the extensometer and a specimen prior to a tension test (b) A photograph of a tensile specimen with the speckle pattern used in the DIC study.

Table 1. The average thickness (of two specimens) measured at the middle of the gauge length.

Specimen Location	Average Thickness (mm)
1	1.203
2	1.183
3	1.182
4	1.183
5	1.178

HARDNESS MEASUREMENTS OF TRANSITION ZONE SPECIMENS

A LECO MHT Series 2000 micro-hardness tester (with 1000 g load) was used to measure the Vickers hardness distribution along the center-line (and mid-thickness) of the five specimens shown in Figure 1b. The specimens were cold mounted in epoxy resin and polished to a mirror finish.

DIGITAL IMAGE CORRELATION STUDY

A single tensile specimen from each of the five locations was pulled in tension and the strain history was recorded using digital image correlation (DIC) techniques. The purpose of this study was to observe the strain distribution along the specimens and provide a comparison to finite element models of the tests. The DIC study tension test parameters were the same as those described above, with the exception that no extensometer was used and a random speckle pattern was applied to the tensile specimens, as shown in Figure 2b. During the test, a stereo camera system was used to track and record the speckle pattern at five frames per second. Post-processing of the images was conducted using the Correlated Solutions Incorporated software Vic-3D.

EXPERIMENTAL RESULTS

The length of the hardness distribution along each specimen was 85 mm and centered at the tool air gap which defines the middle of the transition, as shown in Figure 3. As expected, a strong hardening trend is observed along the length of the sample from the softened region (−40 mm) to the fully hardened region (40 mm). Hardness levels as low as 265 HV were observed in several of the samples which is indicative of a bainitic microstructure [11]. Hardness measurements in excess of 450 HV indicate a fully hardened, martensitic microstructure. The entire transition from the softened to hardened state is within the gauge length of the tensile samples. Figure 3 also shows a shift in the hardness distribution within some of the specimens with respect to the middle of the specimen which corresponds to the location of the air gap during the forming operation (Figure 1b). Note that the hardness of the location 5 specimen (fully hardened) exceeds 480 HV throughout the gauge length, as expected.

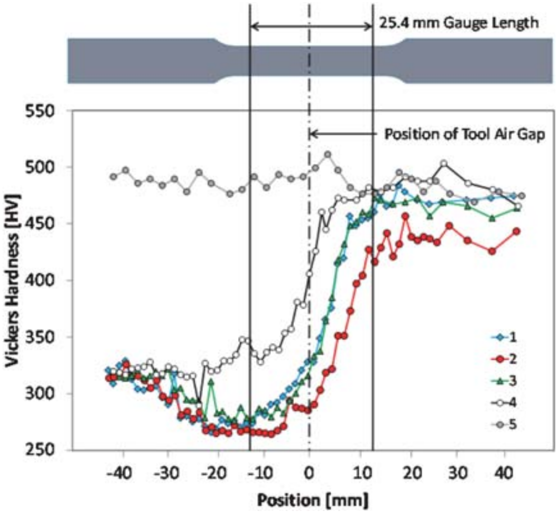

Figure 3. The Vickers hardness distribution of the tensile specimens from location 1 to 5.

For the transition zone specimens at locations 1 to 4, the tension test specimens are non-uniform due to the variation in mechanical properties throughout the gauge length. The engineering stress vs. engineering strain curves calculated from these tests are not valid in the conventional sense, but were calculated for comparison purposes and a relative ranking of stress-strain response with respect to location along the side wall of the B-pillar. The specimen at location 5 is considered a conventional tensile specimen due to the relatively uniform properties throughout the gauge length. Based on the two repeat tension tests that were conducted on the specimens from the five locations, an average engineering stress vs. engineering strain curve was created for each location and shown as solid black curves in Figure 4. The curve for location 3 was omitted for clarity since it overlaid the location 1 curve. The repeatability of the two tests was excellent with the greatest difference in stress level being less than 2% for the number four location repeat tests.

Due to the soft and lower strength region found at one end of each transition zone specimen, necking consistently occurred at one end of the gauge length where the extensometer was connected. This lead to some difficulty as the neck typically occurred at or outside of the gauge length; therefore the stress-strain curves shown in Figure 4 should only be considered accurate up to the apparent uniform elongation strain which ranged from an average value of 0.016 to 0.036 for the location 4 and 2 specimens, respectively.

The transition zone specimens showed limited elongations. This was expected because only a small portion (the soft region) of the entire specimen gauge length plastically deformed, resulting in an engineering strain that was calculated with the conventional assumption that the entire gauge length plastically deforms. This was confirmed by the engineering major strain (e1) contour plots extracted from the digital image correlation (DIC) (shown in Figure 5). The DIC images in Figure 5 were extracted at the apparent uniform elongation strain indicated in the figure which corresponds to the apparent ultimate tensile strength (UTS) of the curves shown in Figure 4. Due to a deterioration of the speckle pattern paint, some data loss was experienced in the high strain region of the location 1 DIC contour plot. The increase in average UTS observed at locations 2 (798 MPa), 1 (816 MPa), 3 (824 MPa) and 4 (913 MPa) is a result of increased volume fractions of the higher hardness (and higher strength) martensite phase present in the gauge length of the specimen, as shown by the hardness distributions in Figure 3. The shift in hardness distribution with respect to the tool air gap could be due to plastic deformation (which changes transformation kinetics [12]) or due to variations in quench rate that may have been caused by blank/die clearance differences along the side wall of the tool. Also, the steady-state die temperature distribution has not been measured and may have contributed to the hardness distribution variations.

The uniform elongation of the location 5 specimen occurred at 0.051 strain, but the strain distribution extracted at this point from the DIC image already indicates some degree of localization initiating at the center of the gauge length, where fracture eventually occurred. Further analysis of the DIC images indicated that a last true uniform elongation state occurred at a strain of roughly 0.043. This result is not surprising since the strain hardening behavior of martensite is very low near the UTS and the presence of a diffuse neck is expected.

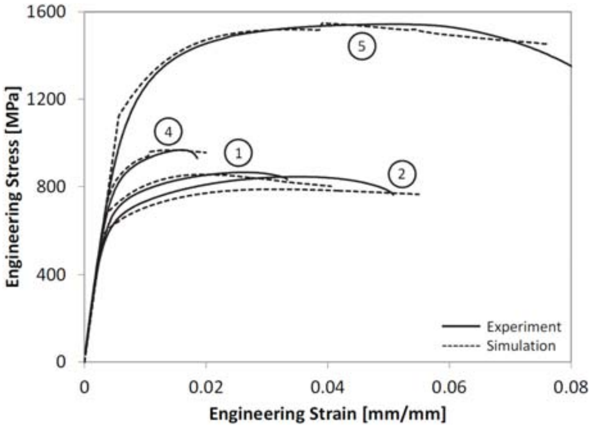

Figure 4. The measured and predicted engineering stress vs. engineering strain curves for the location 1,2,4 and 5 specimens. The location 3 results were omitted for clarity.

MODELS

The transition zone tension tests were modeled using the explicit dynamic finite element (FE) code LS-DYNA [13]. Mass scaling was implemented to reduce computational time. The tensile specimens were meshed with ~0.5 × 0.5 × 0.3 mm solid brick elements as shown in Figure 6a. There are two elements through the thickness of the ¼ symmetry model. The entire length of the grip regions were not meshed for simplicity and symmetry boundary conditions were applied to the ¼ model at the symmetry planes shown in Figure 6a. One end of the specimen was fully constrained and the other end was displaced in the x direction at the same constant crosshead velocity prescribed in the tension test experiments.

Due to the variation in measured Vickers hardness along the centerline gauge length of the tensile specimens (see Figure 3), the FE mesh was subdivided into five "bins" based on a nominal measured hardness value along the length of each bin, as shown in Figure 6a. These nominal hardness values were then used to define the true stress vs. effective plastic strain (or flow stress) curves for each bin according to the

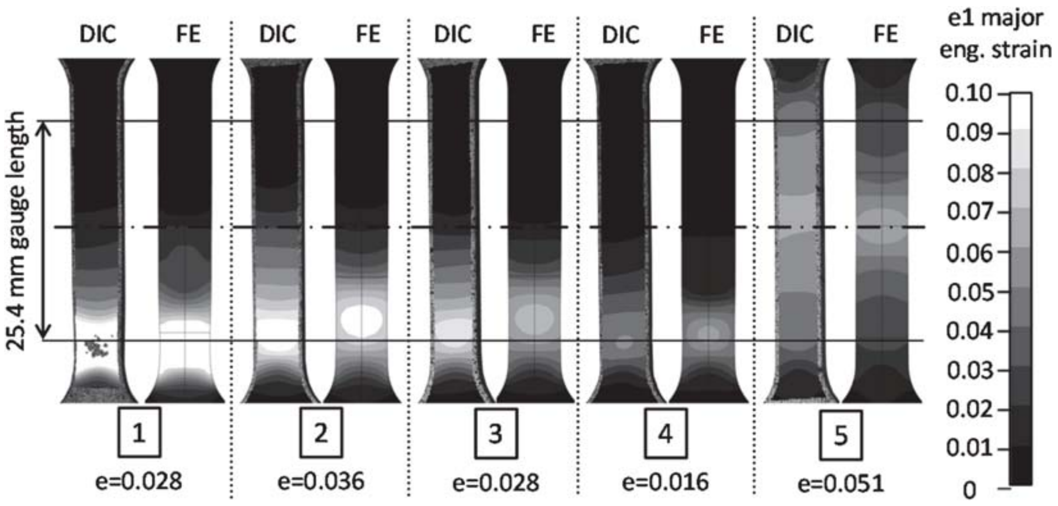

Figure 5. The measured (DIC) and predicted (FE) major engineering strain distributions at the strain state indicated. The framed numbers indicate the specimen location.

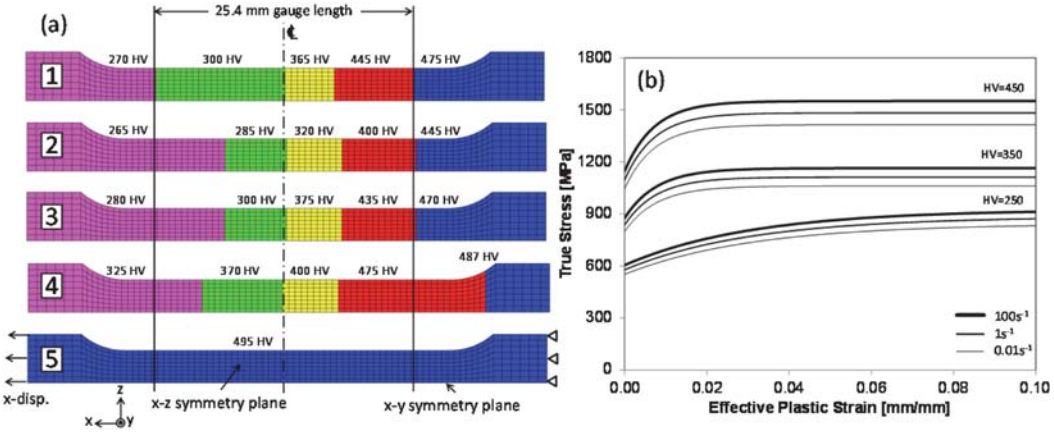

Figure 6. (a) Finite element mesh of the tensile specimens cut from location 1 to 5. (b) A plot of flow stress curves generated using the strain rate sensitive constitutive model [11].

strain rate sensitive tailored property constitutive model developed by Bardelcik et al. [10, 11]. This constitutive model was derived from tensile data collected on specimens where the microstructure was either fully bainitic, fully martensitic or had mixed volume fractions of bainite/ martensite. The tensile experiments used to generate the data for the constitutive model were conducted under quasi-static (0.003 s^{-1}, 1.0 s^{-1}), intermediate (~85 s^{-1}) and high strain rate (~1075 s^{-1}) loading conditions. The constitutive model is a single equation (based on the Voce hardening law) that is a function of strain, strain rate and as-formed Vickers hardness. The model was used to calculate the point-wise stress-strain-strain rate data that was converted into tabular form and implemented using Material 24 (*MAT_PIECEWISE_LINEAR_PLASTICITY) within LS-DYNA. Figure 6b is a plot of the flow stress curves that were calculated using this constitutive model [10, 11]. Note that these curves are extrapolated beyond the point of uniform elongation. For the FE models developed in the current work, the mechanical properties were assumed to be uniform along the length, width and thickness of each bin region. A uniform thickness was applied to the meshes corresponding to the average measured thickness shown in Table 1.

The black dashed curves in Figure 4 are the engineering stress vs. engineering strain curves that were extracted from the finite element (FE) simulations of the tension tests. Overall, the models predict the stress-strain response very well with the exception of a slight under estimation of the stress level for location 2. Contour plots of the engineering major strain (e1) from the FE models are shown in Figure 5 at the same strain state as the contour plots from the DIC study (also shown in the figure). The measured and predicted strain distributions agree very well for the transition zone specimens at location 1 to 4. The FE model of location 5 predicted the strain distribution of this fully martensitic specimen very well and exhibited the initial localization at UTS that was observed as a diffuse neck in the DIC contours. The predicted engineering stress suddenly increases during the tension test simulations for the location 4 and 5 specimens. At the point of sudden stress increase, it was observed that a group of elements became unstable which is analogous to the onset of necking and was manifest in the models as a rapid element elongation from one time step to the next. The increased deformation rate of these "necked" elements resulted in the stress increase due to the strain rate sensitive constitutive model used in the simulations. Because the transition zone specimens have a complex and varying material state along the gauge length, the good predictions validate the use of the current constitutive model [11] for application to FE simulations of as-quenched hot stamped parts with tailored properties.

The lab-scale B-pillar hot stamping experiments (which were used to produce the B-pillar parts used in this study) were also modeled by George et al. [7, 8] using the hot stamping constitutive model due to Akerstrom [2] as implemented within LS-DYNA [14]. In the work by George et al., the predicted as-quenched Vickers hardness distribution of the B-pillar agreed well with the experiments at sample locations throughout the part, but the predicted transition zone hardness distribution (circled region in Figure 7a and b) along the height of the side wall was not validated against the experiments. Based on the hardness measurements in Figure 3, the location of the transition zone is taken as the position where the hardness is mid-way between (median hardness) the maximum and minimum measured hardness values for each transition zone specimen. The location is plotted as the black points on the part image in Figure 7c. The transition zone boundary is then shown as a line drawn between these black points. The shape of this boundary corresponds well to the hardness contour shown in Figure 7b. This variation in transition zone distribution needs to be accounted for when considering the subsequent crash/impact properties of such structures during the development phase of hot stamped automotive components.

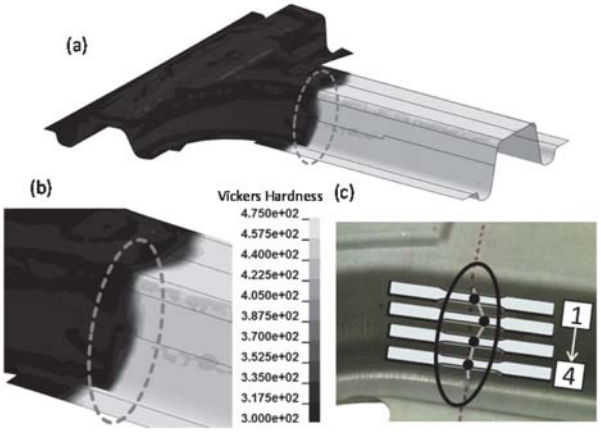

Figure 7. (a) The predicted Vickers hardness distribution throughout the as-quenched B-pillar from [7, 8] (b) An enlarged image of the transition zone Vickers hardness contour plot (c) The measured median hardness distribution overlaid on a picture of the B-pillar transition zone.

SUMMARY/CONCLUSIONS

Based on the results obtained from this work, the following conclusions can be made:

- The hardness distribution profile within the transition zone varied with respect to the tool air gap for the four specimen locations studied along the B-pillar side wall. The position of the measured median hardness along the side wall of the B-pillar was predicted well by the hot stamping finite element model created by George et al. [7, 8].

- Tension tests conducted on the transition zone specimens revealed that the highest strength region was at location 4 and the lowest strength region was location 2. All of the transition zone stress-strain curves showed limited ductility due to the presence of the fully hardened regions within the gauge length which only deformed elastically.

- Finite element models of the transition zone specimens accurately predicted the engineering stress vs. strain curves calculated from the tension tests. A DIC study revealed that the predicted and measured strain distributions within specimens at locations 1 to 5 agreed very well. These two findings validate the use of the strain rate sensitive constitutive model developed by Bardelcik et al. [10, 11].

CONTACT INFORMATION

Alexander Bardelcik, MASc
PhD Candidate
University of Waterloo
Department of Mechanical and Mechatronics Engineering
abardelc@uwaterloo.ca

ACKNOWLEDGMENTS

Support for this research from Honda R&D Americas, Promatek Research Center (Cosma International), ArcelorMittal, the Natural Sciences and Engineering Research Council, and the Ontario Research Fund is gratefully acknowledged.

REFERENCES

1. Altan, T., “Hot-stamping boron-alloyed steels for automotive parts, Part I: Process methods and used,” Stamping Journal Magazine, 40-41, 2006.

2. Akerstrom, P., “Modelling and simulation of hot stamping,” PhD thesis, University of Lulea, 2006.

3. Karbasian, H., and Tekkaya, A.E., “A review on hot stamping,” J. Mater. Process. Technol. **210**(15):2103-2118, 2010.

4. Maikranz-Valentin, M., Weidig, U., Schoof, U., Becker, H.H., et al., “Components with optimised properties due to advanced thermo-mechanical process strategies in hot sheet metal forming,” Steel Res. Int. **79**(2):92-97, 2008.

5. Duque Múnera, D., Pic, A., Abou-Khalil, D., Shmit, F. et al., “Innovative Press Hardened Steel Based Laser Welded Blanks Solutions for Weight Savings and Crash Safety Improvements,” *SAE Int. J. Mater. Manuf.* 1(1):472-479, 2009, doi:10.4271/2008-01-1076.

6. Wilsius, J., Tavernier, B., and Abou-Khalil, D., “Experimental and Numerical Investigation of Various Hot Stamped B-Pillar Concepts Based on Usibor 1500P,” presented at 3rd International Conference on Hot Sheet Metal Forming of High-Performance Steel, 2011.

7. George, R., Bardelcik, A., and Worswick, M.J., “Hot forming of boron steels using heated and cooled tooling for tailored properties,” J. Mater. Process. Technol. (Under Review).

8. George, R., “Hot Forming of Boron Steels with Tailored Mechanical Properties: Experiments and Numerical Simulations,” MASc thesis, University of Waterloo, 2011.

9. Múnera, D., Pinard, F., and Lacassin, L., “Very and Ultra High Strength Steels Based Tailored Welded Blanks: A Step Further Towards Crashworthiness Improvement,” SAE Technical Paper 2006-01-1213, 2006, doi: 10.4271/2006-01-1213.

10. Bardelcik, A., Ghavam, K., George, R., and Worswick, M.J., “An impact model of a hot stamped lab-scale b-pillar with tailored properties,” presented at 3nd International Conference on Hot Sheet Metal Forming of High-Performance Steel, 2011.

11. Bardelcik, A., Worswick, M.J., Winkler, S.L., and Wells, M.A., “A Strain Rate Sensitive Constitutive Model for Quenched Boron Steel with Tailored Properties,” Int. J. Impact Eng. (Under Review).

12. Barcellona, A., and Palmeri, D., “Effect of Plastic Hot Deformation on the Hardness and Continuous Cooling Transformations of 22MnB5 Microalloyed Boron Steel,” Metall. Trans. A **40**(5):1160-1174, 2009.

13. Hallquist, J. O., “LS-DYNA Keyword Users Manual, Version 971,” 2007.

14. Olsson, T., “An LS-DYNA material model for simulations of hot stamping processes of ultra high strength steels,” presented at 2nd International Conference on Hot Sheet Metal Forming of High-Performance Steel, 2009.